



2015

An Experimental Method of Measuring Spectral, Directional Emissivity of Various Materials and Joule Heating

Robert Bickel

University of Kentucky, rsbickel@gmail.com

[Click here to let us know how access to this document benefits you.](#)

Recommended Citation

Bickel, Robert, "An Experimental Method of Measuring Spectral, Directional Emissivity of Various Materials and Joule Heating" (2015). *Theses and Dissertations--Mechanical Engineering*. 60.
https://uknowledge.uky.edu/me_etds/60

This Master's Thesis is brought to you for free and open access by the Mechanical Engineering at UKnowledge. It has been accepted for inclusion in Theses and Dissertations--Mechanical Engineering by an authorized administrator of UKnowledge. For more information, please contact UKnowledge@lsv.uky.edu.

STUDENT AGREEMENT:

I represent that my thesis or dissertation and abstract are my original work. Proper attribution has been given to all outside sources. I understand that I am solely responsible for obtaining any needed copyright permissions. I have obtained needed written permission statement(s) from the owner(s) of each third-party copyrighted matter to be included in my work, allowing electronic distribution (if such use is not permitted by the fair use doctrine) which will be submitted to UKnowledge as Additional File.

I hereby grant to The University of Kentucky and its agents the irrevocable, non-exclusive, and royalty-free license to archive and make accessible my work in whole or in part in all forms of media, now or hereafter known. I agree that the document mentioned above may be made available immediately for worldwide access unless an embargo applies.

I retain all other ownership rights to the copyright of my work. I also retain the right to use in future works (such as articles or books) all or part of my work. I understand that I am free to register the copyright to my work.

REVIEW, APPROVAL AND ACCEPTANCE

The document mentioned above has been reviewed and accepted by the student's advisor, on behalf of the advisory committee, and by the Director of Graduate Studies (DGS), on behalf of the program; we verify that this is the final, approved version of the student's thesis including all changes required by the advisory committee. The undersigned agree to abide by the statements above.

Robert Bickel, Student

Dr. Michael Winter, Major Professor

Dr. Haluk Karaca, Director of Graduate Studies

AN EXPERIMENTAL METHOD OF MEASURING
SPECTRAL, DIRECTIONAL EMISSIVITY OF
VARIOUS MATERIALS AND JOULE HEATING

THESIS

A thesis submitted in partial fulfillment of the
requirements for the degree of Master of Science in
Mechanical Engineering in the College of Engineering
at the University of Kentucky

By:

Robert S. Bickel

Lexington, Kentucky

Director: Dr. Michael Winter

Assistant Professor of Mechanical Engineering

Lexington, Kentucky

Copyright © Robert S Bickel 2015

ABSTRACT OF THESIS

AN EXPERIMENTAL METHOD OF MEASURING SPECTRAL, DIRECTIONAL EMISSIVITY OF VARIOUS MATERIALS AND JOULE HEATING

Emissivity is an important parameter in calculating radiative cooling of a surface. In experiments at the NASA Ames hypervelocity ballistic range, one of the main errors indicated in temperature measurements is the uncertainty of emissivity for the materials under investigation. This thesis offers a method for measuring emissivity of materials at elevated temperatures at the University of Kentucky. A test specimen which consists of different sample materials under investigation and a blackbody cavity was heated in a furnace to an isothermal condition at known temperature. The emitted thermal radiation was measured and the comparison of sample and blackbody radiation yielded the desired emissivity. In addition to the furnace measurements, separate experiments were conducted in ambient air to determine how much irradiation is reflected back to the samples from the radiation shield used in the furnace to block undesired ambient radiation. Here, the sample heating was accomplished by applying a direct current across the samples. ANSYS simulations were performed to assist the design and analysis. Experiments were conducted in ambient air and a vacuum environment to verify these simulations.

KEYWORDS: Radiation, emissivity, Joule heating, blackbody, spectroscopy

Robert S. Bickel

15 July 2015

AN EXPERIMENTAL METHOD OF MEASURING SPECTRAL, DIRECTIONAL
EMISSIVITY OF VARIOUS MATERIALS AND JOULE HEATING

By

Robert S. Bickel

Dr. Michael Winter

Director of Thesis

Dr. Haluk Karaca

Director of Graduate Studies

4 August 2015

This work is dedicated to my parents Stephen and Karen Bickel. I greatly appreciate all of the sacrifices you two have made so that I may reach my full potential. I love you both very much

ACKNOWLEDGEMENTS

The following thesis benefited from the insights and direction of several individuals. First, my thesis chair Dr. Michael Winter has helped me not only grow as a graduate student but as an engineer as well. He has spent countless hours mentoring me through designs and solutions, and has worked hard on my behalf to provide funding for me throughout my time at the University of Kentucky. He has worked patiently with me, and I am thankful for his devotion to my studies. On the same note, Dr. Dusan Sekulic has offered his facilities and insights for completing my studies. Without his laboratory, much of this work would not have been possible. During my time at UK, I have also taken two classes led by Dr. Sekulic which were both very beneficial for my career. Dr. Sekulic' research team, in particular Hai Fu, helped us greatly with operating their furnace for our experiments. Dr. Kozo Saito, Dr. Nelson Akafuah and Dr. Ahmad Salaimah were instrumental in my research as well by providing us with an infrared camera that was used in this work. I would also like to thank NASA KY and NASA Ames. Without funding that I received for my studies from NASA KY through NASA award No: NNX10AL96H much of this research would not have happened. NASA Ames, in particular Dr. Michael Wilder, provided motivation for this research, as well as sharing his insights on the project.

I would also like to thank the members of the Radiation Sciences lab: Helmut Koch, Zhaojin Diao, Bradley Butler, and Christian Arnold. Helmut has provided many suggestions and has mentored me throughout designing my experimental setup. I was very fortunate to have someone with research experience sitting in close proximity to me.

Zhaojin and Bradley both contributed aspects of my setup that I would use for my measurements. Without their contributions, this work would have suffered.

Thirdly, I would like to offer my gratitude to Floyd Taylor, Herb Mefford, and Julius Schoop. All three machined multiple assemblies necessary for my research.

Additionally, they worked with me during the design process to ensure that my setups could be manufactured. Dr. Haluk Karaca provided us with his group's electrical discharge machine for cutting our NASA samples which was necessary for our work.

Finally, I would like to thank my father and mother for encouraging me to pursue a Masters in Mechanical Engineering as well as my brothers, Scott Bickel and Jeff Langford, and my sisters Kelly Bickel and Katherine Bickel. Without their support and guidance throughout my educational career, I would not have reached my full potential.

Lastly, I would like to thank my dear girlfriend Akiko for being my side during this journey.

TABLE OF CONTENTS

ACKNOWLEDGEMENTS	iii
LIST OF TABLES.....	ix
LIST OF FIGURES	x
NOMENCLATURE	xii
1 INTRODUCTION	1
1.1 Objective.....	3
2 THEORY	5
2.1 Radiation Theory.....	5
2.1.1 Blackbody Theory.....	6
2.1.2 Emissivity Theory	7
2.1.3 Blackbody Design	8
2.1.4 Reflected Radiation	9
2.1.5 View Factors	10
2.2 Joule Heating.....	11
2.3 Thermal Energy Balances in Cylindrical Coordinates	12
3 LITERATURE REVIEW	15
4 AMBIENT AIR JOULE HEATING SIMULATION AND EXPERIMENT	19
4.1 Experimental Setup	19
4.1.1 Temperature Measurement and Recording:.....	20
4.1.2 Electrical Control	21
4.1.3 Experimental Procedure:	22

4.2	Experimental Results	22
4.3	Ambient Air Joule Heating Simulation	24
4.3.1	Geometry and Mesh Size	25
4.3.2	Boundary Conditions	25
4.3.3	Material Properties	26
4.3.4	Simulation Results	26
4.4	Conclusions	29
5	VACUUM JOULE HEATING SIMULATION AND EXPERIMENT	33
5.1	Experimental Setup	33
5.1.1	Electrical Control	35
5.1.2	Water Cooling	35
5.1.3	Temperature Measurement	36
5.1.4	Vacuum Operations	37
5.2	Experimental Procedure	37
5.3	Simulation Vacuum Chamber Joule Heating Experiment	38
5.3.1	Geometry and Mesh Size	38
5.3.2	Boundary Conditions	39
5.4	Experimental and Simulation Results	40
5.4.1	Test case 1: Atmospheric Pressure and No water Cooling	40
5.4.2	Test case 2: Atmospheric pressure and water cooling	42
5.4.3	Test case 3: vacuum environment with water cooling	45

6	EXPERIMENTAL DESIGN FOR MEASURING SPECTRAL, DIRECTIONAL EMISSIVITY	50
6.1	Facility Overview	50
6.1.1	Radiation Shield Cooling Adapter	51
6.1.2	Optical Setup.....	56
6.2	Sample Preparation.....	64
6.2.1	Sample Holder Design I	66
6.2.2	Sample Holder Design II	67
6.3	Isothermal Test.....	68
6.3.1	Experimental Procedure.....	69
6.3.2	Experimental Results and Analysis.....	69
6.4	Spectrally Resolved Measurements in the VIS/NIR Wavelength Range.....	76
6.4.1	Experimental Procedure.....	76
6.4.2	Experimental Results.....	78
7	RADIATION REFLECTED BY SHIELD EXPERIMENT	84
7.1	ANSYS Simulations.....	84
7.1.1	Geometry and Mesh Size.....	84
7.1.2	Boundary Conditions.....	85
7.1.3	Simulation Results.....	86
7.1.4	Final Design	89
7.2	View factor calculations	90

7.3	Reflectivity experimental setup.....	93
7.3.1	Experimental Setup	93
7.3.2	Experimental Procedure.....	93
7.4	Experimental Analysis.....	94
7.5	Experimental Results	95
7.5.1	Experiment one: no anti-reflective paint	95
7.6	Analysis and Conclusions	98
8	CONCLUSIONS	99
	APPENDIX 1 ASSEMBLY DRAWINGS.....	102
A 1.1	Six Way Assembly	103
A 1.2	Radiation Adapter Assembly	113
A 1.3	Sample Holder Assembly	119
A 1.4	FLIR IR Camera Adapter	128
	APPENDIX 2: CALCULATED ELECTRICAL RESISTIVITY	133
	APPENDIX 3: CALCULATED HEAT TRANSFER COEFFICIENT VALUES.....	135
	APPENDIX 4: MATLAB CODE FOR EMISSIVITY ANALYSIS.....	137
	APPENDIX 5: OPERATION MANUAL FOR SIX WAY	151
	REFERENCES	155
	VITA.....	159

LIST OF TABLES

Table 4-1 Test case matrix for ANSYS simulations	24
Table 4-2 Thermal conductivity of materials (Touloukian)	26
Table 4-3 Percent difference for simulation case 1 and case 2.....	32
Table 5-1 List of test case conditions for experiments	33
Table 5-2 Maximum temperature for measured and ANSYS for virgin graphite rod	42
Table 5-3 Test case 2: Maximum temperature for preheated graphite measured and ANSYS values comparison.....	45
Table 5-4 ANSYS simulation and experimental data comparison for test cast 3, preheated graphite sample	49
Table 6-1 Summary of sample surfaces received from NASA Ames.....	64
Table 7-1 View factor results with D=6.5”	92
Table 7-2 Average count difference across each sample.....	98
Table 7-3 Percent difference for counts measured in isothermal test based on reflectivity measurements.....	98

LIST OF FIGURES

Figure 1-1 Experimental cycle diagram	3
Figure 2-1 Spectral blackbody emissive power (Modest)	7
Figure 2-2 Apparent emittance from an isothermal cylindrical cavity.....	9
Figure 2-3 Pictorial representation of surface A_i and surface A_j	10
Figure 2-4 Controlled volume in cylindrical coordinates.....	13
Figure 2-5 Uniform heat generation in a cylinder.....	14
Figure 3-1 Szeles and Wolfe setup with a separate blackbody.....	16
Figure 3-2 Experimental setup with a moving sample (Atkinson and Strange).....	17
Figure 3-3 Schematic of experimental setup (Postlethwait et al, 1994).....	18
Figure 4-1 Photo of ambient Joule heating setup.....	20
Figure 4-2 Thermocouple locations (inches) on the graphite rod for ambient air Joule heating experiment	21
Figure 4-3 Experimental results displaying the maximum temperature at each thermocouple location	22
Figure 4-4 Current vs Temperature for all give locations	23
Figure 4-5 Measured temperature profiles at 60 amperes	24
Figure 4-6 Geometry with meshing for ambient air Joule heating simulation	25
Figure 4-7 Simulation case 1: temperature profile graph	27
Figure 4-8 Simulation case 1: current vs temperature graph	28
Figure 4-9 Simulation case 2: temperature profile graph	28
Figure 4-10 Simulation case 2: current vs temperature graph	29
Figure 4-11 Maximum measured temperatures of measured and simulated cases.....	30
Figure 4-12 Maximum temperature comparison between measured results, simulation case 1, and simulation case 2 at 100 Amps.....	31
Figure 5-1 Photo of vacuum chamber assembly	34
Figure 5-2 Top cross sectional view of six way.....	35
Figure 5-3 Cooling water schematic for cathode side	35
Figure 5-4 Thermocouple location for vacuum chamber graphite rod in inches.....	37
Figure 5-5 Geometry and mesh used in the vacuum Joule heating simulation.....	39
Figure 5-6 Maximum temperature measured for test case 1.....	40
Figure 5-7 Test case 1: maximum temperature and power comparison for samples.....	41
Figure 5-8 Test case 2: virgin graphite center temperature vs time graph	43
Figure 5-9 Test case 2: Preheated graphite rod temperature vs time graph.....	43
Figure 5-10 Test case 2: preheated graphite temperature profile for measured and simulation values at 100 amperes.....	45
Figure 5-11 Temperature profile plot of virgin rod and preheated rod	46
Figure 5-12 Maximum Measured Temperature Time Profile for test case 3: virgin graphite	47
Figure 5-13 Maximum measured temperature time profile for test case 3: preheated graphite sample	48
Figure 6-1 Picture of furnace used to heat samples to desired temperatures.....	50
Figure 6-2 Radiation cooling adapter attached to the furnace	51
Figure 6-3 Hidden line view of radiation shield adapter and furnace	52
Figure 6-4 Transmission curve for sapphire window [Edmund Optics]	53

Figure 6-5 Radiation shield measured temperature at furnace temperature 775 °C	54
Figure 6-6 Measured temperature of shield in furnace at 970°C for 60 seconds.....	55
Figure 6-7 ANSYS results for temperature profile of radiation shield	56
Figure 6-8 Sketch of optical setup for emissivity measurements.....	57
Figure 6-9 Picture of optical setup	57
Figure 6-10 Alignment diodes imaged on the entrance slit of the spectrometer	59
Figure 6-11 Uncalibrated wavelength reported by the CCD at one row	60
Figure 6-12 Calibrated wavelength data.....	61
Figure 6-13 Equation 6-1 dimensions	63
Figure 6-14 Picture of Samples received from NASA	65
Figure 6-15 Three samples cut from a wafer	66
Figure 6-16 Sample holder design I	66
Figure 6-17 Sample holder design II	67
Figure 6-18 Isothermal test: furnace image	70
Figure 6-19 Temperature variation across the samples	71
Figure 6-20 Graphite sample with blackbody outline	72
Figure 6-21 Isothermal test of 30° sample.....	73
Figure 6-22 Emitting surface on sample holder design 1	73
Figure 6-23 Isothermal test: emissivity results	75
Figure 6-24 Areas investigated for spectroscopy measurements	79
Figure 6-25 Measured blackbody curve vs Planck’s curve	80
Figure 6-26 Intensity calibration and blackbody spectra (count/sec).....	80
Figure 6-27 Normalized blackbody curve at 700 nm.....	81
Figure 6-28 Measured emissivity values in visible wavelength for stainless steel 304	82
Figure 7-1 Comparison of sample mesh sizes for ANSYS Simulation.....	85
Figure 7-2 Simulated temperature profile at 200 amperes for steel.....	86
Figure 7-3 Simulated temperature profile at 250 amperes for steel.....	87
Figure 7-4 Simulated temperature profile at 200 amperes of titanium sample.....	88
Figure 7-5 Simulated temperature profile at 250 amperes of titanium sample.....	88
Figure 7-6 Top view of reflected irradiation setup.....	89
Figure 7-7 Clamping Mechanism.....	90
Figure 7-8 Area definitions for view factor calculations.....	91
Figure 7-9 Variable definition for equation 7-2.....	91
Figure 7-10 View factor from shield to sample	93
Figure 7-11 Experiment 1: Surface plot without shield covering sample at.....	95
Figure 7-12 Experiment 1 reflected irradiation on sample at 0°	96
Figure 7-13 Experiment 1 reflected irradiation on sample at 30°	97
Figure 7-14 Experiment 1 reflected irradiation on sample at 60°	97

NOMENCLATURE

Greek Symbols

ϵ	emissivity
ϵ_a	apparent emissivity
λ	wavelength
μ	kinematic viscosity
ρ	mass density
σ	standard deviation
σ_{sb}	Stefan-Boltzmann constant

Latin Symbols

A	area
BG	background
c	speed of light
cp	specific heat
CS	cross sectional area
d	diameter
E	emissive power
g	gravitational acceleration
G	Irradiation
Gr	Grashof Number
i	current
I	Intensity
J	radiosity
k	thermal conductivity
k_r	mean roughness value
K	Kelvin
L	length
N	number of samples
Pr	Prandtl number
R	resistance
Ra	Rayleigh number
sr	Serrand
SE	uncertainty
q''	heat flux
T	temperature
t	time
V	volts
W	watt
WOS	without shield
WS	with shield

Subscripts

b	blackbody
cond	conduction

conv	convection
f	film
hc	horizontal cylinder
hp	horizontal plate
rad	radiation
ref	reflection
s	surface
sz	local surface
vp	vertical plate
∞	at infinity

1 INTRODUCTION

Thermal radiation is an important parameter for calculating heat flux, especially at high temperatures where radiation may be dominant over heat conduction and heat convection. Thus, knowledge of thermal radiation is key in many industrial applications including aerospace engineering, combustion, nuclear reactions, solar energy collection, and climatology (Modest). Thermal emissivity is an important property in calculating radiation heat flux. Emissivity is defined as the ratio of the energy emitted from a given surface to the energy emitted by a black surface at the same temperature and wavelength. In this definition a black surface absorbs all incident radiation, and does not reflect nor transmit at all. The emissivity of a material depends on a wide variety of factors including the material temperature, surface roughness, surface condition (e.g. oxidation), wavelength and direction (Furukawa and Iuchi). With many parameters affecting the emissivity value of materials, it becomes apparent why research of emissivity is vital.

The necessity to understand the spectral, directional emissivity of stainless steel 304 and titanium 6AL-4V at various roughnesses stems from research being conducted at the hypersonic ballistic range facility at NASA Ames Research Center. At this facility, researchers are interested in studying the convective heat transfer rates to these materials traveling between 3.4 km/s and 6 km/s at ambient temperatures and pressures ranging from 0.016 atm to 0.4 atm. These environments simulate atmospheric flight reentry conditions. To calculate the heat flux, the temperature distributions of these materials were measured with thermal imaging. Two types of high speed cameras were utilized for measuring the emitted radiation from the samples with one type operating from 0.53 μm

to 0.86 μm and the other type operating between 3-5 μm . In order to convert the intensity measured by the thermal cameras to temperatures, the emissivity of the materials must be known. The researchers state that the uncertainties in emissivity of the materials caused a 5% uncertainty for derived temperatures in the visible range, and a 7.5% uncertainty in temperatures in the infrared range (Wilder, Reda, and Prabhu).

Thus, a setup was developed at the University of Kentucky to measure the spectral, directional emissivity of the materials used at NASA Ames at elevated temperatures. To confirm the validity of assumptions used in the experiment, a second setup was engineered based on experimental models conducted with ANSYS Workbench 16.0. Furthermore, to ensure the validity of the ANSYS Joule heating models, experiments were performed to measure the temperature distribution of graphite rods heated in ambient air and a vacuum environment. This test cycle is explained in Fig. 1-1.

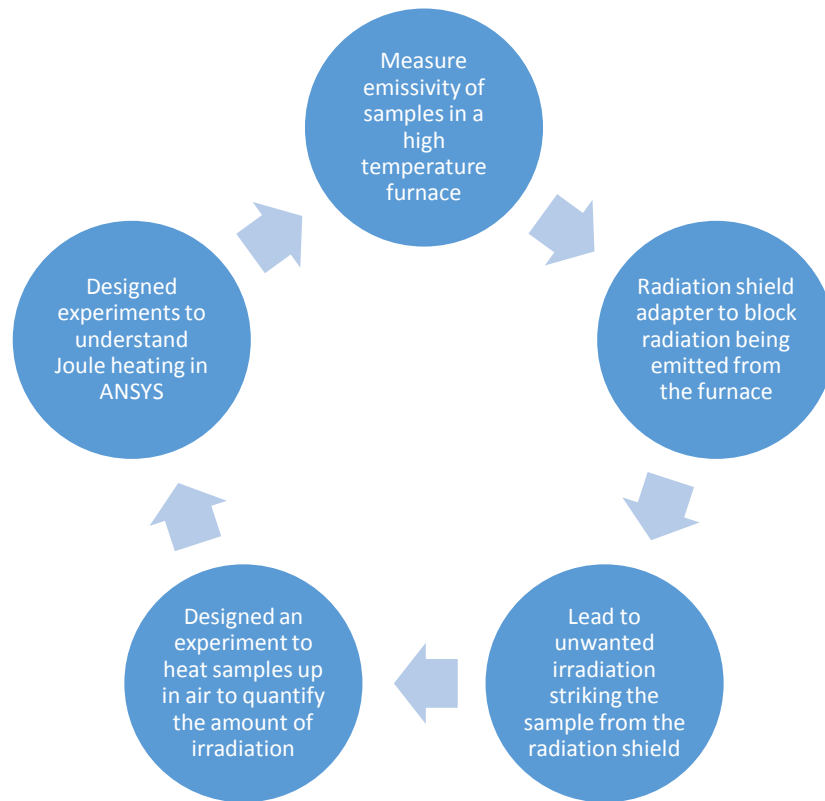


Figure 1-1 Experimental cycle diagram

1.1 Objective

The overall objective is to develop a method for measuring spectral, directional emittance of stainless steel 304 and titanium AL-4V at elevated temperatures. In order to accomplish this, a preexisting furnace capable of reaching an internal temperature of 1200°C was selected to heat the samples to the temperatures of interest. However, to block the radiation emitted from the furnace during measurements, a cold tube must be slid over the sample during measurements to block this emittance. This involved designing a cooling adapter chamber to house the cold tube that would block the radiation emitted by the furnace when measurements are taken.

A second investigation began to quantify the amount of radiation that is emitted from the sample onto the cold tube, and reflected back to the sample. This investigation involved Joule heating the NASA samples in ambient air to the temperatures reached in the furnace. To assist in the design, ANSYS Workbench 16.0 was utilized to predict the temperature distribution across the sample given a set current.

Due to uncertainties in the ANSYS simulations when research first began, a third investigation was launched to verify the accuracy of the ANSYS simulations. This investigation consisted of two sets of simulations where a graphite rod was heated with direct current, and the thermal profile of the graphite rod was compared to the simulation results. The first set was an experiment conducted in ambient air while the second set were experiments conducted in a vacuum environment.

2 THEORY

The objective of this chapter is to describe the radiation theory employed in this work. This includes discussing heat transfer, measuring spectral, directional emissivity at elevated temperatures, and radiosity. This chapter will also discuss Joule heating and a thermal energy balance of a cylinder.

2.1 Radiation Theory

Radiation heat transfer is a complex process that depends on many factors regarding the surface that is radiating, the surface receiving radiation, and the medium between two surfaces. The second heat flux equation, Eq. 2-2, calculates heat flux due to convection where heat flux is equal to the heat transfer coefficient (h), times the difference of the surface temperature (T_s) and the ambient temperature (T_∞). The first heat flux equation calculated conduction

$$q_{\text{cond}}'' = -kx \quad (\text{Equation 2-1})$$

where k is the thermal conductivity of the material and x is the length. The heat flux due to convection is

$$q_{\text{conv}}'' = h(T_s - T_\infty) \quad (\text{Equation 2-2})$$

where h is the heat transfer coefficient, T_s is surface temperature and T_∞ is the ambient temperature. The final heat flux equation defines that heat flux due to radiation

$$q_{\text{rad}}'' = \varepsilon\sigma * (T_s^4 - T_{\text{sur}}^4) \quad (\text{Equation 2-3})$$

where ε is the emissivity of the material and σ is the Stefan-Boltzmann constant.

Radiation heat flux is the major source of heat flux at high temperatures due to the

temperatures being to the fourth power when calculating radiation heat flux as opposed to conduction and convection where only the linear relationship between temperatures is calculated. The emissivity for a material can range from 0-1, with 1 representing the emissivity of a blackbody, the idealized perfect absorber of incident radiation (Modest).

2.1.1 Blackbody Theory

A blackbody provides a limit on the radiation emission and absorption for a prescribed temperature and wavelength. For a blackbody, the spectral emissive power at a certain temperature and wavelength (λ) is described by Planck's law

$$E_b(T, \lambda) = \frac{2\pi h_0 c^2}{\lambda^5 e^{\frac{h_0 v}{k_b \lambda T}} - 1} \quad \text{(Equation 2-4)}$$

where h_0 is Planck's constant, c is the speed of light, and k_b is the Boltzmann constant.

The Boltzmann constant relates heat to random thermal motions at the particle level for a specified temperature (Incropera). By analyzing the blackbody emissive power spectrum in Fig 2-1, a representation of Eq 2-4, it becomes apparent how radiation heat flux increases exponentially with increasing temperature as stated previously (Modest).

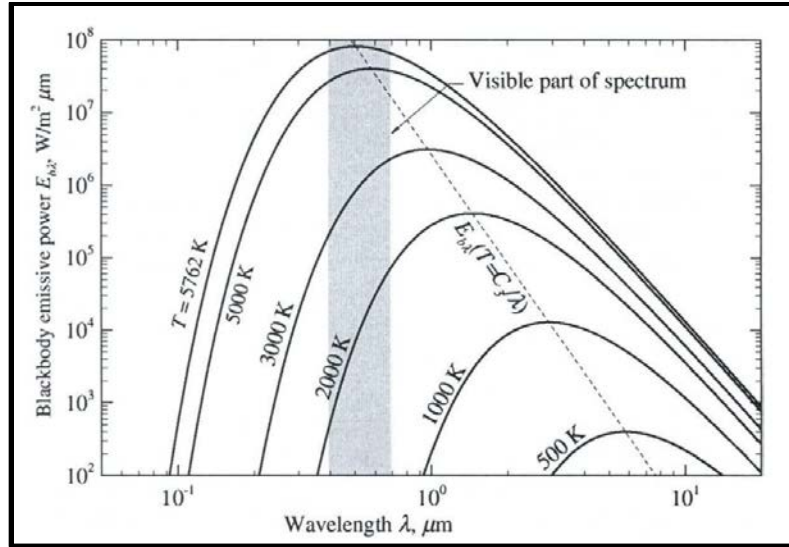


Figure 2-1 Spectral blackbody emissive power (Modest)

2.1.2 Emissivity Theory

Emissivity is a measure of how efficient a material emits thermal energy compared to a blackbody. There are four ways to characterize emittance:

- 1) Spectral, directional emittance
- 2) Spectral hemispherical emittance: a directional average of spectral directional emittance.
- 3) Total directional emittance: spectral average of spectral directional emittance
- 4) Total hemispherical emittance: directional and spectral average of spectral directional emittance.

In this work, spectral, directional emittance is studied where the emissivity is a ratio of the intensity, $I_{\lambda,e}$ at a specific wavelength, direction and temperature compared to the intensity of a blackbody, $I_{\lambda,b}$, at the same wavelength and temperature.

$$\varepsilon_{\lambda,\theta}(\lambda, \theta, T) \equiv \frac{I_{\lambda,e}(\lambda, \theta, \varphi, T)}{I_{\lambda,b}(\lambda, T)} \quad (\text{Equation 2-5})$$

The different angles associated with direction are the directional angle, θ , and the azimuth variation φ . The azimuth variation is usually low and will be neglected for this study. However, the directional elevation will be taken into account as stated previously in Chapter 1.

2.1.3 Blackbody Design

The blackbody intensity must be measured to calculate emissivity, and the blackbody should be confirmed to be a blackbody. First, a blackbody must be designed. It has been shown in previous works that an isothermal cavity with a high depth to radius ratio may be an idealized blackbody. Additionally, a blackbody may be accomplished at a lower length to radius and lower emissivity if there is a flat ring with a smaller hole radius partially covering the cavity. This was studied by Alfano and Sarno, and a summary table of their findings is published in Modest, Fig. 2-3. Implementing a small radius hole would complicate the design, and increase manufacturing costs. In Fig. 2-2, ϵ_a is the apparent emissivity defined as the emissivity that the blackbody cavity will have. The emissivity in Fig 2-2, is the emissivity that the blackbody cavity is manufactured in.

Apparent emittance, $\epsilon_a = J/\sigma T^4$, at the bottom center of an isothermal partially covered cylindrical cavity [20, 21].

ϵ	R_i/R	ϵ_a		
		($L/R = 2$)	($L/R = 4$)	($L/R = 8$)
0.25	0.4	0.916	0.968	0.990
	0.6	0.829	0.931	0.981
	0.8	0.732	0.888	0.969
	1.0	0.640	0.844	0.965
0.50	0.4	0.968	0.990	0.998
	0.6	0.932	0.979	0.995
	0.8	0.887	0.964	0.992
	1.0	0.839	0.946	0.989
0.75	0.4	0.988	0.997	0.999
	0.6	0.975	0.997	0.998
	0.8	0.958	0.988	0.997
	1.0	0.939	0.982	0.996

Figure 2-2 Apparent emittance from an isothermal cylindrical cavity

In order to confirm that the blackbody designed for our setup is a blackbody, its intensity must be compared to Planck's curve, Fig. 2-1, at the specified measured wavelength and temperature.

2.1.4 Reflected Radiation

One source of error investigated in this study is radiation that is emitted from the sample, striking the radiation shield, and then being reflected back to the sample. This is a two part process which first involves the irradiation, the rate at which radiation is incident upon a surface area, in this case, the rate at which radiation is irradiated from the sample to the radiation shield when the shield is slid over the sample. Next, this radiation is reflected back to the sample along with radiation that may be emitted from the radiation shield itself given the shield temperature (Incropera). This total radiation is called radiosity, J , and is written as

$$J = E + G_{\text{ref}} \tag{Equation 2-6}$$

where E is radiation emitted by the tube and G_{ref} is the reflected radiation .

2.1.5 View Factors

In order to compute the radiation exchange between surfaces, view factors must be understood. View factors are defined as the fraction of energy leaving a surface that is intercepted by another surface. This view factor between two surfaces, i and j , is defined with Figure 2-3 (Modest) and

$$dF_{dA_i-dA_j} \equiv \frac{\text{diffuse energy leaving } dA_i \text{ directly toward and intercepted by } dA_j}{\text{total diffuse energy leaving } dA_i} \quad (\text{Equation 2-7})$$

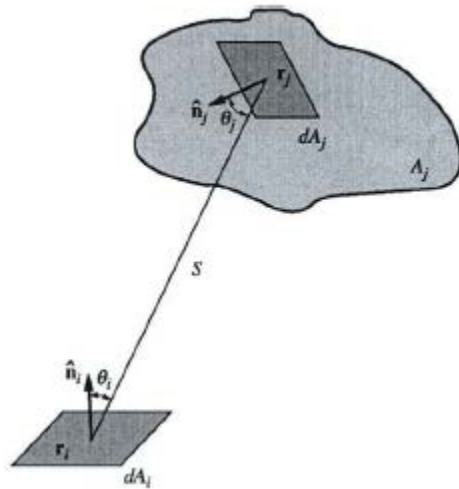


Figure 2-3 Pictorial representation of surface A_i and surface A_j

In order to calculate view factors, there are two important equations. The first is the law of reciprocity

$$A_i F_{A_i-A_j} = A_j F_{A_j-A_i} \quad (\text{Equation 2-8})$$

where the area surface 1 is A_i , the area of surface 2 is A_j , the view factor from area 1 to 2 is $F_{A_i-A_j}$ and $F_{A_j-A_i}$ is the view factor from area 2 to 1. The second equation is the summation rule. (Incropera).

$$\sum_{j=1}^N F_{ij} = 1 \quad (\text{Equation 2-9})$$

To calculate view factors there are three approaches: direct integration, where view factors are expressed in terms of double surface integrals, statistical integration by using the Monte Carlo method, and view factor algebra, a set of methods used to determine view factors with simple algebraic equations. The latter one is used in this thesis to calculate view factors. For many geometric arrangements between two surfaces, the view factors have been calculated in previous research and these solutions are readily available via heat transfer books or journal articles (Modest).

2.2 Joule Heating

Joule heating, commonly known as resistive or Ohmic heating, is the conversion from electrical to thermal energy. This is seen in quite a few applications including electric heating, electric fuses, and the incandescent light bulb. Joule heating is defined as

$$\dot{E}_g = I^2 R \quad (\text{Equation 2-10})$$

where I is the current and R is the resistance. The heat generated due to Joule Heating is then

$$\dot{q} = \frac{\dot{E}_g}{\text{Volume}} = \frac{I^2 R}{\text{Volume}} \quad (\text{Equation 2-11})$$

These two equations show that the heat generated by Joule heating is proportional to the current squared multiplied by the resistance over the volume.

The resistance is defined by the material used in heating:

$$R = \frac{\rho L}{CS} \quad (\text{Equation 2-12})$$

where ρ is the resistivity of the material, L is the length, and CS is the cross sectional area. Resistivity also varies with temperature. Previous research conducted has shown that graphite's resistivity varies significantly with temperature and that its resistivity may only be 91% of the original resistance following heating up to 1200°C (Noyes).

In the Joule heating experiments, the resistivity of graphite was calculated from the voltage and current outputted by the DC power supply from Ohm's law. Since copper has a much lower resistivity than graphite, the resistivity of copper in the feed lines was neglected. The power supply outputs the voltage needed to push a set current through a resistor. Thus, the resistivity of graphite was extracted by using Eq. 2-13 and Ohm's law:

$$V = IR \quad (\text{Equation 2-13})$$

2.3 Thermal Energy Balances in Cylindrical Coordinates

In this work, the surface temperature of various materials is calculated with simulations and measured numerically for cylindrical rods. The simulations calculate the amount of heat generated and the temperature distribution by performing energy balances between the system and boundary conditions defined by the user. Thus, it is critical to understand the thermal principles behind these calculations

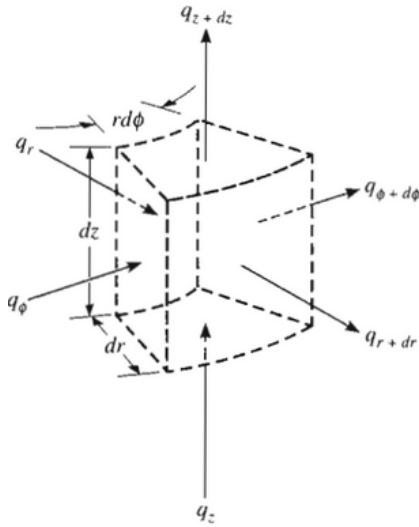


Figure 2-4 Controlled volume in cylindrical coordinates

If a controlled volume is defined as in Figure 2-4, and is assumed to have a homogenous material with no work being done on the system, then only thermal energy is considered.

An energy balance is calculated for the control volume to yield

$$\frac{1}{r} \frac{\delta}{\delta r} \left(kr \frac{\delta T}{\delta r} \right) + \frac{1}{r^2} \frac{\delta}{\delta \phi} \left(k \frac{\delta T}{\delta \phi} \right) + \frac{\delta}{\delta z} k \left(\frac{\delta T}{\delta z} \right) + \dot{q} = \rho c_p \frac{\delta T}{\delta t} \quad (\text{Equation 2-14})$$

where r is the radius, z is the vertical distance, and c_p is the specific heat. This allows the temperature distribution to be a function of time (t).

Once the graphite rod used in the experiments reaches steady state, the temperature distribution across the rod will remain constant and the right side of equation 2-14 will equal 0.

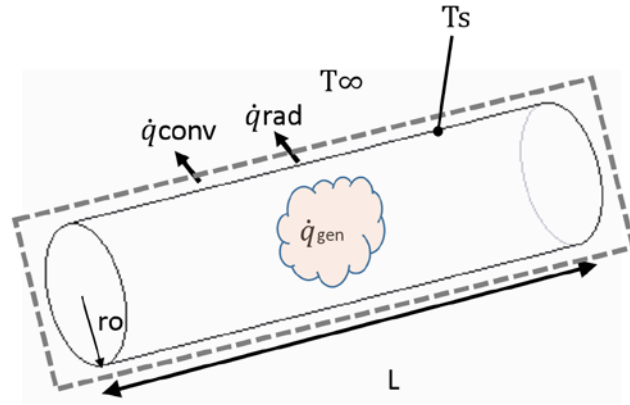


Figure 2-5 Uniform heat generation in a cylinder

An energy balance may be performed to determine the surface temperature of the rod shown in Figure 2-5 similar to the graphite rod analyzed in Chapters 4 and 5 of this thesis where heat convection and radiation are considered while the rod is undergoing constant heat generation in the form of Joule heating. Equation 2-15 is the result of this energy balance at a localized position, L , assuming that the graphite rod is at steady state.

$$\dot{q}(\pi r_o^2 L) = h(2\pi r_o L)(T_{sL} - T_\infty) + (2\pi r_o L)(T_{sL}^4 - T_\infty^4) \quad (\text{Equation 2-15})$$

3 LITERATURE REVIEW

There have been different experimental setups to measure emissivity at high temperatures. If knowledge of only total, hemispherical emittance is needed, a method called calorimetric emission measurement can be utilized. This is done by suspending a sample in a testing chamber with cooled walls, and heating the sample up with a set current. The temperature of the walls and sample are monitored with thermocouples, and thus when the sample reaches a steady state temperature, the heat generated with current is compared to the radiative heat loss of the same to the sphere. However, spectral, directional emittance is needed and thus this method is not applicable (Funai, 1963).

Measuring a material's reflectance is another method for calculating a material's emittance. This method involves an isothermal heated cavity and a sample at the same temperature suspending inside of the furnace. The wall of the cavity is assumed to be a blackbody since it is an isothermal enclosure, and thus measurements of the wall are compared to that of the sample. Since the whole cavity and sample must be isothermal, the primary source of error is not having an isothermal cavity. This is the reason why this method is limited to the lower temperature regimes (Zarwoski, 1996).

Research has been done using a long, isothermal cylinder as a blackbody. It has been shown through calculations using the kernel approximation method, and the method of successive approximation, that an isothermal cylinder with a large length to radius ratio may have an emissivity close to one if the material has an apparent emissivity greater

than 0.5. This is the principle in which many of the blackbody furnaces are built upon (Alfano, 1975).

The most common approach to measuring spectral, directional emissivity at high temperatures is to measure the emission of a sample and compare to a blackbody at the same temperature and wavelength utilizing one detector and optical path. The setups vary mainly in the type of blackbody reference. Szeles and Wolfe developed a setup that utilized a separate reference blackbody that is kept at the same temperature as the test specimen. This requires precise knowledge of the temperature of the test specimen, and a feed-back loop controller to set the temperature of the blackbody. This is a common setup that is used in many experiments investigating emissivity such as those conducted by Markham, Soimon, and Best. Instead of designing a blackbody and temperature controller, it is also possible to purchase blackbody furnaces commercially from manufactures such as Chino and Pegasus. However, these blackbodies often cost upwards of \$10,000.

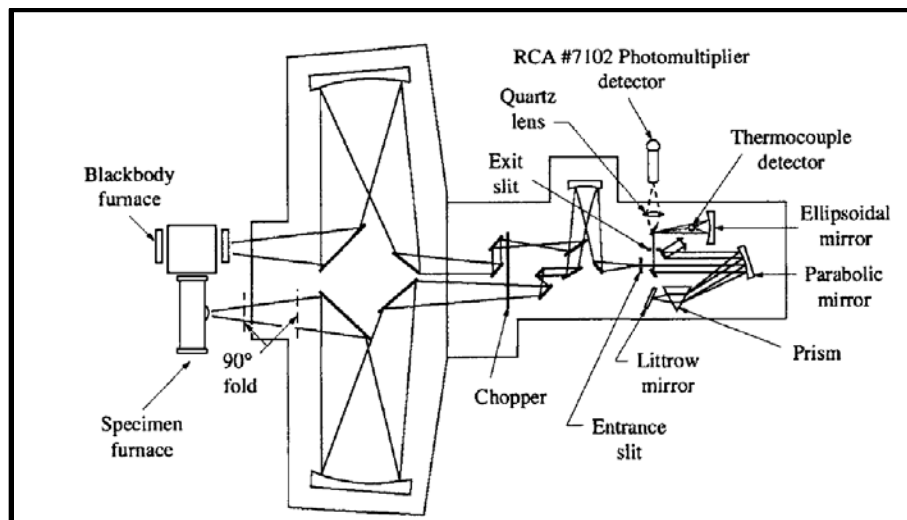


Figure 3-1 Szeles and Wolfe setup with a separate blackbody

For high temperatures, it is less complicated to integrate the blackbody into the setup as long as the blackbody and the sample are isothermal. One group of researchers have placed the sample of interest on a moveable rod located in a blackbody cavity, Figure 3-2. For the blackbody measurement, the sample is located deep inside of a blackbody cavity to reach high temperatures and blackbody measurements are taken. Then the sample is quickly moved out of the furnace and measurements are taken again. However, one disadvantage to this setup is that it is difficult to remove the sample quickly enough so that it stays at the same temperature when the black body measurement was recorded. It is also difficult to ensure that the graphite heater tube is at a constant temperature. Furthermore, this method may only be used for normal emissivity measurements and not directional emissivity measurements (Atkinson and Strange, 1994).

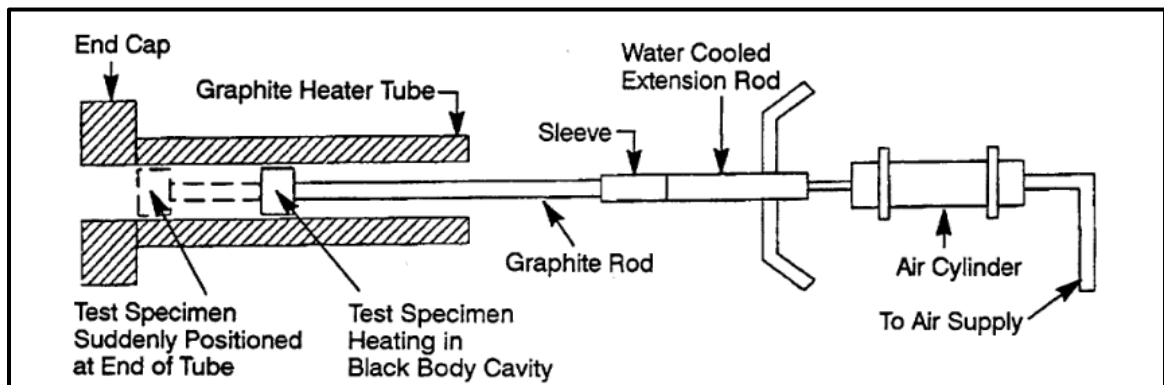


Figure 3-2 Experimental setup with a moving sample (Atkinson and Strange)

The setup utilized in this work is similar to Figure 3-3. In this setup the sample of interest and a blackbody are heated in a furnace to a prescribed temperature. During emission measurements, a tube covers the sample to block the radiation of the furnace. Measurements were done in seconds with an FTIR spectrometer to prevent heating of the tube and cooling of the sample (Postlethwait et al, 1994).

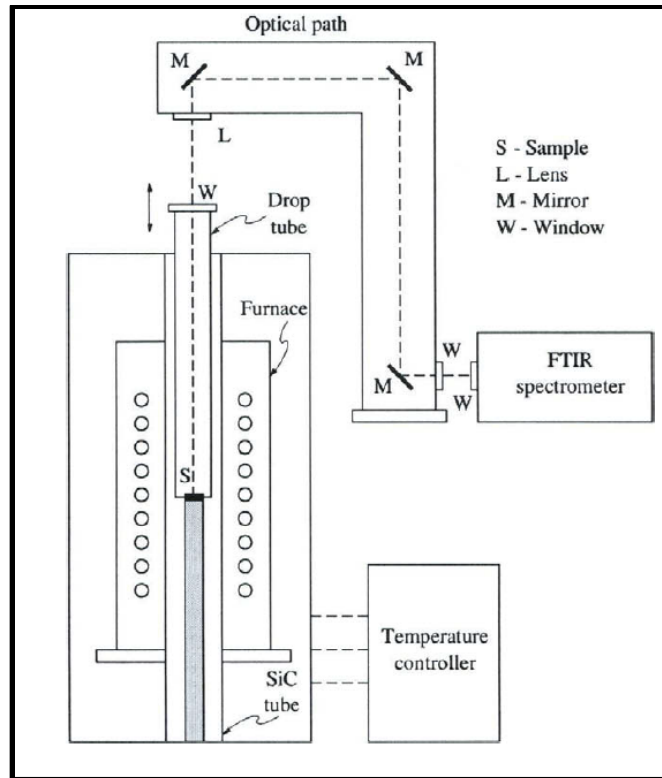


Figure 3-3 Schematic of experimental setup (Postlethwait et al, 1994)

4 AMBIENT AIR JOULE HEATING SIMULATION AND EXPERIMENT

The objective of this chapter is to describe the experimental method and finite element analysis model developed for determining the maximum temperature and temperature profile of a high density graphite, 1.76 g/cm^3 , when electrically heated with a direct current in ambient air. The purpose of these experiments were to aid in understanding ANSYS simulations for joule heating used to design experiments to quantify emissivity error. Experiments were conducted in air with currents up to 100 amperes. This limit was chosen due to preliminary results from the simulations which indicated that above 100 amperes the graphite may reach temperatures above 400°C . According to the manufacturer, the graphite should only be operated below 400°C in ambient air to avoid oxidation.

4.1 Experimental Setup

The objective of this chapter is to describe the experimental setup and procedure for determining the maximum temperature and temperature profile of graphite in ambient air with an applied direct current to verify the maximum temperature and profile calculated with finite element analysis for ambient air. This involved: (i) selecting materials and shapes to heat graphite efficiently and safely; (ii) measuring the temperature of the graphite at three locations and the temperature of the two copper clamps; and (iii) applying a known direct current across the graphite.

This setup, Fig. 4-1, consisted of four materials: graphite, copper, aluminum, and calcium silicate. Copper is a common material used in electrical applications and was chosen for its low electrical resistivity and high melting point temperature. Aluminum served as an

economical anchor for the copper to the optical table. To insulate the optical table electrically, wood was chosen ($\rho=1 \times 10^{16} \text{m} \cdot \Omega$) (Stamm). Likewise, to insulate the wood thermally from the experiment, high-temperature calcium silicate 1/2" thick was chosen due its low thermal conductivity of $0.05 \text{ W}/(\text{m} \cdot \text{K})$ - $0.12 \text{ W}/(\text{m} \cdot \text{K})$ from 0°C - 1000°C (Salmon).

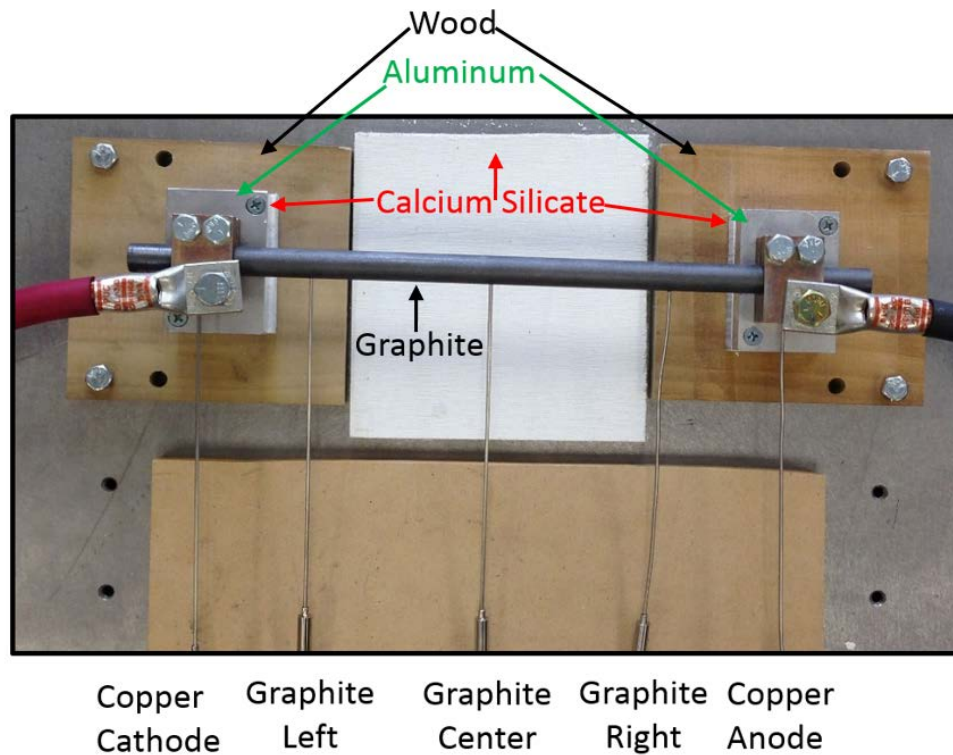


Figure 4-1 Photo of ambient Joule heating setup

4.1.1 Temperature Measurement and Recording:

In order to measure the maximum temperature of graphite and its thermal profile, type K Inconel sheath mineral insulated thermocouples were utilized for temperature measurement. The mineral insulation provides an underground junction to electrically isolate the thermocouple from the current flowing through the system.

Three 1/16” diameter holes were drilled 1/8” radially into a 1/2 diameter graphite rod as shown in Figure 4-2 to place the thermocouples. To monitor the temperature, a similar hole was drilled into both of the copper clamps. Finally, a sixth thermocouple was utilized during the experiment to determine the ambient temperature of air.

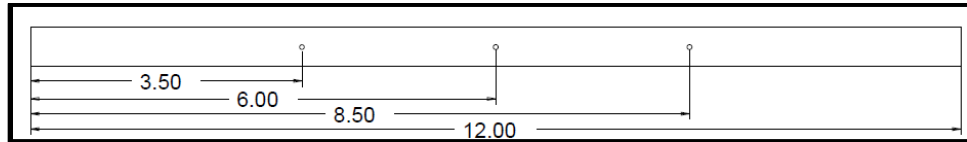


Figure 4-2 Thermocouple locations (inches) on the graphite rod for ambient air Joule heating experiment

The thermocouples were connected to a NI-cDAQ -9178 unit with an NI 9213 16 channel thermocouple module. The temperatures from the thermocouples were then analyzed and recorded with LabView 2011 at a sample rate of 60 samples per minute. The thermocouples have a standard error of the largest value of $\pm 2.2^{\circ}\text{C}$ or $\pm 0.75\%$ of the thermocouple reading.

4.1.2 Electrical Control

Direct current was generated with a Magna-Power XR16-250/208 power supply. This power supply may generate 4000 watts total with a maximum current of 250 amperes. According to the manual, the current outputted by the power supply is within $\pm 0.2\%$ of the user input current. Current was carried to the copper clamps via 3/0 AWG wire that has a maximum capacity of 275 amperes. Figure 4-1 illustrates the experimental setup.

4.1.3 Experimental Procedure:

- 1) Current was applied to the system starting at 10 amperes.
- 2) After the temperature stabilized in the center of graphite for 60 seconds within $\pm 0.2^\circ\text{C}$, the current was stepped up 10 amperes.
- 3) Steps 1 and 2 were repeated up to 100 amperes.

4.2 Experimental Results

Figure 4-3 and Fig. 4-4 displays the maximum measured temperatures at the five locations in the ambient air experiment. The experimental results show that the maximum temperature occurs in the center of the graphite rod for every trial.

Additionally, in every trial the graphite left was slightly cooler than the graphite right.

This may be due to the graphite not being centered perfectly between the copper anode and cathode.

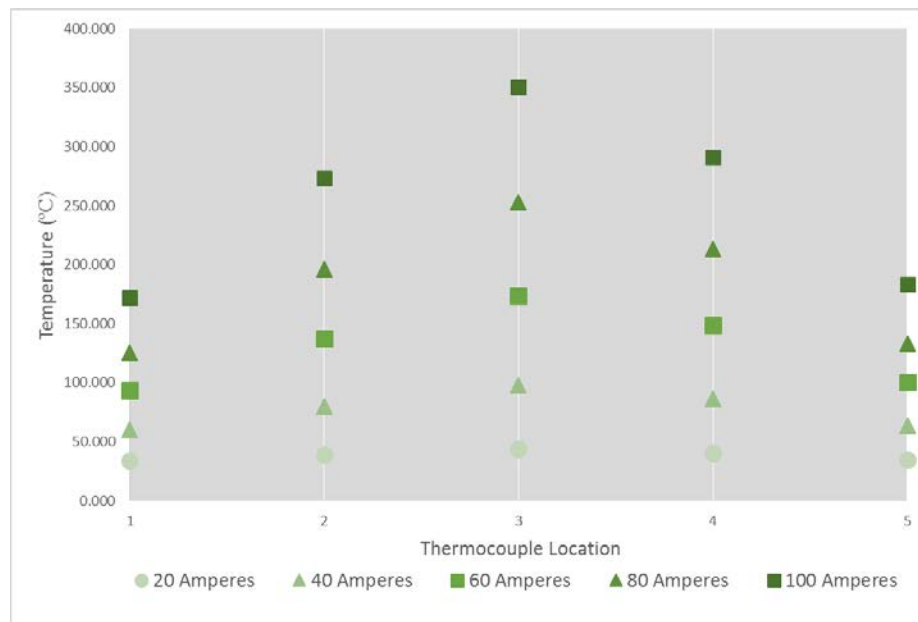


Figure 4-3 Experimental results displaying the maximum temperature at each thermocouple location

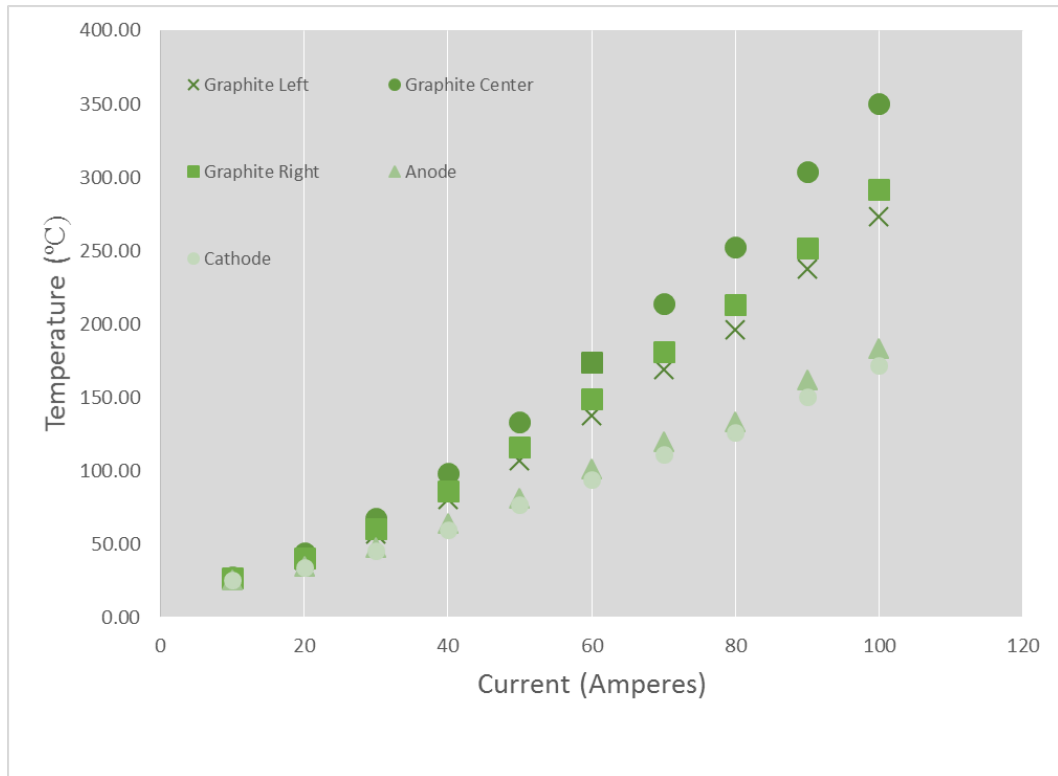


Figure 4-4 Current vs Temperature for all five locations

Figure 4-5 displays that the center of graphite heats up quicker than the rest of the sample. The left and right midpoints of the graphite rod heat up quicker than the copper clips. As expected, this shows that the largest Joule heating is occurring in the graphite which is to be expected due to graphite's higher resistivity than copper. The other two graphite locations and copper clamps have a slower heating rate because those four points are being heated conductively from the center of graphite.

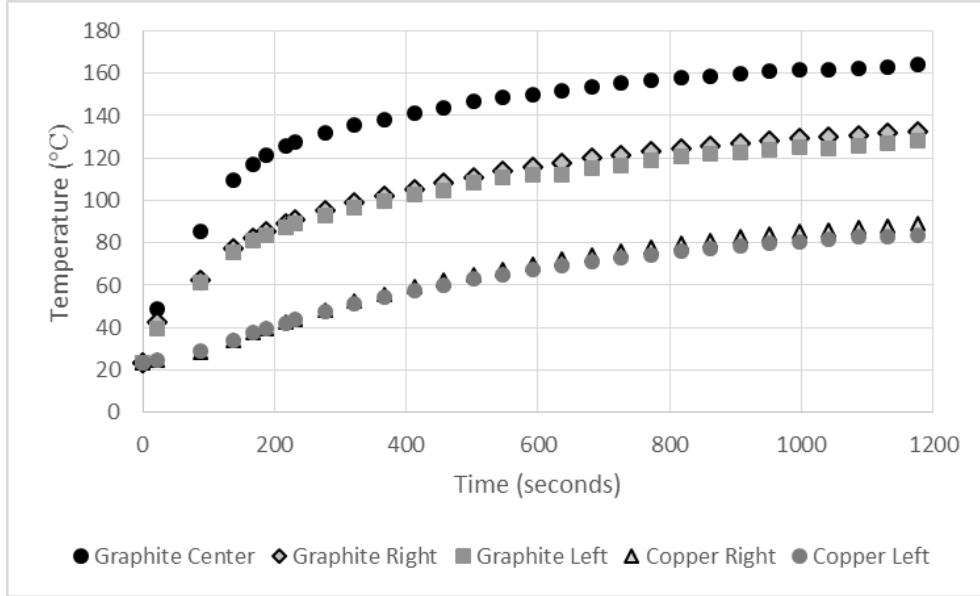


Figure 4-5 Measured temperature profiles at 60 amperes

4.3 Ambient Air Joule Heating Simulation

A finite element analysis (FEA) model was developed and executed with ANSYS Workbench 16.0. The model was built with the thermal electric modular. For this experiment, two models were run with different boundary conditions. The results of these two are compared, and will later be compared to the measured experimental results.

Table 4-1 Test case matrix for ANSYS simulations

<i>Case No</i>	<i>Boundary Conditions</i>	
	Measured Copper Temperature	Calculated Heat Convection Values (Tables 4-2, 4-3 4-4)
1		X
2	X	X

4.3.1 Geometry and Mesh Size

An accurate geometry of the experimental setup was constructed. This included the materials and dimensions in the experimental setup excluding the wooden base. The mesh size was chosen to be medium yielding 8068 nodes and 1337 elements, compared to a fine mesh that yields approximately 17,000 nodes and 3,000 elements. The mesh size choice was based on time for the simulation to run, and the variance of results. It was noted that the temperature profile and maximum temperature did not vary significantly between a medium and fine mesh.

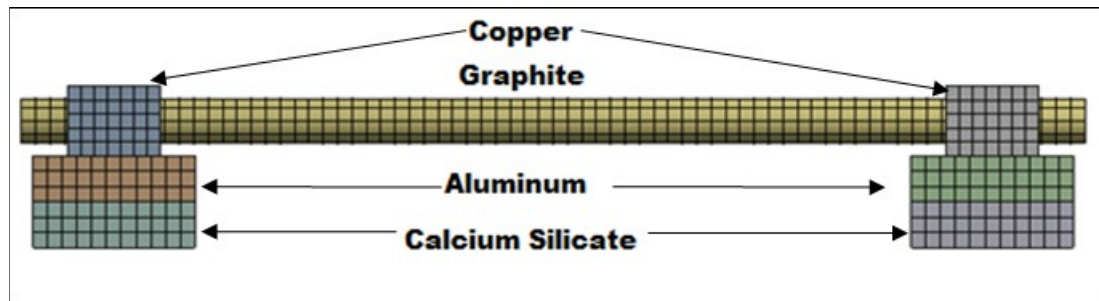


Figure 4-6 Geometry with meshing for ambient air Joule heating simulation

4.3.2 Boundary Conditions

Boundary conditions were applied to the model to closely resemble the heat transfer that would take place in the experiment. An electrical boundary condition of 0 voltage was applied to the top of one of the copper clips. On the top face of the opposite copper clip, a boundary condition was applied depending on the applied current being modeled. Radiation was applied to the graphite rod with an emissivity of 0.95 radiating to the atmosphere at 22°C. Next, it was assumed that the temperature of the bottom of the calcium silicate remained constant at 22°C due to the very low thermal conductivity of calcium silicate. Additionally, convection was applied to the cylinder depending on the

experimental value for the surface temperature of the rod. Convection was calculated by first calculating the dimensionless Grashof number, the ratio of buoyant to viscous forces, for various surface temperatures of dry air at atmospheric pressure. The Prandtl number was also given for these surface temperatures, and thus the Rayleigh number could be determined. Finally, the air flow was determined to be laminar from the Grashof number (Bejan). These calculations and results are available in Appendix 3.

4.3.3 Material Properties

Table 4-2 lists the thermal conductivity for the materials that were applied to the bodies in the simulation. Resistivity of the material was calculated using Ohm’s law, Eq 2- based on the voltages measured in chapter 4, experimental setup 1.

Table 4-2 Thermal conductivity of materials (Touloukian)

	Thermal Conductivity W/(m*K)
Aluminum	155
Copper	400
Graphite	130

4.3.4 Simulation Results

Figure 4-7 and Figure 4-8 correspond to the thermocouple locations used in the experiment. In all cases the maximum temperature was located in the center of the graphite rod. The temperature decreases as the location gets closer to the copper clips. Both simulation cases have symmetric thermal profiles. When the calculated values for the heat convection coefficients for the plates are used, as opposed to holding the copper clips at a constant temperature, higher temperatures result. At 100 amperes in simulation case 1, the difference of the copper clips compared to the center of graphite in

temperature is 177°C. At 100 amperes in case 2 the difference of the copper clips compared to the center of graphite is 164°C. It is also seen from Figure 4-7 and Figure 4-9 that the temperature profiles are similar for case 1 and case 2.

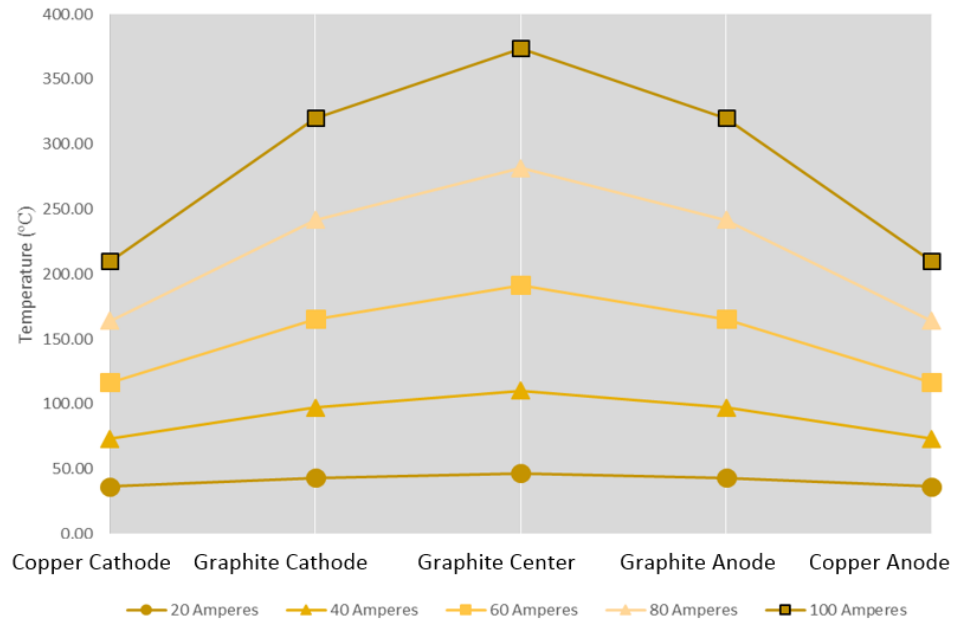


Figure 4-7 Simulation case 1: temperature profile graph

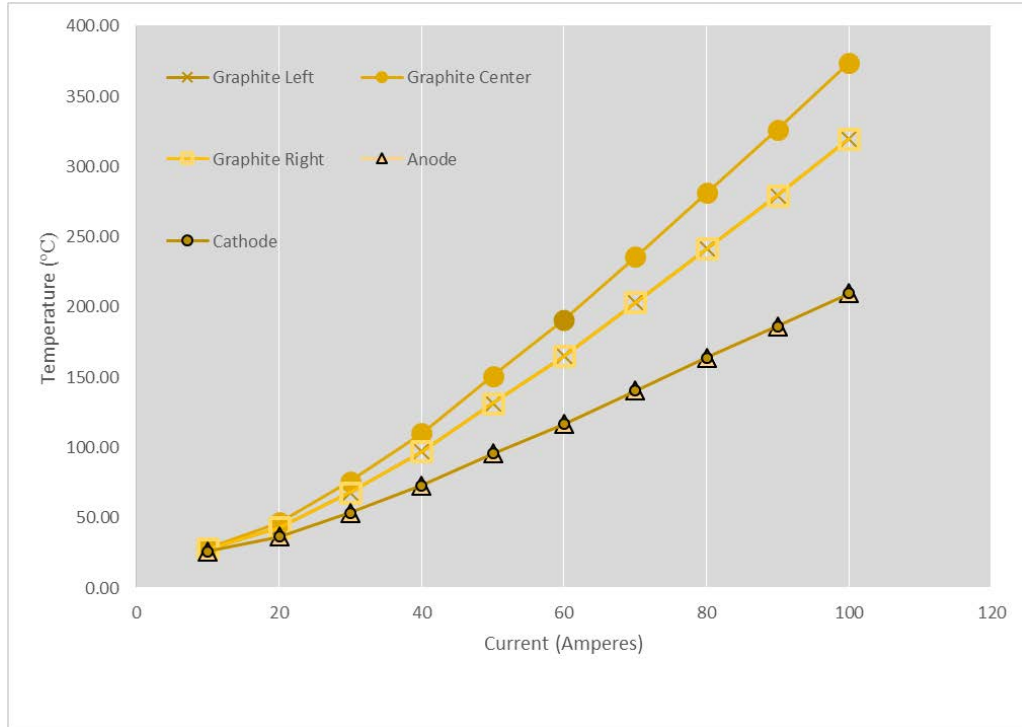


Figure 4-8 Simulation case 1: current vs temperature graph

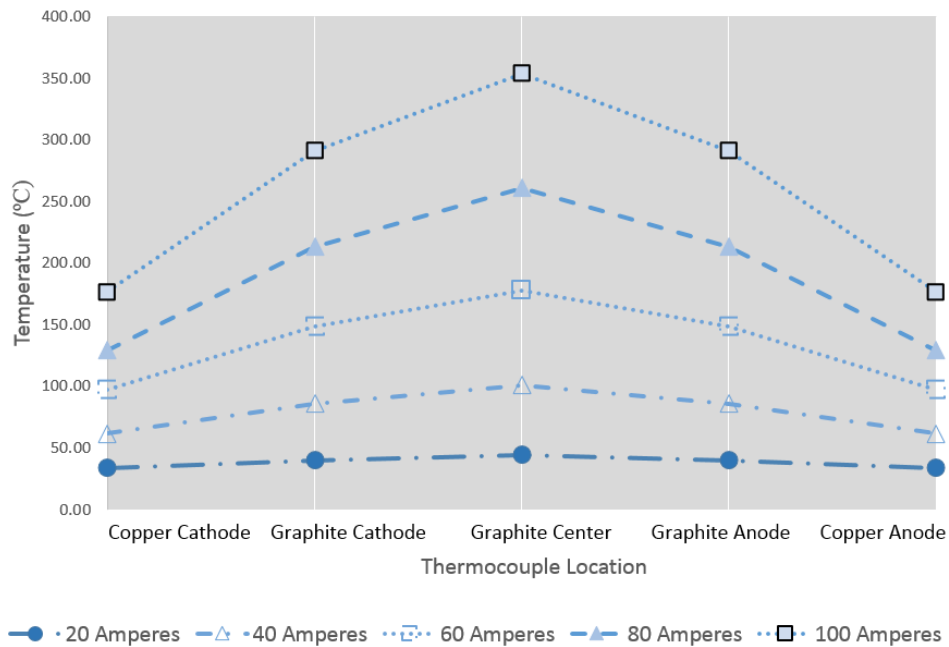


Figure 4-9 Simulation case 2: temperature profile graph

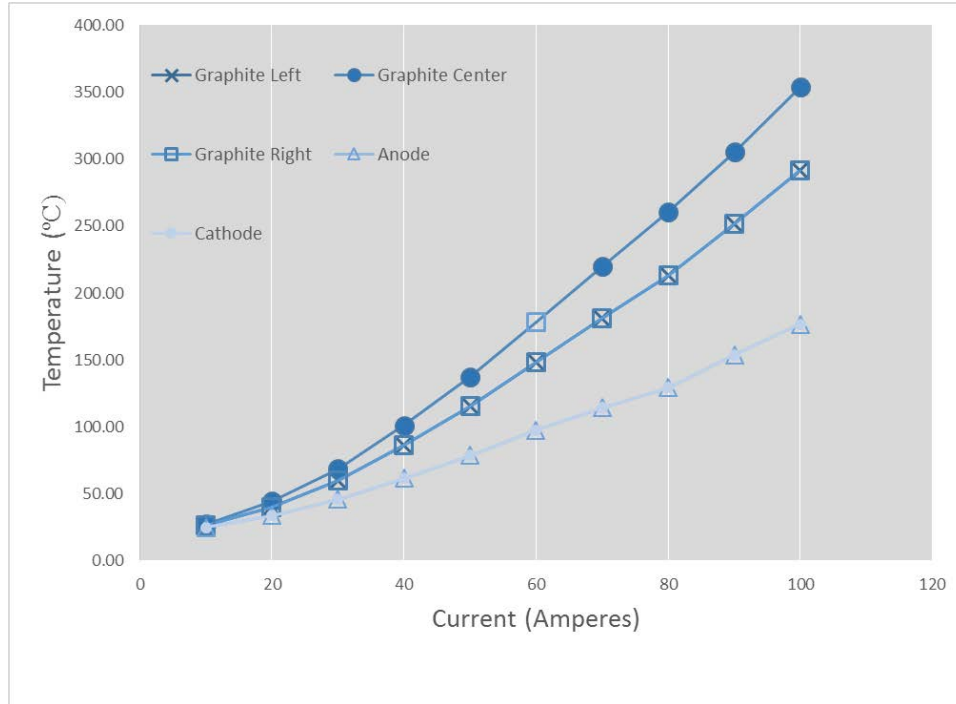


Figure 4-10 Simulation case 2: current vs temperature graph

4.4 Conclusions

Both simulations are fairly accurate at 10 and 20 amperes by comparing the results to the measured values as shown in Figure 4-11. Case 2 has a more accurate temperature profile of the graphite compared to case 1 since 2 used the measured results from the experiment as one of the boundary conditions.

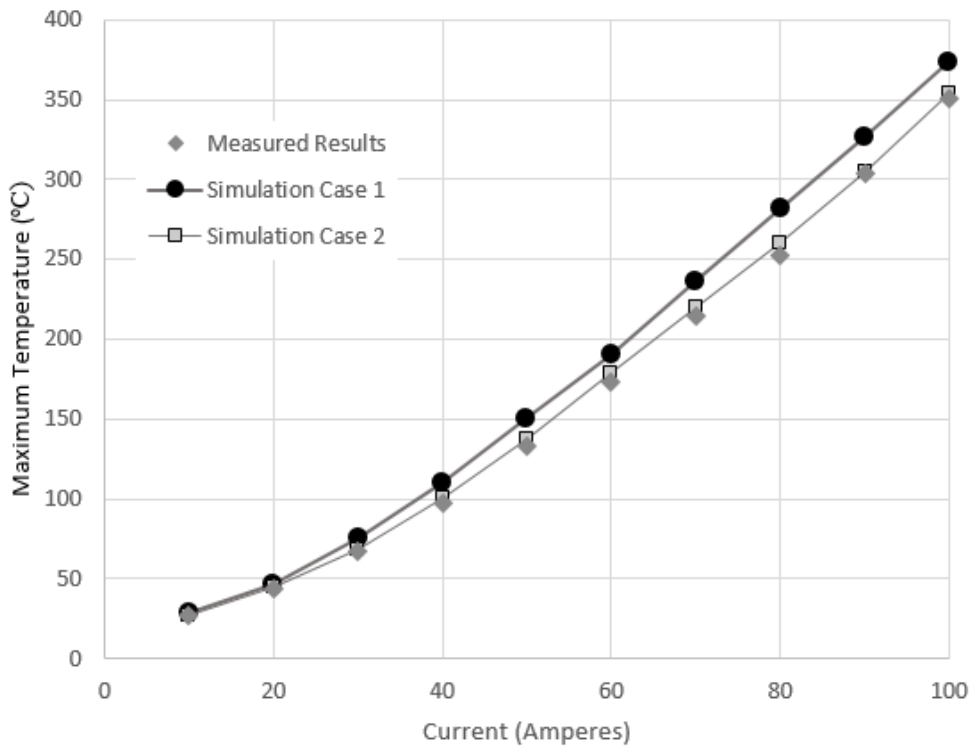


Figure 4-11 Maximum measured temperatures of measured and simulated cases

Figure 4-12 displays that symmetrical surface temperature was not measured during the experiment. This may be due to the graphite rod not being perfectly centered between the two copper clamps. This may have also been observed due to incomplete contact between the thermocouples and graphite at several locations. Furthermore, this could be due to the graphite not being homogenous in material, resulting in a variation of thermal conductivity along graphite axially.

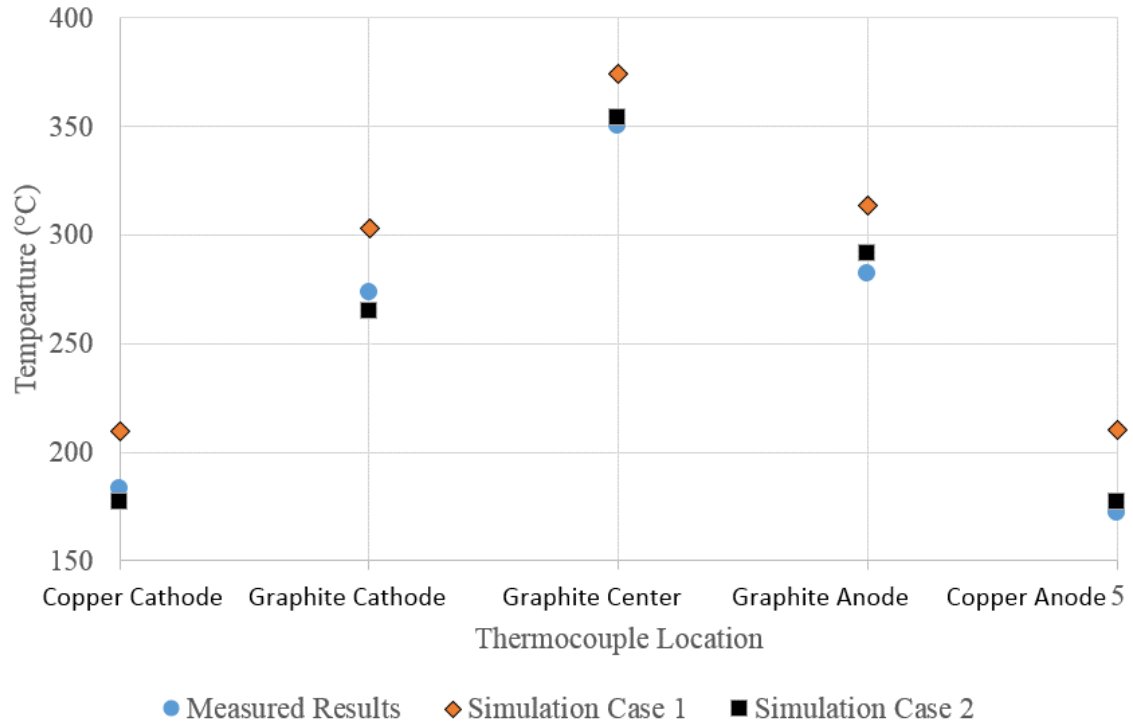


Figure 4-12 Maximum temperature comparison between measured results, simulation case 1, and simulation case 2 at 100 Amps

The percent differences for each case are reported in Table 4-3 were calculated based on Eq. 4-6.

$$\text{percent difference} = \left| \frac{(\text{simulated value} - \text{experimental value})}{\text{experimental value}} \right| \times 100\% \quad (\text{Equation 4-1})$$

After 20 Amperes, the percent difference for case 1 rises to over 12 percent, and continues to be above 10% until 90 amperes. For case 2, the percent difference never rises above 3.2%. For both cases, the largest percent difference is at 50 amperes. For the applications of our ANSYS simulations, the percent difference reported is acceptable. This is due to not have knowledge of the thermal conductivity of graphite beyond what the manufacturer stated. Furthermore, this percent error is acceptable since the

simulations will be used to design experiments to hit target temperatures. Thus, experiments that are designed in the future based on the ANSYS simulations will account for this percent difference

Table 4-3 Percent difference for simulation case 1 and case 2

Current (Amperes)	Case 1 Percent Difference	Case 2 Percent Difference
10	4.7%	0.8%
20	5.6%	0.5%
30	12.6%	2.1%
40	12.5%	3.2%
50	13.2%	3.2%
60	10.2%	2.5%
70	10.1%	2.5%
80	11.3%	3.1%
90	7.2%	0.4%
100	6.7%	0.9%

5 VACUUM JOULE HEATING SIMULATION AND EXPERIMENT

The objective of this chapter is to describe the experimental setup and the finite element analysis model developed for determining the maximum temperature and temperature profile of a material when electrically heated with a direct current in a vacuum environment. The heat transfer coefficient value becomes very important for the experiment conducted in a non-vacuum environment. Furthermore, knowledge of the resistivity of graphite and how it changes with temperature is equally important in determining the heat flux added to the system. Tests were conducted with two samples of graphite, a virgin graphite rod (previously not heated) and a preheated graphite rod that had already experienced the same current and similar temperatures. Experiments were conducted in a vacuum chamber with water cooled copper anodes and cathodes to eliminate the effects of convective cooling to the ambient air, to reach high surface temperatures on the graphite, and to protect the graphite from oxidation. Below is a table of the three test cases with conditions performed for this setup.

Table 5-1 List of test case conditions for experiments

<i>Test Case Number</i>	<i>Test Conditions</i>			Current Range (Amperes)
	Atmospheric Pressure	Vacuum Pressure	Water Cooling	
1	X			20-80
2	X		X	20-100
3		X	X	10-250

5.1 Experimental Setup

The experiment was setup inside of a Kurt. J. Lesker C6-0600 six way cross. Three of the six flanges were custom built for this experiment. Two flanges were used for

electrical input while the remaining flanges were used for pressure monitoring, evacuation, inputs for thermocouples, and a window for monitoring the sample.

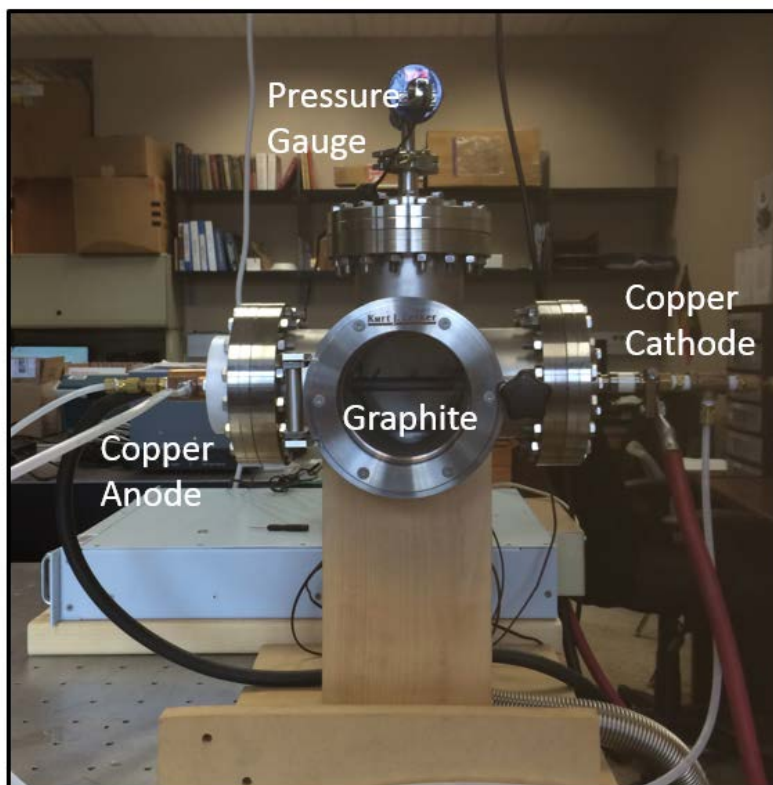


Figure 5-1 Photo of vacuum chamber assembly

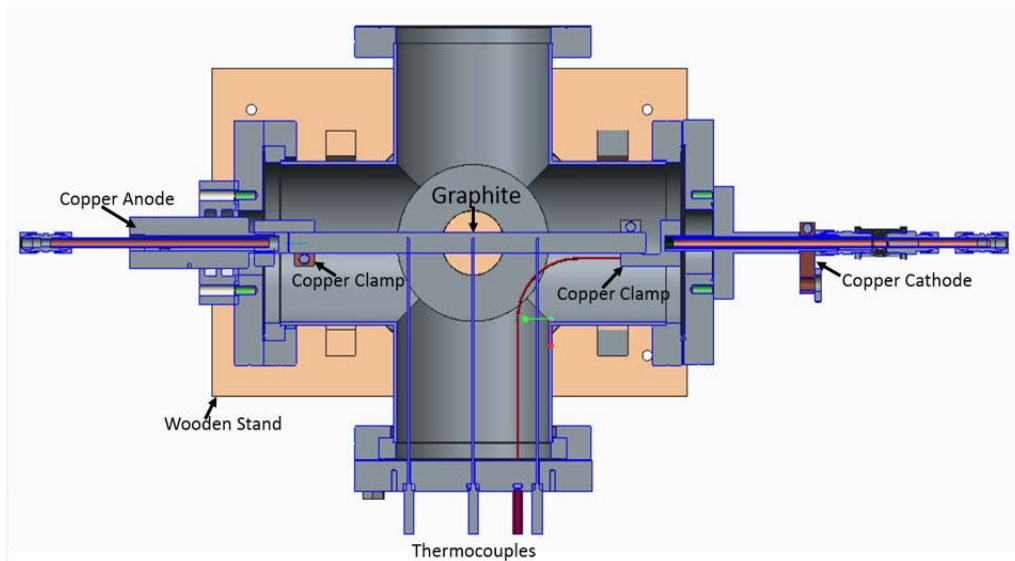


Figure 5-2 Top cross sectional view of six way

5.1.1 Electrical Control

Current was distributed from the Magna power supply to a custom copper clamp that was clamped outside of the chamber to the copper tube of a 2.75" CF Kurt. J. Lesker power feedthrough. Current traveled inside of the chamber across an 8.75" long, 0.5" diameter graphite rod that was mounted inside of the chamber. Current exited the chamber through a custom built copper power feedthrough connected to the power supply.

5.1.2 Water Cooling

Chilled water was circulated inside of both power feedthroughs as shown in Figure 5-3 .

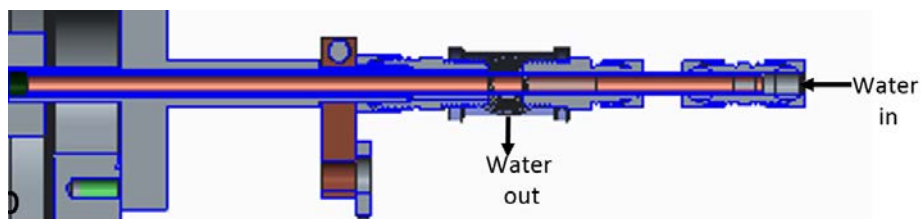


Figure 5-3 Cooling water schematic for cathode side

This was done due to the high temperatures anticipated from the Joule heating simulation of the vacuum setup. For the cathode side, a 0.1875" diameter copper tube was inserted into the 0.25" copper tube of the Kurt. J. Lesker power feedthrough. The inserted tube served as the inlet for the chilled water, while the area between the tubes served as the outlet. According to the manufacturer, the Kurt J. Lesker power feedthrough (cathode feedthrough) should not reach temperatures above 450°C.

The copper anode feedthrough was sealed with a Viton Fluoroelastomer o-ring which has a maximum temperature of 200°C. Thus, in order to maintain a vacuum environment, it was imperative to keep the temperature of the copper anode below this temperature. Similar to the cathode side, a copper tube was placed inside of the anode feedthrough serving as the inlet for the chilled water. The area outside of the tube again served as the outlet for the chilled water.

5.1.3 Temperature Measurement

Temperatures of the nine inch long graphite rod were measured with three ungrounded, type K thermocouples 1/8" in depth in the locations shown in Figure 5-4. The thermocouples protruded the vacuum chamber through a custom built polytetrafluoroethylene (PTFE) flange. Since the sheaths of the thermocouples were constructed out of stainless steel and touching the setup, it was necessary to have a material for the flange that would electrically isolate the thermocouple from the six way chamber. Also, since the sheath may conduct heat from the graphite rod, it was desirable to have a material with a high melting temperature. PTFE was suitable for both of these requirements with a high electrical resistivity and high melting temperature. The

thermocouples were sealed against the flange with #104 Viton Fluorocarbon O-rings and silicone sealant.

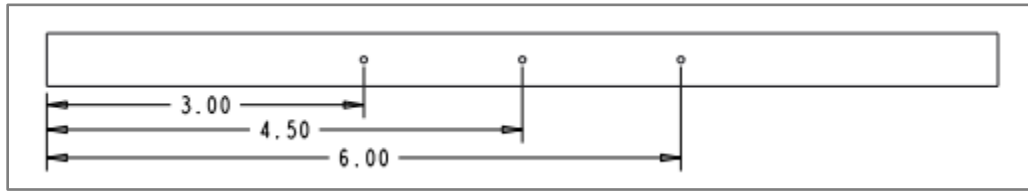


Figure 5-4 Thermocouple location for vacuum chamber graphite rod in inches.

Two additional thermocouples were attached to the copper clamp on the cathode side inside of the vacuum chamber and to the anode copper feedthrough outside of the vacuum environment. Both temperatures were monitored to ensure that no damage was done to the cathode power feedthrough and to the O-ring for the anode feedthrough. For experimental set 3, a third thermocouple was attached to the outside of the vacuum chamber to monitor the temperature of the chamber walls.

5.1.4 Vacuum Operations

Air was evacuated from the chamber at the bottom using a BOC Edwards XDS5 vacuum pump to achieve pressures between 30-50 mTorr inside of the chamber. Pressure was monitored with a Kurt. J. Lesker 275i Series Gauge that has an accuracy of $\pm 10\%$.

5.2 Experimental Procedure

- 1) Ensure the setup is electrically isolated from the vacuum chamber and setup according to the operation manual in Appendix 5.

- 2) Run the first set of experiments, atmospheric pressure and no water cooling from 0-80 amperes in steps of 20 amperes allowing time for the graphite to cool to ambient temperature between current changes. This allowed for the heat generation rate for each current to be observed to study if changes were seen from one current to the next due to the resistivity of the graphite changing.
- 3) Run the second set of experiments, atmospheric pressure with water cooling from 0-100 amperes allowing time for the graphite to cool to chilled water temperature between current changes.
- 4) Run the final set of experiments, vacuum environment with water cooling, from 0-240 amperes in steps of 20 amperes, plus at 250 amperes allowing time for the graphite to cool to chilled water temperature between current changes.
- 5) Repeat steps 2-4 for the same graphite sample.

5.3 Simulation Vacuum Chamber Joule Heating Experiment

5.3.1 Geometry and Mesh Size

The finite element analysis model was developed with ANSYS Workbench 16.0. First, an accurate geometry of the experimental setup was constructed. At the location where the material entered the chamber, the solids were split. This allowed different boundary conditions to be applied to different areas for the same solid. By observing Figure 5-5 the different volumes in which boundary conditions can be applied to are shown in different colors.



Figure 5-5 Geometry and mesh used in the vacuum Joule heating simulation

Similar to the low heat Joule heating analysis, the mesh size implemented was coarse.

This was chosen was based on time for the simulation to run, and the variance of results.

It was noted that the temperature profile and maximum temperature did not vary

significantly between a coarse and medium mesh. A coarse mesh resulted in 8300 nodes and 2400 elements.

5.3.2 Boundary Conditions

Electrical and thermal boundary conditions were applied to this model for all runs of the simulation. Similar to the low heat simulations, current was applied on one area of the geometry, and 0 volts was applied to the surface area on the opposite end of the geometry. In a vacuum environment, no heat convection was calculated for the pieces

inside of the vacuum chamber. For tests done with chilled water, the volumes that had direct contact with the water were assumed to stay at the temperature of the water, 12°C.

Radiation was accounted for in the simulation for the graphite rod and the copper clips inside of the vacuum chamber. For the simulation, it was assumed that the emissivity was constant with temperature. The ambient temperature used when calculating the radiation of the graphite and copper clamps was based upon the temperature measurements taken of the inner walls of the vacuum chamber. Radiation emitted by the

graphite and reflected back to the sample from the vacuum chamber walls was not considered.

5.4 Experimental and Simulation Results

5.4.1 Test case 1: Atmospheric Pressure and No water Cooling

During the duration of the experiments, it became apparent that the resistivity of graphite changed after being exposed to high current. This was noticed when trials one and two produced different results with the same graphite rod at the same current as shown in Figure 5-6. Initially, it was assumed that the resistance of graphite varied with temperature, but would not vary from one trial to the next. To investigate the resistivity of graphite, the voltage outputted of the power supply was recorded at the end of every current measurement. This was started a preheated graphite sample, and was repeated for a virgin graphite sample.

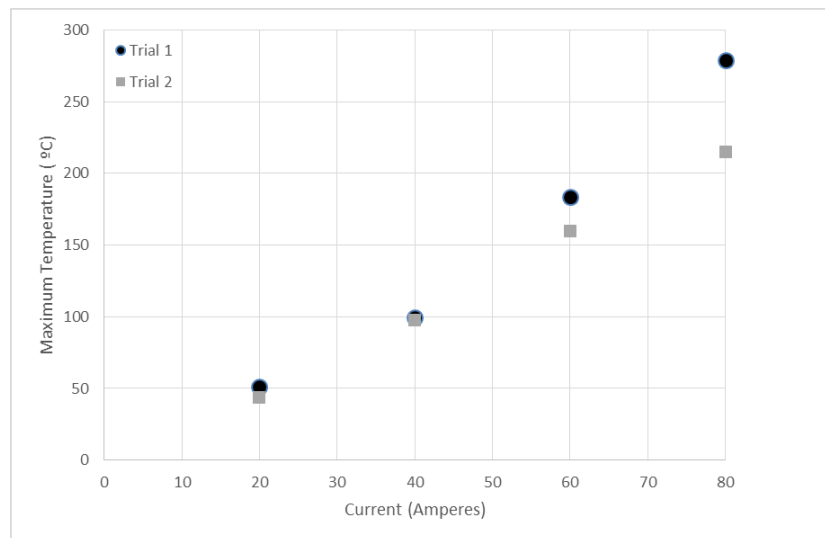


Figure 5-6 Maximum temperature measured for test case 1

As one can note by Figure 5-7, the power outputted by the power supply was much higher for the fresh rod of graphite that had not been exposed to high currents compared to a graphite rod that had been used in the previous trial and had been exposed to high currents. This resulted in higher temperatures for the fresh graphite compared to the preheated graphite rod. Thus, it was important to monitor and record the voltage during experiments to ensure that an accurate resistivity of graphite can be inputted into ANSYS simulation.

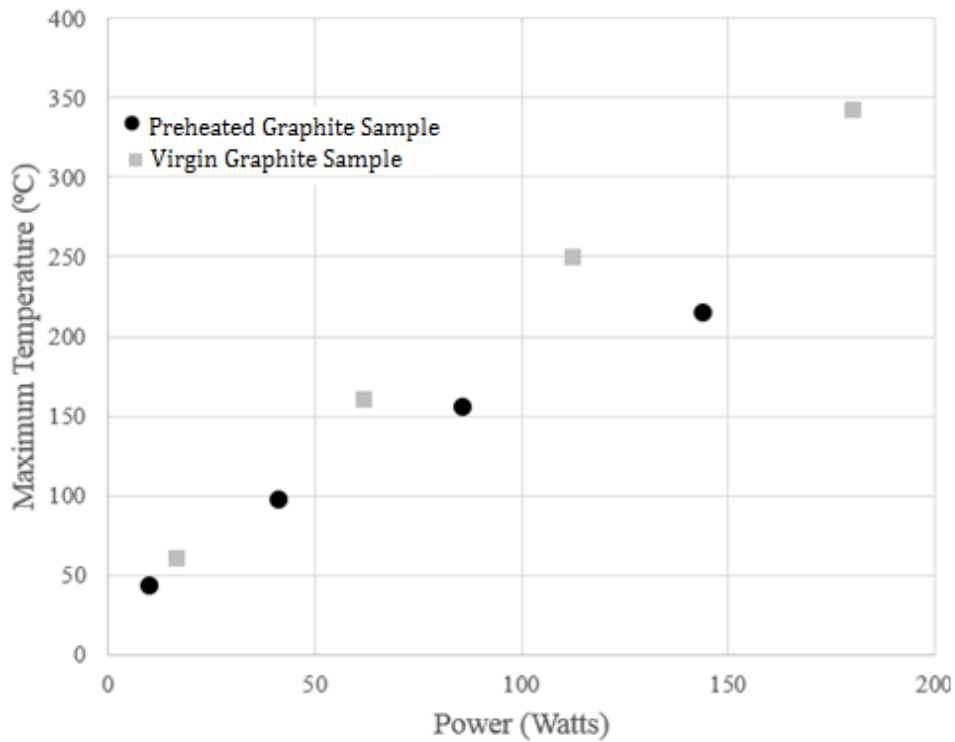


Figure 5-7 Test case 1: Maximum temperature and power comparison for samples

For the ANSYS simulation, the resistivity of graphite was based on measured voltages for a virgin rod. Furthermore, film coefficients of convection were applied in a similar manner as in section 4.3.2.

Table 5-2 displays a comparison between measured temperatures and simulated temperatures. The measured results and experimental results are within a reasonable difference of less than 10°C for all four currents. Furthermore, the percent difference calculated with equation 3-6, is below 9% for all currents. Thus, the model appears to be able to predict maximum temperature of graphite within reason for the vacuum chamber setup at atmospheric pressure, and no water cooling.

Table 5-2 Maximum temperature for measured and ANSYS for virgin graphite rod

Current (Amperes)	Maximum Temperature (°C)		Measured Thermocouple Error (°C)		Difference	
	ANSYS	Measured	Lower Bounds	Upper Bounds	(°C)	Percent
20	67.30	60	58	62	5	8
40	169.75	161	158	163	7	4
60	260.22	250	248	252	8	3
80	345.83	344	342	346	0	0
100	256.94	249	246	251	6	2

5.4.2 Test case 2: Atmospheric pressure and water cooling

Two samples were heated in test case 2. As expected, the virgin graphite reached temperatures much higher than the preheated graphite. This is due to the higher resistivity of the virgin graphite.

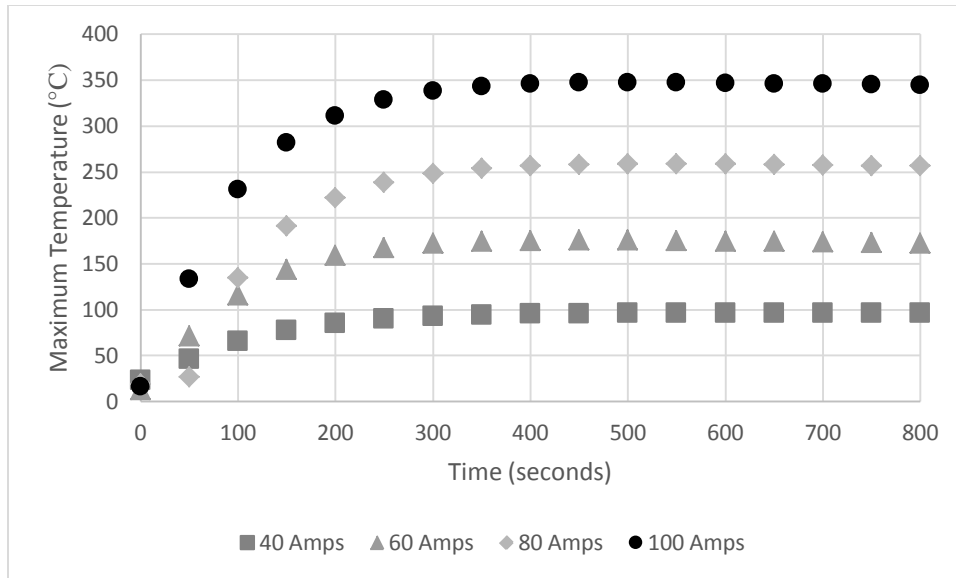


Figure 5-8 Test case 2: virgin graphite center temperature vs time graph

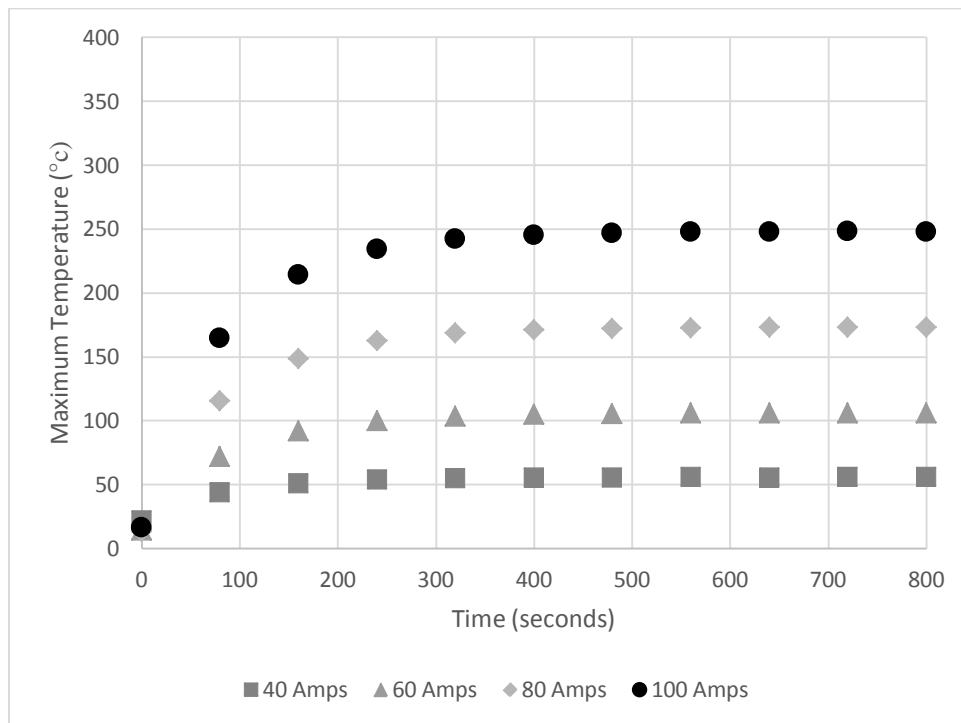


Figure 5-9 Test case 2: Preheated graphite rod temperature vs time graph

The temperature time plot is different between Figure 5-8 and Figure 5-9. For the virgin graphite sample, the graphite reached a maximum temperature and then slowly cooled.

However, the graphite's maximum center temperature reached steady state for the preheated graphite sample. This suggests that during heating of the virgin graphite, the graphite's resistivity was possibly changing so less heat was being generated towards the end of the test compared to the beginning of the test.

The experimental results for the maximum temperature show good agreement with the model for the preheated graphite as shown in table 5-3. The largest percent difference exists at 20 Amperes at 8% with a temperature difference of five degrees. The slopes from 1/3 to 1/2 agree well in Fig. 5-10 suggesting the thermal profile difference is similar. However from 1/2 to 2/3, the experimental results have a higher cooling rate. This may be attributed to a higher mass flow of the chilled water on that side of the setup. One difference between the model and the experiment is the temperature distribution of the graphite rod. The cathode side of graphite in the experiment reached lower measured temperatures than the anode side and compared to the cathode side in the simulation. This may be due to a higher mass flow rate for the cooling water. Inlet and outlet temperatures of the chilled water, as well as flow rate, were not monitored nor controlled during the experiment.

Table 5-3 Test case 2: Maximum temperature for preheated graphite measured and ANSYS values comparison

Preheated Graphite Sample						
Current (Amps)	Maximum Temperature (°C)		Measured Error (°C)		Difference	
	ANSYS	Measured	Lower Bounds	Upper Bounds	(°C)	Percent
20	67.30	60.11	57.91	62.31	4.99	8.30%
40	169.75	160.60	158.40	162.80	6.95	4.33%
60	260.22	250.10	247.90	252.30	7.92	3.17%
80	345.83	343.86	341.66	346.06	0.23	0.07%
100	256.94	248.58	246.38	250.78	6.16	2.48%

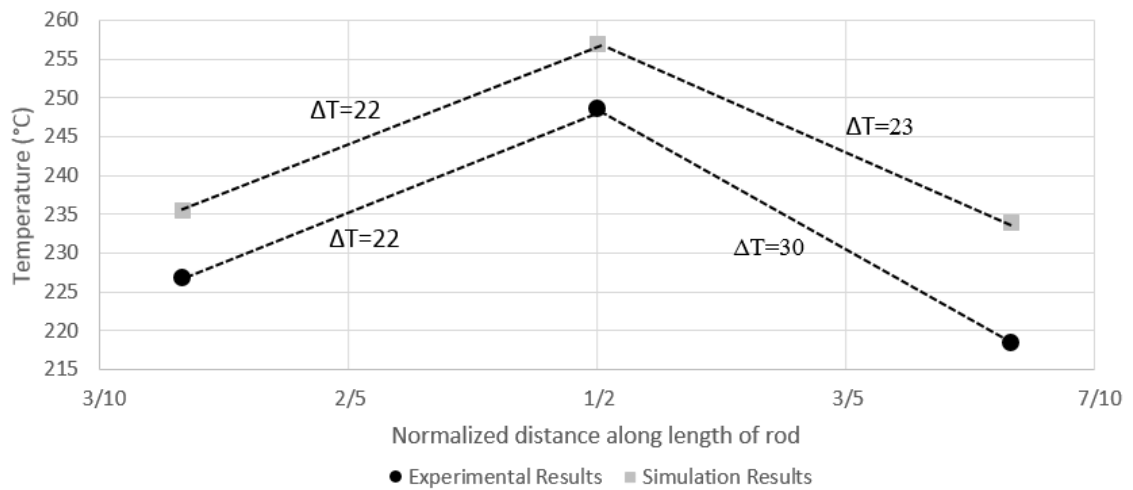


Figure 5-10 Test case 2: preheated graphite temperature profile for measured and simulation values at 100 amperes.

5.4.3 Test case 3: vacuum environment with water cooling

Test case 3 was conducted in a vacuum environment with water cooling with two samples of graphite. To study the accuracy of the ANSYS model, the preheated graphite sample was chosen since previous results has shown the resistivity to be more consistent than the virgin graphite. Also, for the preheated sample, the temperature of the vacuum chamber walls was measured. This made the ANSYS simulation for accurate for the

radiation heat transfer from the graphite sample. It is shown in Fig. 5-11 that the maximum measured temperature in the preheated graphite sample is more likely the actual maximum temperature of the graphite rod compared to maximum measured temperature of the virgin sample. This is assumed since the temperature difference between the center of the graphite and the cathode is closer in value compared to the difference between the center of graphite and the anode. For example, at 250 amperes the anode and cathode vary by 84.4°C for the virgin sample, while for the preheated sample the anode and cathode vary by 27°C. For the virgin graphite sample, it is possible the maximum temperature was not at the location measured due to the material not being homogenous, or due to a change in flow rate for the cooling water.

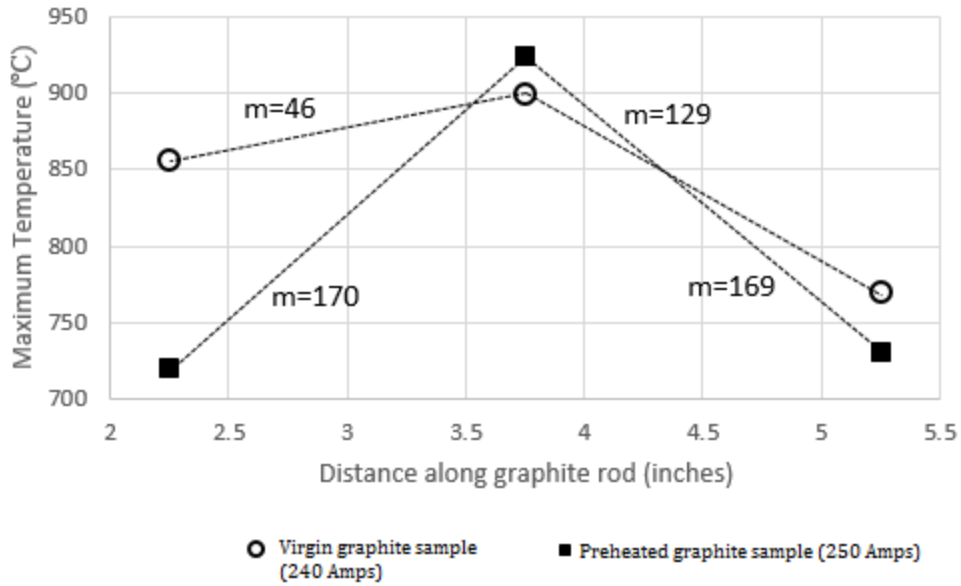


Figure 5-11 Temperature profile plot of virgin rod and preheated rod

Below in Fig. 5-12 is the temperature plot for the virgin graphite and in Fig. 5-13 is the temperature plot for the preheated sample. Two trends may be noted from these figures. First, for the virgin graphite sample there is a faster heating time at 240 amps compared

to the other currents applied. This heating time aligns to the heating times of the second trial conducted. The second trend is seen in Fig. 5-12 for the virgin graphite sample with the temperature of graphite peaking, and then decreasing. In Fig. 5-13, this trend is not seen, suggesting that the trend seen in Fig. 5-12 may be due to the resistivity of graphite changing while heating.

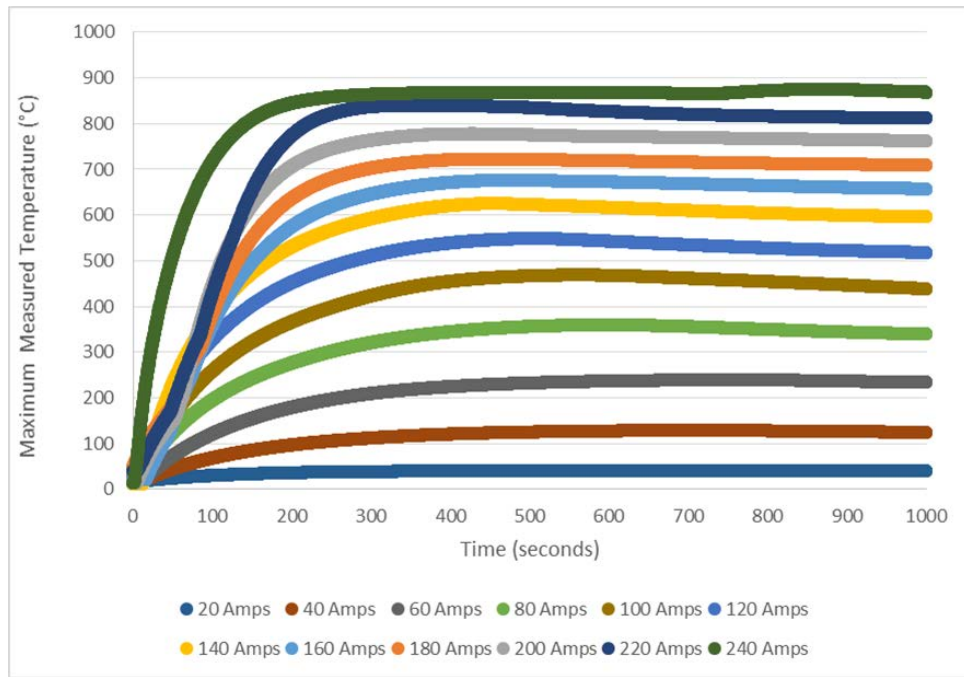


Figure 5-12 Maximum Measured Temperature Time Profile for test case 3: virgin graphite

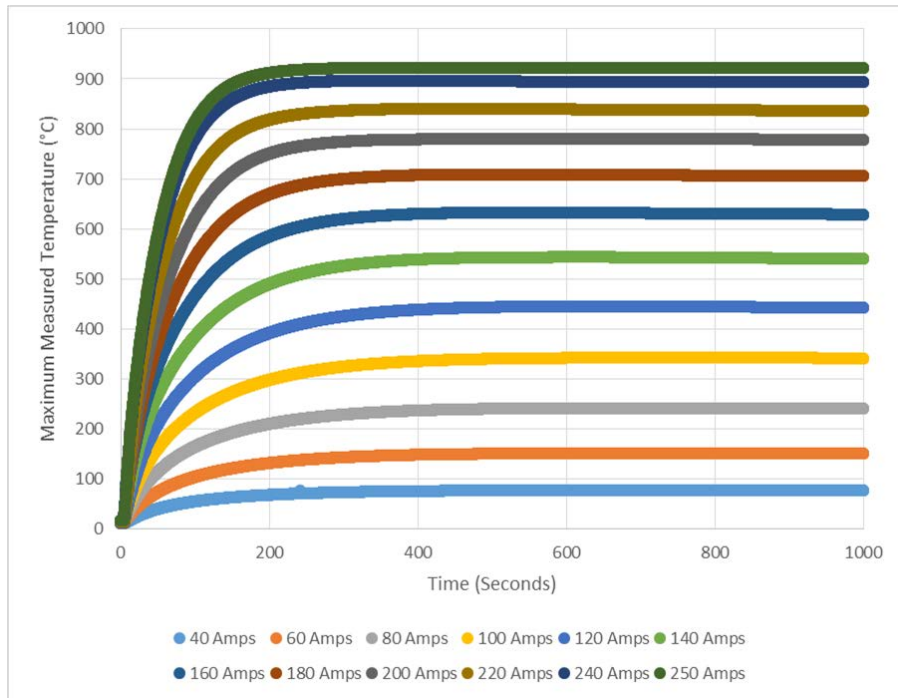


Figure 5-13 Maximum measured temperature time profile for test case 3: preheated graphite sample

Table 5-4 compares the measured results to ANSYS simulation of the preheated graphite sample by using equation 3-6. At 20-100 amperes, there was no difference between the ANSYS reported value and the measured value including error from the thermocouple based on the accuracy of the thermocouple. The largest percent error between the measured and ANSYS results was 2.63% at 160 amperes with a temperature difference of 17 °C. For predicting temperature for Joule heating up to 1000°C, this is an acceptable percent error.

Table 5-4 ANSYS simulation and experimental data comparison for test cast 3, preheated graphite sample

Current (Amperes)	Maximum Temperature (°C)		Measured Error (°C)		Difference	Percent Difference
	ANSYS	Measured	Lower Bounds	Upper Bounds		
20	29	28	26	31	1	4%
40	77	77	75	79	0	0%
60	150	151	149	153	1	1%
80	240	242	239	244	2	1%
100	343	342	340	345	0	0%
120	455	445	442	448	10	2%
140	525	543	539	548	18	3%
160	611	633	628	637	21	3%
180	691	709	704	714	18	3%
200	766	780	774	786	14	2%
220	838	840	834	847	3	0%
240	904	897	890	903	7	1%
250	936	924	917	931	12	1%

6 EXPERIMENTAL DESIGN FOR MEASURING SPECTRAL, DIRECTIONAL EMISSIVITY

6.1 Facility Overview

Experiments for measuring spectral, directional emissivity were conducted in the *Institute for Sustainable Manufacturing Brazing, Soldering, and Heat Exchanger Laboratory* at the University of Kentucky. Samples were heated to the desired temperature in a furnace manufactured by DATA PHYSICS, OCA-LHT; HTFC 1200 system capable of reach 1200°C. However, in this experiment at 1200°C a sample temperature of 875°C was measured. The heating zone has an alumina oxide tube with a ceramic mount for samples. The furnace has purging capabilities to produce an inert atmosphere to slow oxidation of the samples. For these experiments, N₂ with a purity of 99.999% was utilized as the purging gas.

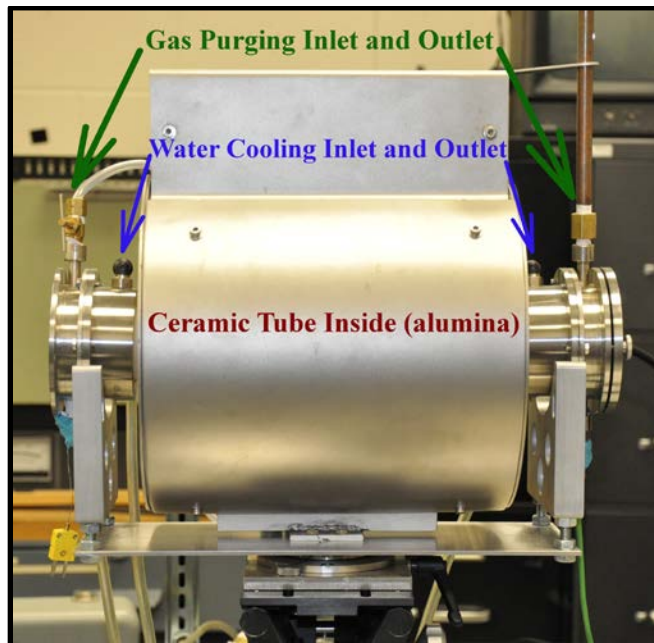


Figure 6-1 Picture of furnace used to heat samples to desired temperatures

To block the radiation of the furnace during measurements, a water cooled adapter was designed and built for the existing furnace to house a stainless steel tube that slides around the sample during measurements and acts as a radiation shield.

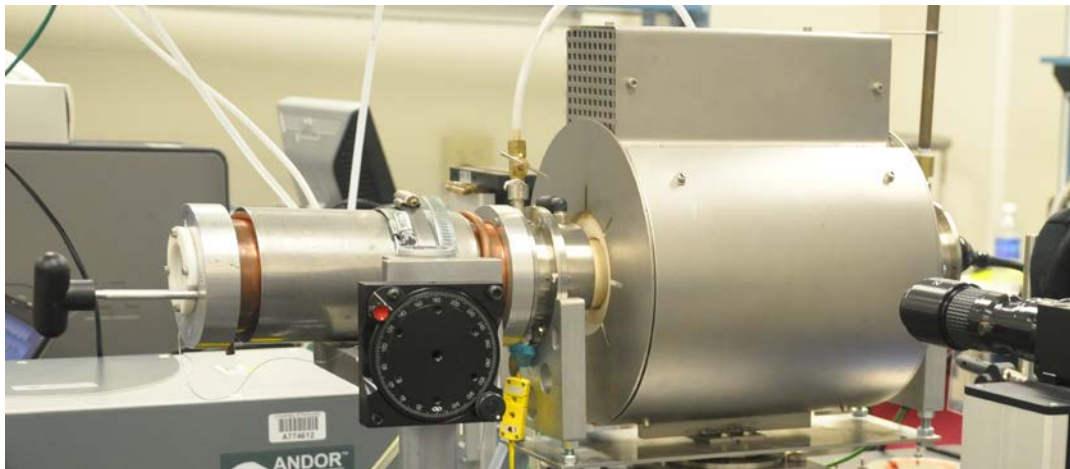


Figure 6-2 Radiation cooling adapter attached to the furnace

6.1.1 Radiation Shield Cooling Adapter

6.1.1.1 Radiation Shield Cooling Adapter Design

To block out the radiation from the furnace during sampling, a cold tube (or radiation shield) must be slid over the sample. This adapter was specifically designed to fit onto the preexisting furnace for this application. Figure 6-3 shows a hidden line view of the adapter attached to the furnace. The main housing of the adapter is a three inch diameter copper tube with a quarter inch wall thickness. Copper was chosen due to its high thermal conductivity.

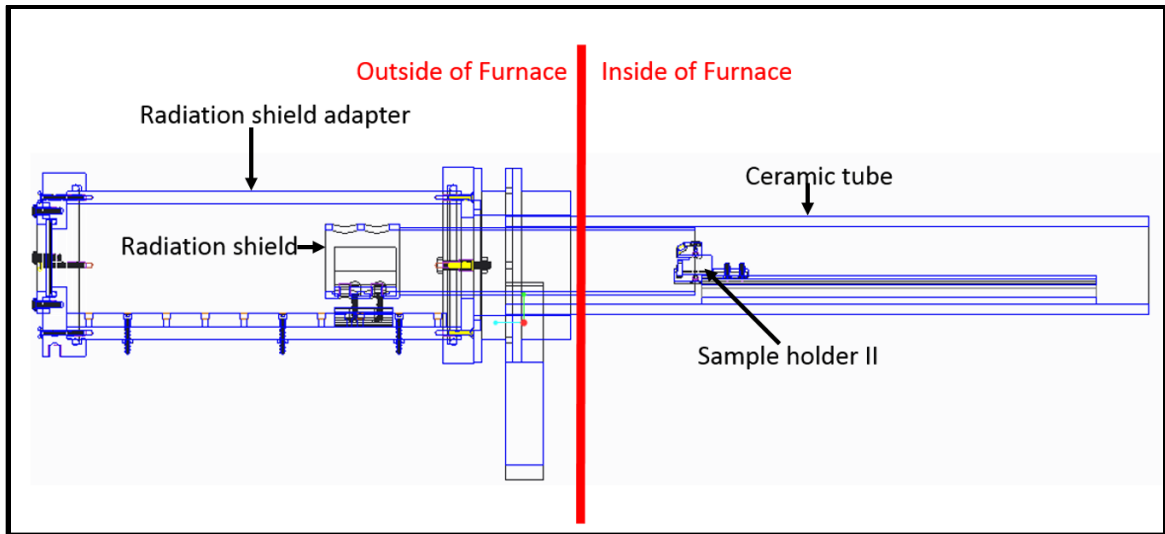


Figure 6-3 Hidden line view of radiation shield adapter and furnace

The radiation shield is a 1.50" outer diameter stainless steel tube with 1/8" wall thickness 7" long. The radiation shield is mounted on a carriage that travels along a pre-made frelon-lined guide rail that is mounted in the bottom of the tube. The carriage is moved along the rail by a rod attached to the radiation shield holder and extends outside of the chamber sealed by a Viton O-ring. Clamped to the outside of the radiation shield adapter is a 1/4" copper tube used for water cooling the adapter with potable water. The front flange that attaches to the furnace is manufactured out of aluminum. The front flange and adapter attaches to the furnace using preexisting 4 mm threaded holes in the furnace. The front and back flanges are sealed to the copper tube with sealing flat headed Philips machine screws screwed into the wall of the copper tube. The two flanges are also sealed with 3/16" Viton Fluoroelastomer O-rings to seal the radiation adapter from the atmosphere.

A mineral insulated type k thermocouple with an inconel sheath and diameter of 0.02” is epoxied with Omega Bond 600 High Temperature cement to the interior of the radiation shield tube. This cement is applicable to temperatures up to 1400°C and has a thermal conductivity of 2 W/m*K. The thermocouple is epoxied two inches from the edge of the tube that would be inserted into the furnace.

The back flange of the adapter is manufactured out of aluminum and contains a 60 mm diameter, 3 mm thick sapphire window. The sapphire window was chosen because of the high transmittance in the visible and lower infrared wavelengths, Figure 6-4. The window is pressed against a 3/16” Viton Fluroelastomer O-ring by a nylon ring to seal the adapter against the atmosphere. Different window glasses may be inserted if different wavelengths need to be investigated in the future.

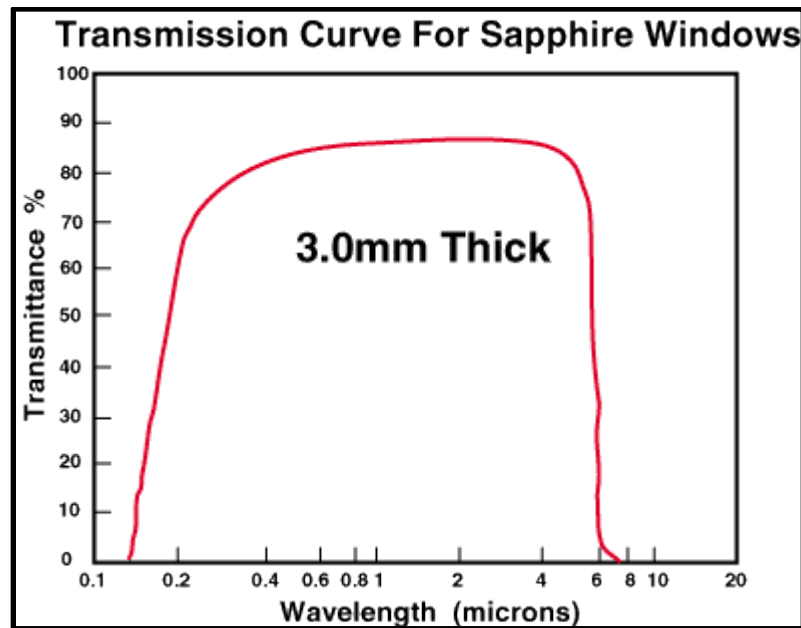


Figure 6-4 Transmission curve for sapphire window [Edmund Optics]

6.1.1.2 Verification Tests of Radiation Shield Temperature

Two tests were performed to verify that the radiation shield remained at low temperatures during operations. This is critical to ensure that the radiation shield does not reach temperatures where the radiation shield is emitting radiation.

The first test heated the furnace up to 575-580°C and then heating the furnace to 775°C at which point the tube was inserted into the furnace. It is predicted that the tube will only be in the furnace for a maximum of 120 seconds during emissivity measurements. A test time of 340 seconds was chosen to ensure that the tube does not reach high temperatures during measurements. At 575°C-580, the tube was at a temperature of 43°C inside of the radiation shield. Due to the low temperature of the shield, the furnace temperature was increased to 775°C. Figure 6-5 shows that at the location of the thermocouple, the maximum temperature recorded after 340 seconds was 146°C.

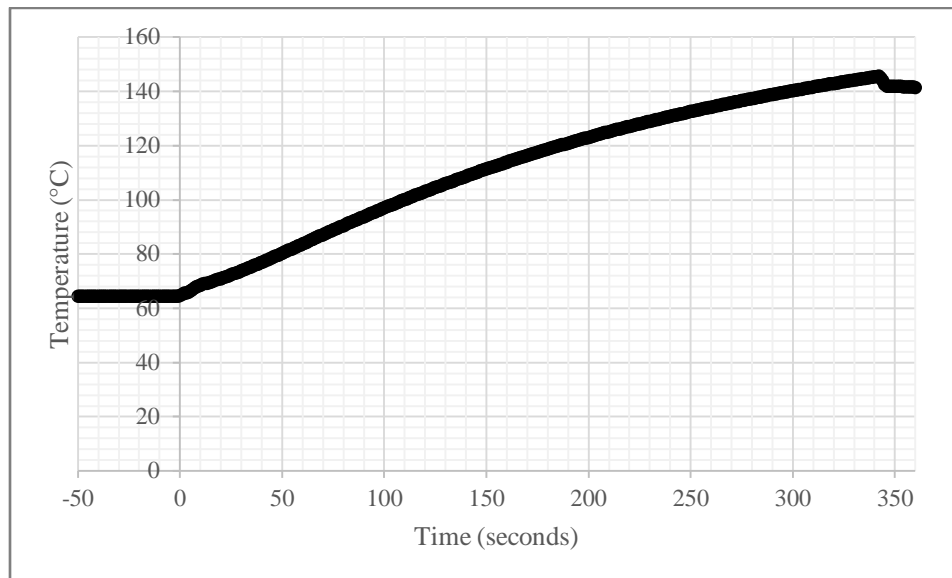


Figure 6-5 Radiation shield measured temperature at furnace temperature 775 °C

The second test involved heating the furnace up to its maximum temperature of 975°C from room temperature, and then inserting the radiation shield into the furnace for 60 seconds. This test showed that the radiation shield stays below 105°C at the thermocouple location after 60 seconds of exposure, Fig. 6-6.

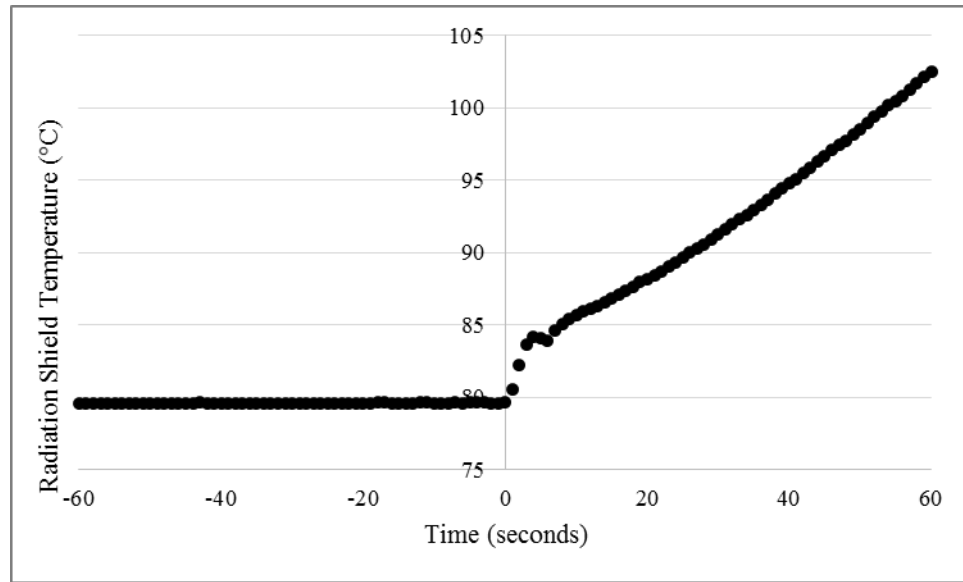


Figure 6-6 Measured temperature of shield in furnace at 970°C for 60 seconds

A thermal transient ANSYS simulation was carried out with ANSYS Workbench 16.0 to predict the temperature of the tip of the stainless steel tube for the time that the tube was inserted into the furnace for the three furnace target temperatures. The tube was divided up into four sections to apply different temperature boundary conditions along the tube. The maximum temperature applied corresponded to the furnace temperature while the minimum temperature applied corresponded to the temperature of the radiation shield before being inserted into the tube. The middle two temperatures were the two midpoints between the minimum and maximum temperature values.

Figure 6-7 plots the results for the three furnace target temperatures. At the thermocouple location, the ANSYS simulation was accurate within seven degrees or less compared to the measured value at the thermocouple location. The simulation shows that shield will remain below 180°C for all three cases. Thus, the shield will not be emitting radiation that will interfere with intensity measurements of the sample.

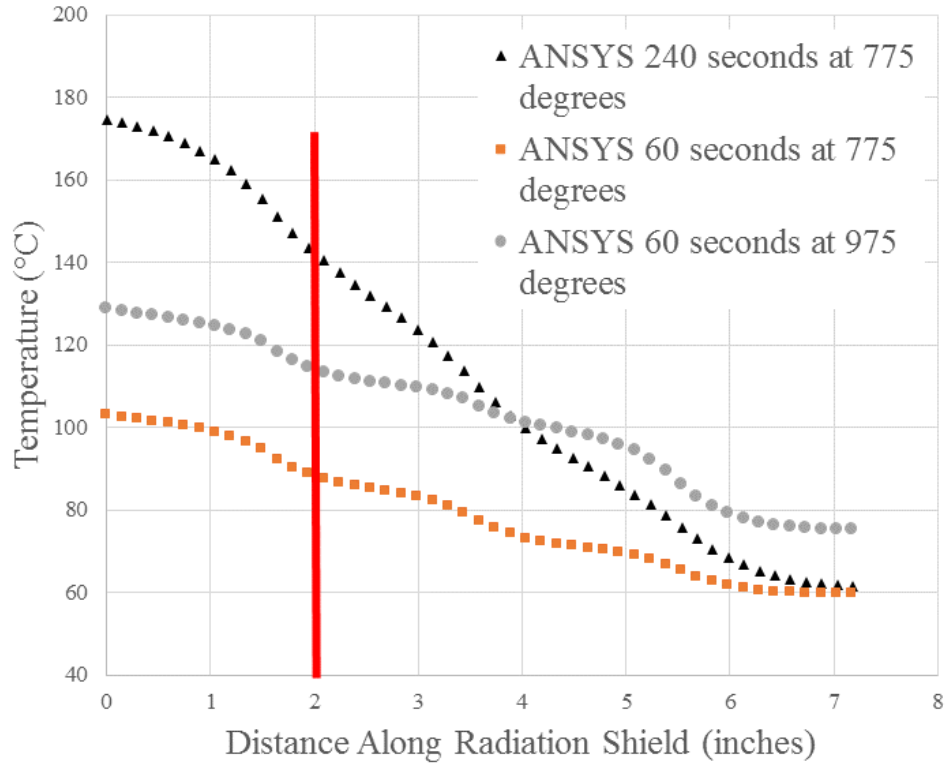


Figure 6-7 ANSYS results for temperature profile of radiation shield

6.1.2 Optical Setup

6.1.2.1 Spectrometer Setup

In order to image the samples and blackbody on the spectrometer, an optical setup was designed alongside of PhD candidate Bradley Butler as shown in Fig. 6-8 and Fig. 6-9.

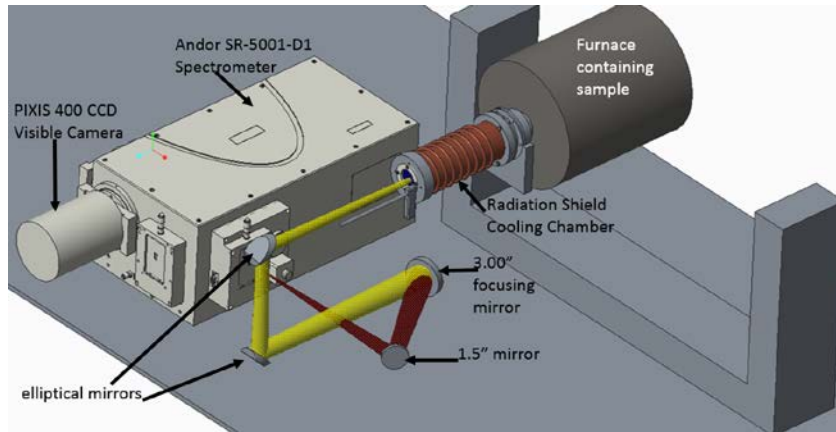


Figure 6-8 Sketch of optical setup for emissivity measurements

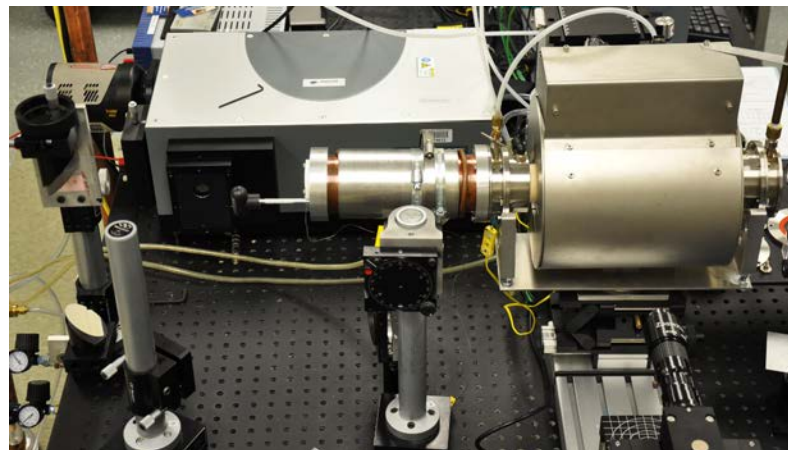


Figure 6-9 Picture of optical setup

The emission from inside the furnace is redirected to a parabolic focusing mirror with a focal length of 444 mm by two elliptical 1.875" silver flat mirrors located on the periscope above and focused onto the entrance slit of the spectrometer passing another redirecting 1.5" silver flat mirror. Through this set-up, a vertical line across the test specimen of about 16 mm length is imaged on the entrance slit of the Andor Shamrock 500i spectrometer, de-magnified by a factor of 2 allowing for different sample locations to be recorded at the same time on the Princeton PIXIS 400 CCD. The PIXIS 400 has a

1340 x 400 imaging array with 20 μ m x 20 μ m pixels. Before spectroscopy measurements are taken, it is critical to perform four tasks:

- 1) Align the optical setup by back tracing from the spectrometer to the sample location with a laser.
- 2) Align the CCD camera on the spectrometer to ensure that it is in the focal plane of the spectrometer's focusing mirror and that a vertical line on the CCD is aligned with the image of the entrance slit on the CCD.
- 3) Calibrate the CCD camera with a mercury lamp for a wavelength calibration for all center line wavelengths to be used during the measurements.
- 4) Calibrate the CCD camera with a continuum lamp of known radiance (here a Gigahertz miniaturized integrating sphere) placed at the measurement location for an intensity calibration.

Optical alignment was accomplished by back tracing a JDS uniphase 630nm 4mW laser, which enters the spectrometer through an otherwise unused second exit slit and takes the reverse optical path, to a dummy sample located in the same position as the actual sample measurement in the furnace. At each point of the optical path, the height of the laser was measured to confirm that the optics were aligned vertically. Additionally, the optics were aligned horizontally to ensure that the laser struck the middle of each mirror. The dummy sample contains three LEDs, green, white and blue, aligned vertically along the same axis as the sample, the center LED being at the position of the blackbody used in the setup. This produces an image on the entrance slit of the spectrometer and on the CCD to verify that the optics are aligned with the blackbody as shown in Figure 6-10.



Figure 6-10 Alignment diodes imaged on the entrance slit of the spectrometer

To align the CCD camera on the spectrometer, a StellarNet SL2 mercury argon calibration lamp was placed in front of the input slit of the spectrometer opened to $25\ \mu\text{m}$ which corresponds to about one pixel width of the CCD and measured with an integration time of 200 ms. Three rows of pixels (50, 200, and 350) at different locations on the CCD camera were selected and were displayed on the same plot. Since the rows are at the same wavelength, the three lines should overlap if the camera is aligned. If not, the camera must be adjusted on the spectrometer with fine screws to cause the wavelength lines to overlap. After this alignment, the three spectra were saved to use for the wavelength calibration. Next, an acrylic sheet was placed in between the spectrometer and the calibration lamp to be used as a long pass filter above $\sim 330\ \text{nm}$ and the emission was recorded. Therefore, the most prominent line of mercury at $253.652\ \text{nm}$ was absorbed by the filter.

First, the background intensity was extrapolated from a wavelength range that mercury and argon do not emit, and the background was subtracted from all three measurement

points (50, 200, 350) for measurements with and without the filter. Figure 6-11 shows the uncalibrated spectrum. The red boxes show that the peaks around pixels 200, 700, and 1250 disappear in the measurement with the long pass filter.

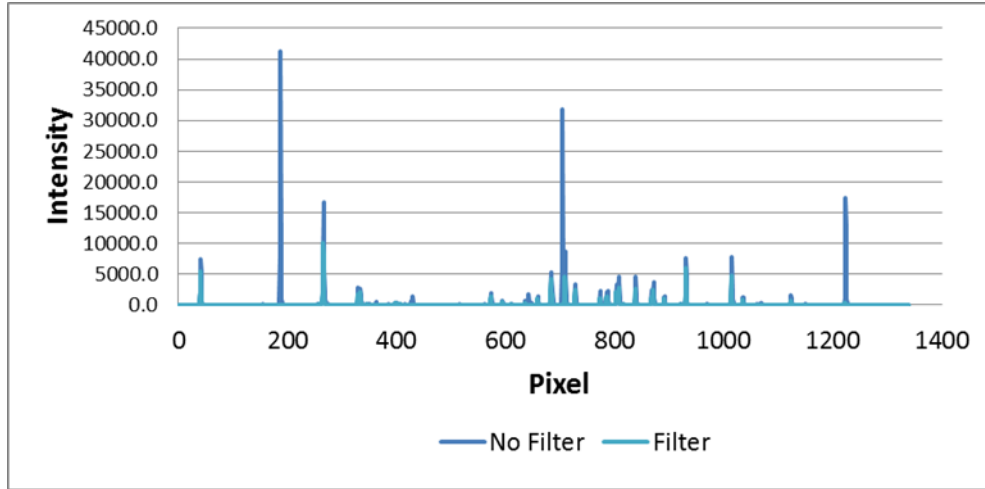


Figure 6-11 Uncalibrated wavelength reported by the CCD at one row

These strong lines are the 2nd, 3rd, and 4th order diffraction lines of the mercury line at 253.652 nm which appear at 507.3 nm, 760.95 nm, and 1014.608 nm in the measured spectrum. All wavelengths on the CCD are now interpolated with a second order polynomial function which is defined by the three pixel-wavelength pairs of the above mentioned lines. The measured data may be then compared to known data from NIST to check the wavelength calibration. Figure 6-12 shows the calibration data and NIST data.

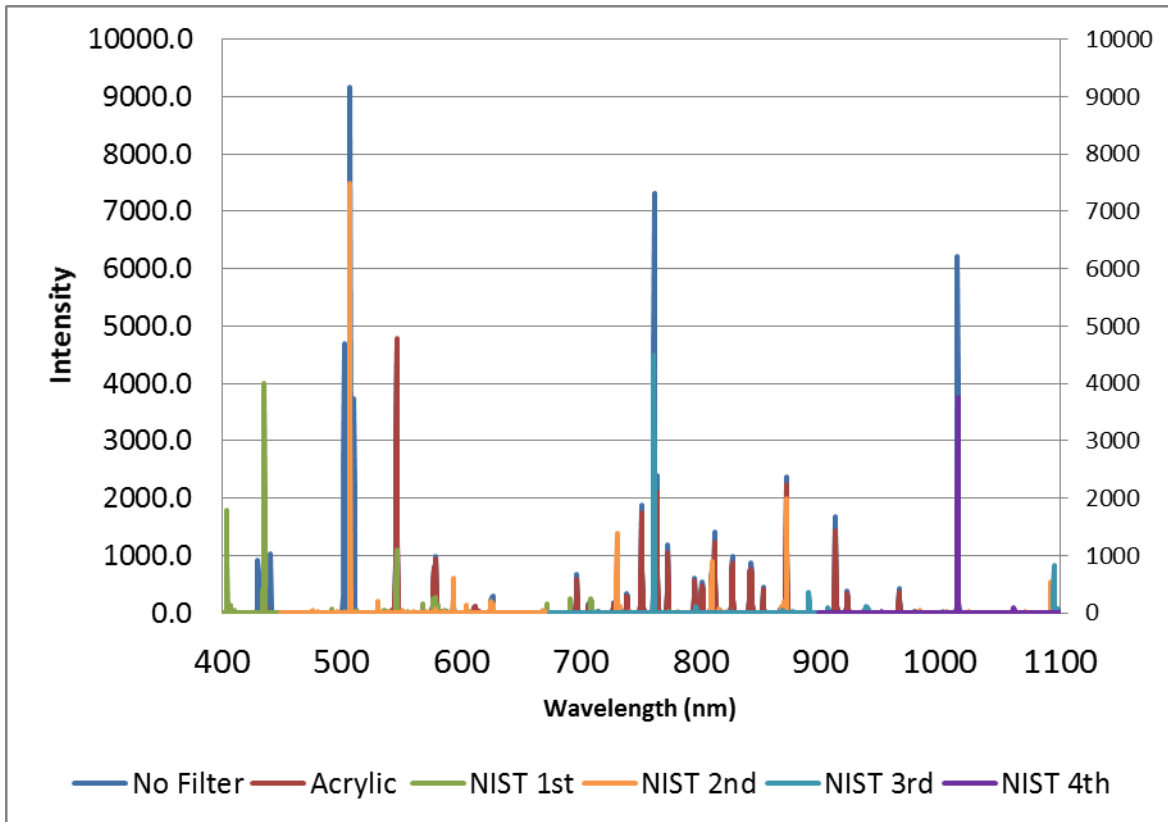


Figure 6-12 Calibrated wavelength data

For an intensity calibration, a calibration lamp with a known intensity must be placed at the same location as the sample. In this investigation, a Gigahertz-Optik ISS-5P calibration lamp is used. The intensity of the lamp is recorded by the CCD with the same entrance slit width as used during testing. The manufacturer provides a calibration curve of radiance versus wavelength for the calibration lamp. Thus, by dividing the measured calibration data from the CCD camera and spectrometer (units: counts) by the integration time of the camera, the measured data will be in counts/sec. Next, this data is related to the calibration curve given by the manufacturer to convert this data to $\text{mW}/(\text{m}^2\text{sr}\cdot\text{nm})$. Thus, a correction factor in $[\text{mW}/(\text{m}^2\text{sr}\cdot\text{nm})]/[\text{counts}/\text{s}]$ may be defined by dividing measured and manufacturer provided spectra, and data collected for a measurement at

this location and entrance slit, regardless of the integration time as long as it is recorded, may be converted to $\text{mW}/\text{m}^2\text{sr.nm}$.

The spectrometer was controlled with Andor SOLIS 32 bit and the camera was operated with WinSpec to capture the spectral measurements. During measurements the spectrometer had an entrance slit of $100\ \mu\text{m}$ and was centered at $770\ \text{nm}$. The camera operated at 2MHz analog digital conversion frequency with a variable integration time depending on the intensity emitted by the furnace. For the time of the measurement, a shutter in front of the spectrometer was opened by the CCD software. In between data acquisition, this shutter was closed.

6.1.2.2 Infrared Camera Setup

To quantify the amount of radiation emitted in the infrared regime, a FLIR SC4000 infrared camera with 420 frames per second for 320×256 focal plane array and a spectral range of $3\text{-}5\ \mu\text{m}$ was used. The camera outputted data via a gigabit Ethernet cable to a PC in counts. Counts values are proportional to the incident energy measured by each pixel of the camera as long as the camera stays within its linear range. Therefore, the integration time, here defined as the time it takes for the camera to capture a single frame of data, was adjusted to keep the count range of $3000\text{-}12000$ during all measurements. Counts below $3,000$ and above $12,000$ results in a non-linear behavior, higher counts would eventually over expose the camera. Recorded measurements were saved as a .sfmov file and converted to a .csv file for analysis by MATLAB 2014b.

6.1.2.3 Infrared Camera Adapter

For spectrally resolved measurements in the IR, the FLIR camera was intended to be coupled to the spectrometer. Thus, an adapter to connect the infrared camera to the spectrometer was designed and manufactured for the purpose of being used for these experiments. This was done by determining where the imaging plane of the infrared camera would be in relation to the focal plane of the spectrometer using Eq. 6-1. Figure 6-13 of the spectrometer displays the dimensions utilized.

$$X_{\text{CCD}} + X_{\text{IR}} = Y_{\text{CCD}} + Y_{\text{IR}} \quad (\text{Equation 6-1})$$

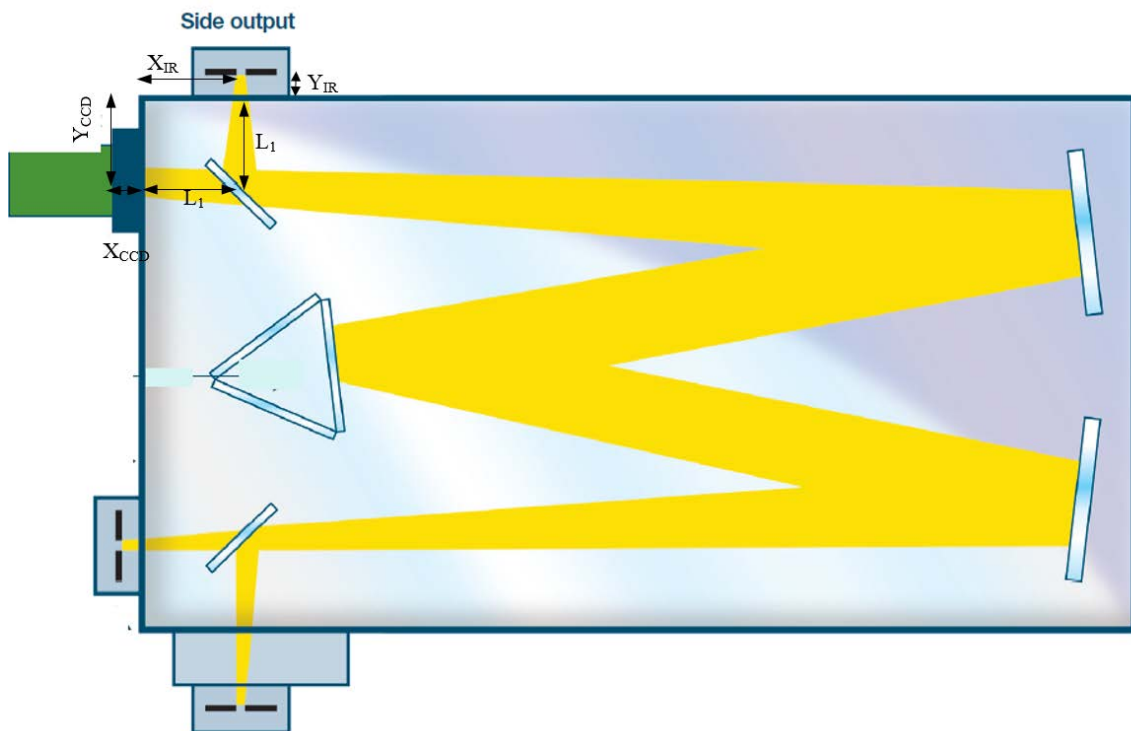


Figure 6-13 Equation 6-1 dimensions

Following these calculations, an aluminum angle was selected to hold the mounting system outside of the spectrometer. T6-6061 was chosen for its light weight and ability

to hold the camera. Afterwards, a railing system and slider was designed for the camera to mount on to allow for the camera to be adjusted. The assembly and drawings are available in appendix 1. However, for time reasons, this setup was not utilized by the publication date of this thesis.

6.2 Sample Preparation

Sample wafers were received from NASA Ames Research Laboratory pre prepped for this experiment. Each wafer contains two surfaces where one half was blasted and the other remained polished. NASA blasted each wafer with a feed pressure of 90 psi with white aluminum oxide grit supplied by Kramer Industries. Surfaces were scanned with a nanofocus μ surf explorer confocal microscope to characterize the surfaces. Table 6-1 displays the values for kr , mean peak to valley height, for the sample materials supplied by NASA.

Table 6-1 Summary of sample surfaces received from NASA Ames

Sample Material	Grit #	Mean Grit Particle Size, mm	Mean kr , μ m
Titanium 6AL-4V	800	7.3	1.77
	360	23.1	3.70
	220	46	5.85
	120	100	10.25
	60	250	19.49
Stainless Steel 304	800	7.3	2.23
	360	23.1	4.02
	220	46	5.78
	120	100	9.04
	60	250	15.08
Oxidized			

Some of the wafers were oxidized from heating to 440°C for three hours. Figure 5-14 show the titanium 6AL-4V 220 grit sample on the left and the oxidized titanium 6Al-4V 120 grit sample on the right.

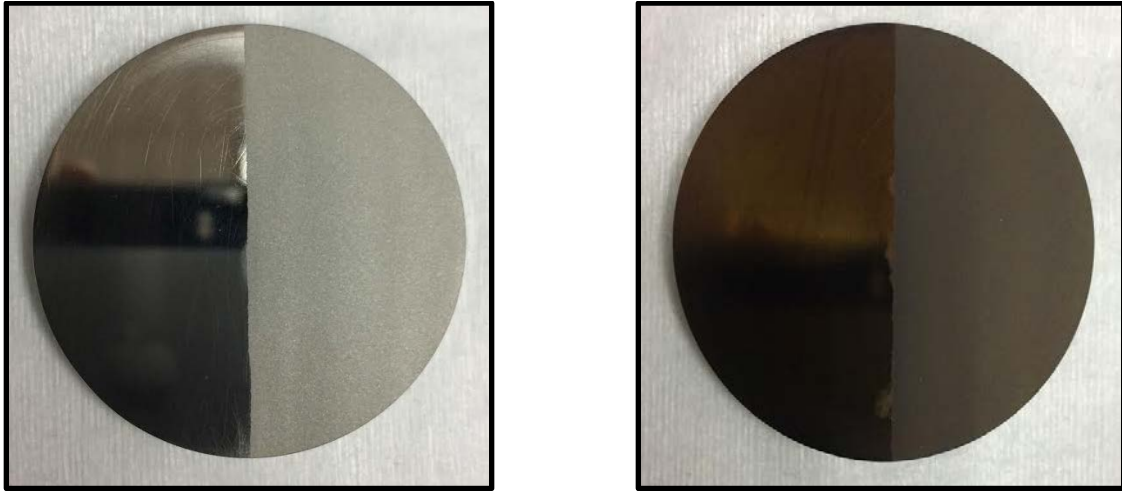


Figure 6-14 Picture of Samples received from NASA

Since the test samples are larger than the diameter of the furnace, samples used for testing had to be cut from the wafers received from NASA. To eliminate the need for additional testing, the wafers were cut in a way to allow both surfaces to exist on one sample. Furthermore, the sample size was kept small to maximize the number of samples that may be extracted from a size wafer. A smaller sample size also decreases the temperature distribution across the sample. Additionally, a small sample would be more isothermal than a larger sample. Figure 6-15 shows how the samples were cut for sample holder design 1 from the wafers using an electronic discharging machine.

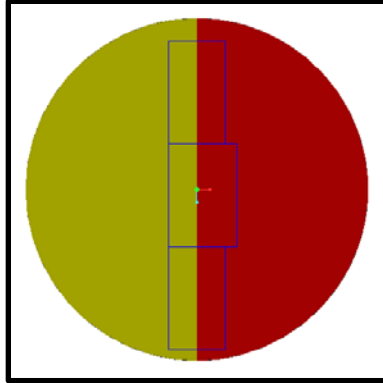


Figure 6-15 Three samples cut from a wafer

6.2.1 Sample Holder Design I

A sample holder and positioning system to mount the samples in the furnace was designed for these experiments as shown in Figure 6-16.

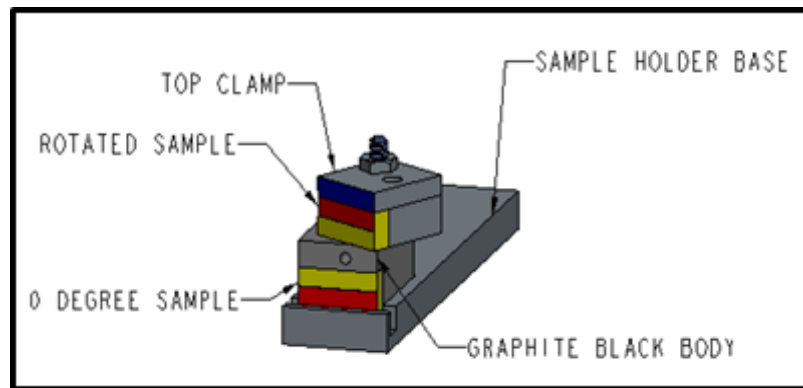


Figure 6-16 Sample holder design I

The sample holder allows two samples to be observed in the same test from two different direction. The red and yellow areas on the samples indicate the two different surface finishes on the wafer. The top sample may be rotated to either 30° or 60° . The top sample is clamped by the top piece manufactured out of stainless steel and a #3-48 flat head screw. The bottom sample stays at 0° . The sample holder also has a built in blackbody cavity manufactured out of high density graphite with a diameter of 0.0625"

and a length of 0.25, leading to a length to radius ratio of 8.3. Since graphite has an emissivity of about 0.9, this gives an apparent emissivity of the cavity greater than 0.996 compared to Figure 2-2. The sample holder base was manufactured with ¼” thick stainless steel. This allows the sample to be cantilevered off a ceramic platform in the furnace so the radiation shield was slide over it.

6.2.2 Sample Holder Design II

Due to the results from the isothermal test (Section 5.3.1), and difficulty with duplicating the same position of the sample in furnace from one test to the next, sample holder I was redesigned. Sample holder design II, Figure 6-17, involves replacing the top clamp with two holders designed specifically for 30° and 60°

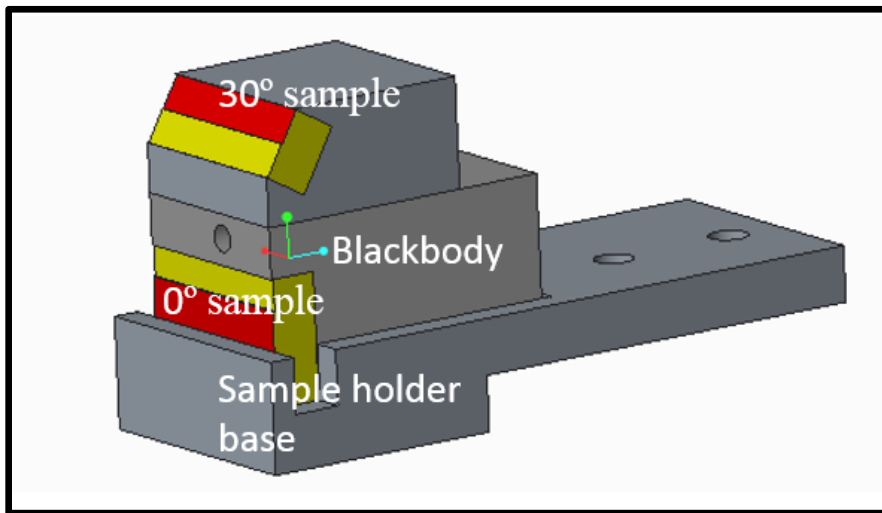


Figure 6-17 Sample holder design II

This eliminates the reflected radiation from the graphite sample onto the front of the tilted sample. Since the samples in design II are being tilted along a different axis than design I, the projected area of the samples for the 30° and 60° sample onto the camera is

different than the 0° sample. Therefore, the sample size for the 30° and 60° were increased to give the samples the same projected area as the 0° sample.

The sample holder base was redesigned to make sample placement easier in the furnace by having a lip to rest against the front of the ceramic base in the oven. Two screws were added to the sample holder as well to screw the sample holder base onto a 1/16" thick piece of sheet metal that matches the dimensions of the ceramic platform in the furnace. Thus, by aligning the corners of the sheet metal to the ceramic platform, the sample position may be duplicated from one test to the next.

6.3 Isothermal Test

In order to ensure that the samples and blackbody were at a uniform temperature, sample holder I with dummy samples manufactured out of stainless steel 304 were placed in an inert environment in the furnace. From 450°C - 1050°C in steps of 100°C , the counts measured by the infrared camera were recorded for the sample holder with the radiation shield covering the samples. A 50mm lens was attached to the IR camera to allow for a sharp image of the sample setup. Additionally, a $3.8\mu\text{m}$ filter with a width of 50nm was attached to the lens of the IR camera. For this experiment, sample temperature was initially assumed to be equal to the temperature measured by a thermocouple in the furnace. After further testing beyond this IR test, it was determined that this thermocouple measurement did not accurately reflect the temperature of the sample. Thus, 100°C was subtracted from the furnace measured temperature for analysis.

6.3.1 Experimental Procedure

- 1) Set the top sample at 30°, place the second sample in the 0° position, and place the sample holder in the furnace on the ceramic holder.
- 2) Purge the furnace of oxygen with a 99.99% pure nitrogen for one hour.
- 3) Set the target temperature to 1150°C.
- 4) Adjust the integration time to allow the counts viewed to be within the 3000-12000 range.
- 5) Slide the radiation shield over the sample when 450°C is reached and record a measurement with the IR camera software.
- 6) Retract the radiation shield once the data has been recorded from step 6.
- 7) Record a background measurement by placing a dark surface in front of IR camera
- 8) Repeat for 550°C, 650°C, 750°C, and 850°C up to the maximum temperature reached by the furnace.
- 9) Turn the furnace off and allow the furnace to cool down to 300°C before turning the purging gas off.

6.3.2 Experimental Results and Analysis

The count data recorded for all seven temperatures were analyzed for the graphite body, 0° sample and the tilted 30° sample. Figure 6-18 shows a surface plot of the counts recorded by the IR camera for this experiment.

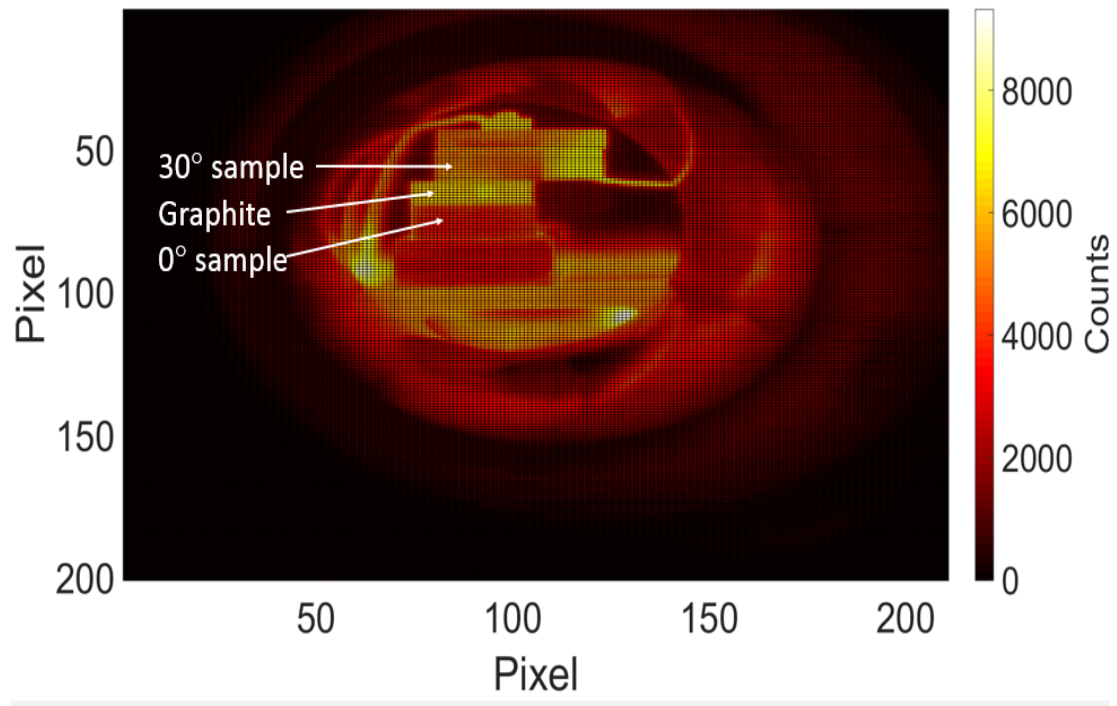


Figure 6-18 Isothermal test: furnace image

Figure 6-19 displays the temperature variation across the samples in the furnace defined by:

$$\pm T_v = \frac{T_r - T}{T} \quad (\text{Equation 6-2})$$

where T is the sample temperature, T_v is the temperature variation, and T_r is an estimated temperature in:

$$\frac{\frac{2\pi hc^2}{hc} \left[\frac{1}{\lambda^5 [e^{k\lambda T_r} - 1]} \right]}{\frac{2\pi hc^2}{hv} \left[\frac{1}{\lambda^5 [e^{k\lambda T} - 1]} \right]} = \frac{\overline{\text{counts}} - 2\text{standard deviations}}{\overline{\text{counts}}} \quad (\text{Equation 6-3})$$

The average count value, \overline{counts} , and the standard deviation for counts across a sample body were calculated to determine this estimated temperature using Eq.6-2. A ratio of Planck's law was setup as shown on the left side of eq. 6-2 to determine the percent of counts covered by the lower 95% confidence interval. The temperature represented in the numerator of equation 6-2, T_r , is a temperature value that will make the equation true. For the graphite, there is less than a 2% variation across the sample, and a 2-3% variation across the sample for the 0° sample. However, for the 30° sample, there is a 4-8% variation in temperature across the sample.

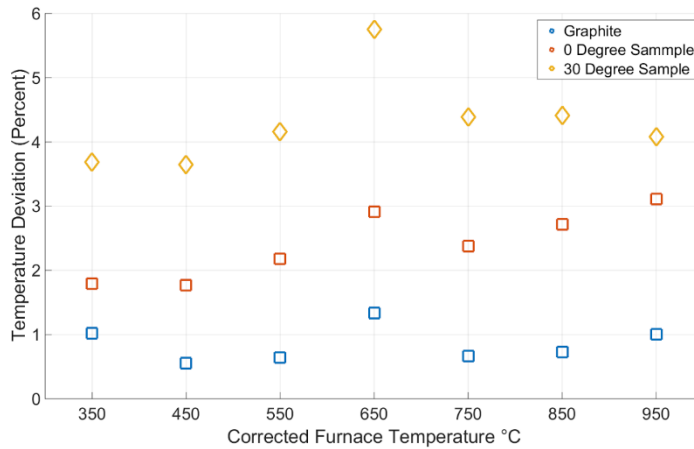


Figure 6-19 Temperature variation across the samples

Figure 6-20 displays the graphite portion of our sample with the blackbody. The blackbody was approximated to be 2x2 pixels on the camera, with spatial resolution affecting the surrounding pixels. Therefore the pixels surrounding the blackbody, the sixteen highest count values, were omitted when the emissivity and error uncertainty for the emissivity of graphite was calculated.

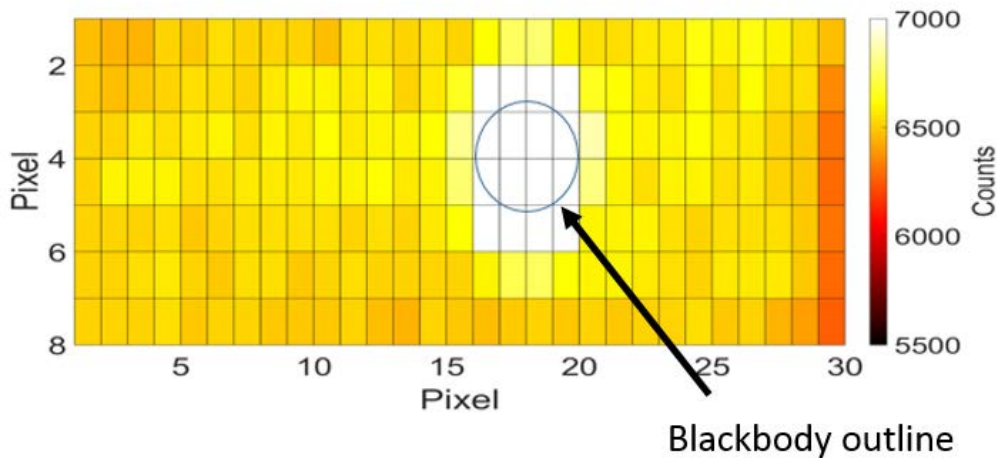


Figure 6-20 Graphite sample with blackbody outline

Figure 6-21 displays the count profile for the 30° sample. The left portion (first 13 columns) of the sample appears to have a higher count than the right portion (last 13 columns). The average count for the left portion is 5272 counts and the average count for the right half is 4872 counts. This would suggest that the left half is at a higher temperature or reflecting radiation. The left portion of the sample is sitting on top of the graphite surface while the right portion is sticking off the graphite sample. It is likely that the left portion may have been receiving radiation being emitted from the graphite that the right portion was not receiving as illustrated in Figure 6-22.

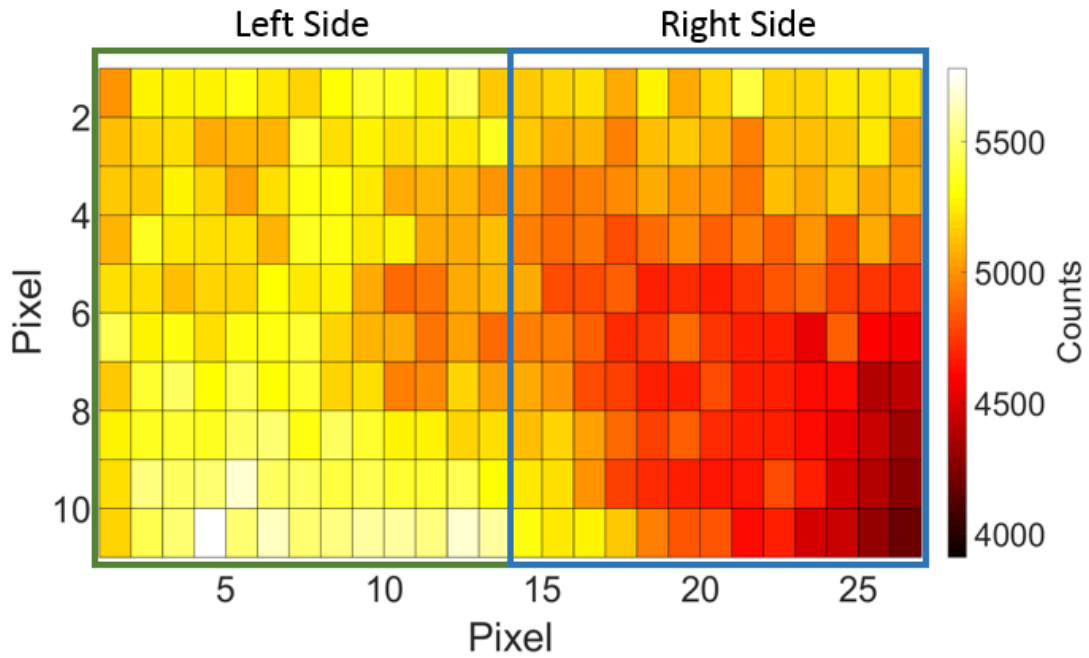


Figure 6-21 Isothermal test of 30° sample

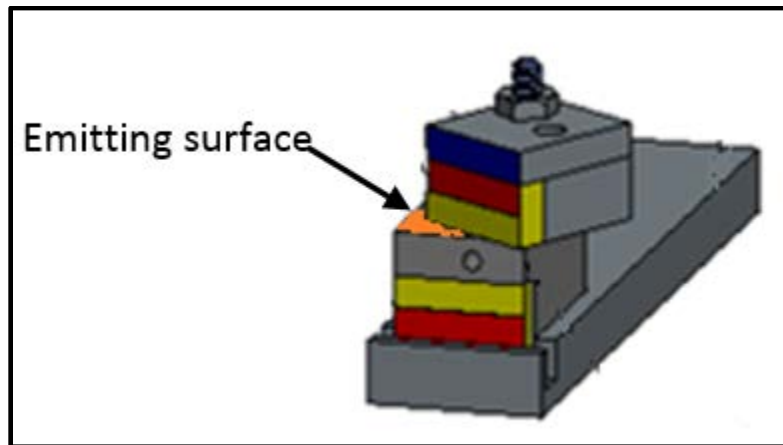


Figure 6-22 Emitting surface on sample holder design 1

The average of counts for with the shield covering the sample, \overline{WS} , and the average counts of the background noise, \overline{BG} , were used to give the corrected average counts for the shield, $\overline{[counts_s]}$, for determining emissivity.

$$[\overline{counts_s}] = [\overline{WS}] - [\overline{BG}] \quad (\text{Equation 6-4})$$

Eq 6-4 must also be done for the blackbody, $\overline{counts_b}$. To determine the emissivity of a surface, ϵ_s , including the uncertainty, such that

$$\epsilon_s = \frac{[\overline{Counts_s}]}{[\overline{Counts_b}]} \pm SE_\epsilon \quad (\text{Equation 6-5})$$

where SEs is the uncertainty of the surface that emissivity is being calculated. This standard error is defined such that

$$SE_\epsilon = \sqrt{[SE_b \frac{\delta\epsilon}{\delta b}]^2 + [SE_s * \frac{\delta\epsilon}{\delta s}]^2} \quad (\text{Equation 6-6})$$

where $\frac{\delta\epsilon}{\delta b} = \frac{-\overline{counts_s}}{\overline{counts_b}^2}$ and $\frac{\delta\epsilon}{\delta s} = \frac{1}{\overline{counts_b}}$. The standard error of the blackbody is defined

such that

$$SE_B = 1.96 \times \frac{\sigma_b}{\sqrt{N_b}} \quad (\text{Equation 6-7})$$

where σ is the standard deviation for the counts and N is the total number of counts for the surface. Likewise, the standard error of the surface is defined in a similar manner.

$$SE_S = 1.96 \times \frac{\sigma_s}{\sqrt{N_s}} \quad (\text{Equation 6-8})$$

For all three surfaces the uncertainty in the emissivity calculations is within $\pm.01$. Figure 6-23 displays the emissivity of all three surfaces versus temperature assuming the samples are at the same temperature as the blackbody.

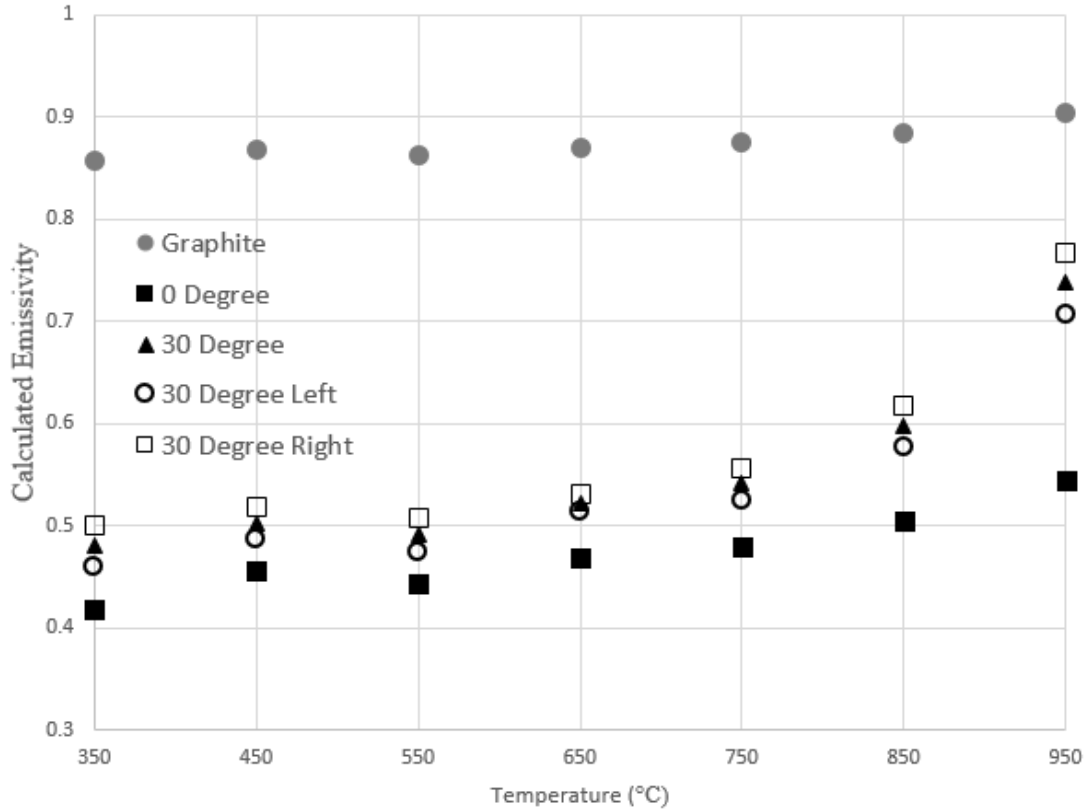


Figure 6-23 Isothermal test: emissivity results

The emissivity of graphite increases slightly from 350°C to 950°C. At 4 μm , literature reports graphite having an emissivity of 0.85 at temperatures of 1200°C. This is .04 lower than values measured at 850°C, but this may be possibly explained by the nature of the two materials since the surface roughness and density of the graphite used in this experiment may be different. This may also be explained by the inaccuracy of temperature measurement during this first test since the pyrometer was not utilized. At lower wavelengths of 0.65 μm and temperatures up to 1000°C, graphite has been reported to have an emissivity of 0.8 to 0.95 [non metal Dewitt].

The normal spectral emissivity of stainless steel 304 at 4 μm has been reported to be have emissivity values from 0.32 at 600°C and low levels of oxidation. At 1000°C and high levels of oxidation, stainless steel 304 at 4 μm has been reported to have an emissivity of 0.70. After testing, it was apparent that oxidation did occur on the surface of the sample, but this value was not quantified. The experimental emissivity value for stainless steel 304 is 0.45 to 0.55 which is within the reported range from 650-950°C.

The emissivity of the 30° sample is not accurate. This is due to either the sample not being isothermal or the sample reflecting radiation from the graphite surface. This results in a higher calculated emissivity for the right side compared to the left side by 0.05 to 0.07.

6.4 Spectrally Resolved Measurements in the VIS/NIR Wavelength Range

The Andor Shamrock 500i Spectrometer and Praxis 400 CCD camera were utilized for this experiment. Temperature measurement was accomplished with a Mikron M90 infrared pyrometer calibrated 600-3000°C placed at the backside of the furnace 1 meter from the test specimen and targeted at the graphite sample. Below 600°C, temperature measurement was based on the furnace temperature minus 100°C. This adjustment of 100°C is only approximate and has been derived from the difference between pyrometer readings and furnace thermocouple temperatures at higher temperatures.

6.4.1 Experimental Procedure

- 1) Place the sample holder in the furnace on the ceramic mount ensuring that the sample holder lip is touching the front of the ceramic mount.

- 2) Purge the furnace for one hour with 99.999% N₂.
- 3) During purging, align the pyrometer from the back of the furnace with the graphite at a distance of 1 m from the sample and an emissivity of 0.9.
- 4) After purging, set a target temperature of 1150°C on the furnace.
- 5) During heating, double check alignment of the blackbody on the CCD camera.
 - a) Set the center line on the spectrometer to 25 nm (pure imaging mode, no diffraction) and open the entrance slit to 2 mm.
 - b) Check the blackbody to see if it's centered in the center of the CCD at 670 x 200 pixels.
 - c) If not, adjust the top mirror on the periscope to align.
 - d) After alignment, set entrance slit to 100 μm and the center wavelength of the spectrometer to 770 nm.
- 6) Be mindful of the intensity limit of 65,000 by adjusting the integration time on the camera.
- 7) Insert the shield when furnace temperature reads 350°C.
- 8) Take measurement after the second reading by the CCD camera at that time. Note temperature of furnace during beginning and end of measurement.
- 9) Remove the shield and take a background measurement by covering the window to the radiation shield adapter with a black plate at the same integration time.
- 10) Repeat steps 8-9 for a furnace temperature of 450°C.
- 11) Insert shield when pyrometer reads 650°C.
- 12) Take measurement after the second reading by the CCD camera at that time. Note temperature of the pyrometer during beginning and end of measurement.

- 13) Take background measurement described in step 9.
- 14) Repeat steps 11-13 in steps of 100°C as well as for the maximum temperature reached for the graphite sample.
- 15) Turn furnace off and take similar measurements during cool down.
- 16) Turn the purging gas off at 300°C.

6.4.2 Experimental Results

So far, only preliminary results were obtained for the spectral emissivity measurements in the VIS/NIR wavelength range. However, once current inconsistencies in the intensity calibration are resolved, measurements covering a more comprehensive test matrix in terms of different materials angles and roughness values are intended to be performed. To demonstrate the procedure, results are presented from spectroscopy measurements of stainless steel 304 at 1120K (847°C) with two surfaces (1) a mean roughness height of 15 μ m and (2) an oxidized surface. This test was conducted with samples at 0° and 30° in the sample holder design II. It should be noted that the oxidized surface on the 30° sample is about 20% the size of the rough surface due to uneven blasting on the wafer received from NASA.

The non-blue areas in Figure 6-24 correspond to the surfaces that were average and analyzed in this discussion. The pixels on the left in Figure 6-24 correspond to the pixels on the CCD camera.

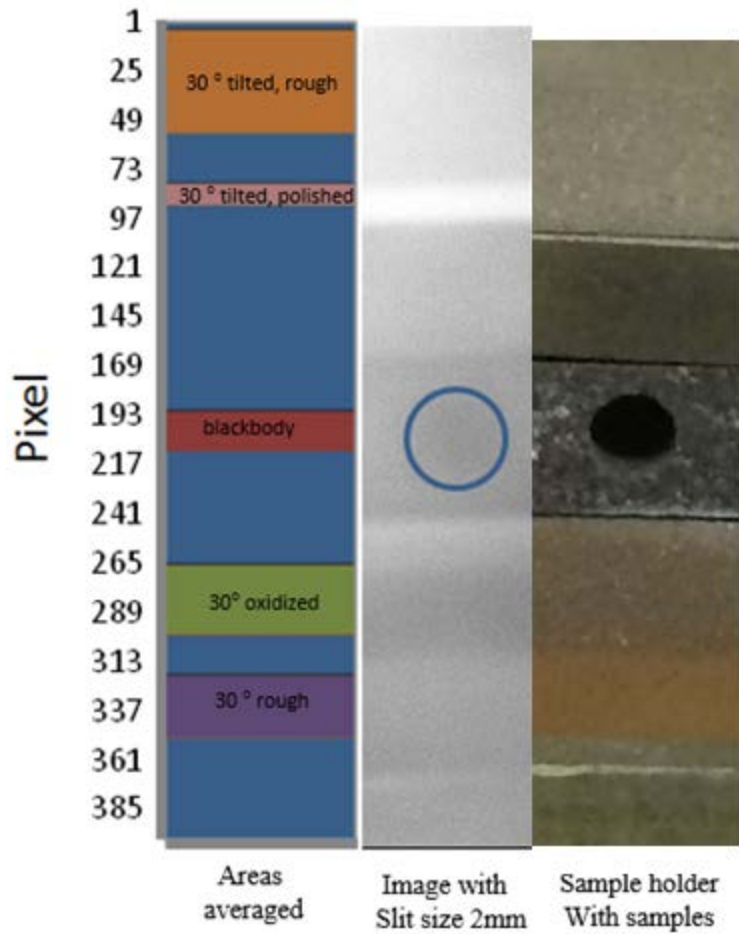


Figure 6-24 Areas investigated for spectroscopy measurements

6.4.2.1 Blackbody Analysis

The first area of interest in the measurements is the blackbody since these measurements are the reference for the emissivity for every surface. Figure 6-25 displays the blackbody curve compared to Planck radiation at 1020K, 1070K, 1120K, and 1170K and displays a comparison to blackbody curves normalized by W/m^2srnm at 700 nm. The spectral shape of the measurement indicates a temperature between 1120 K and 1170 K. The measured intensity begins to drop after 900 nm, though, then rises slightly, and then drops significantly after 1020 nm.

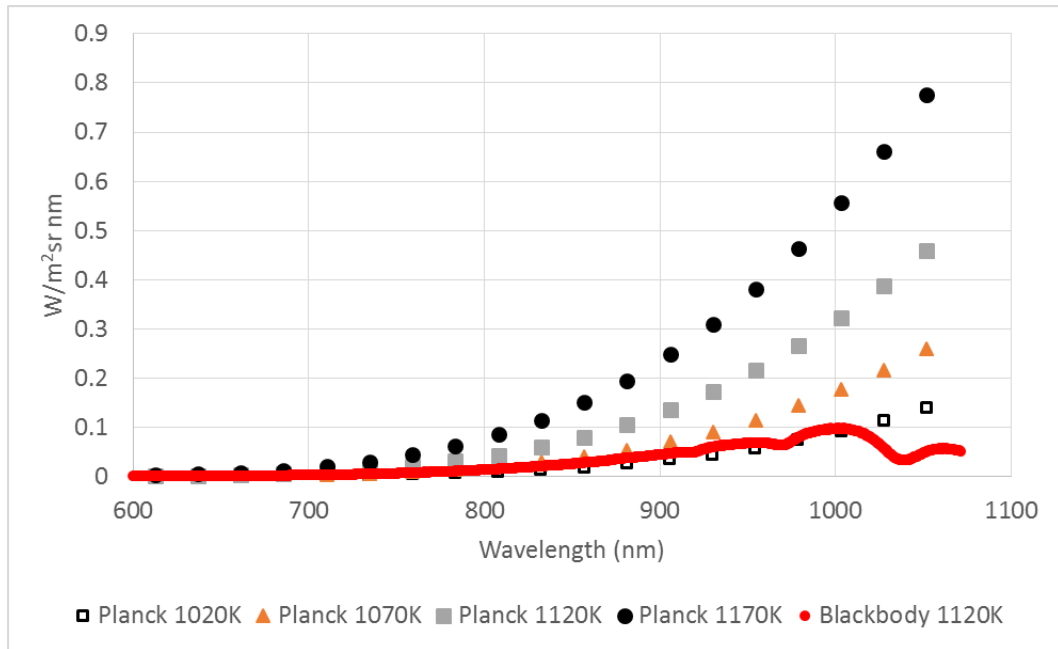


Figure 6-25 Measured blackbody curve vs Planck's curve

The measured blackbody should not have these increases and decreases, but rather follow Planck's curve. This error may be due to the manner in which the intensity calibration was performed.

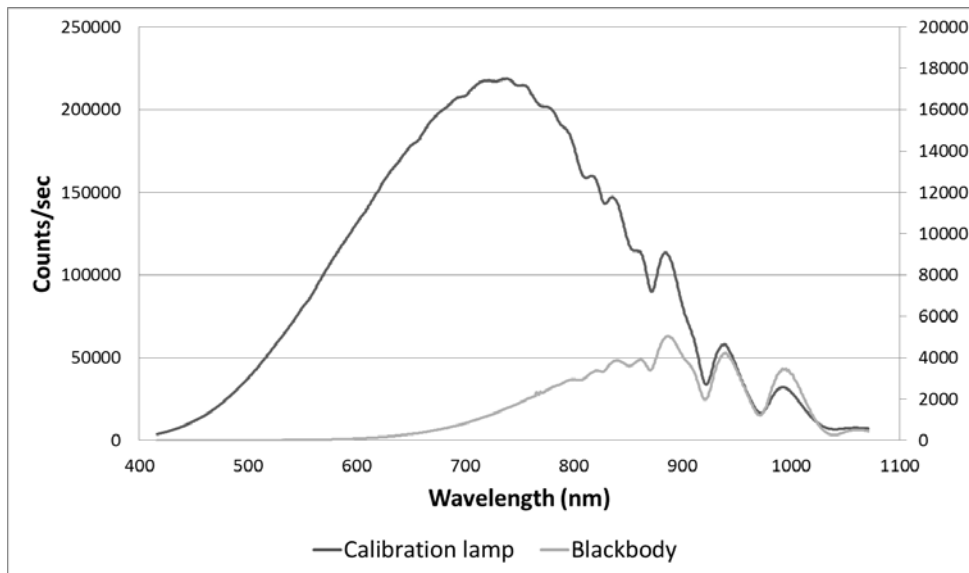


Figure 6-26 Intensity calibration and blackbody spectra (count/sec)

Figure 6-26 illustrates that the blackbody follows the shape of the intensity calibration measurements. Error may have occurred during calibration beyond 900 nm due to second order emission from wavelengths below 590nm. This may possibly be eliminated by using a long pass edge filter during calibration that would block transmission after a given wavelength.

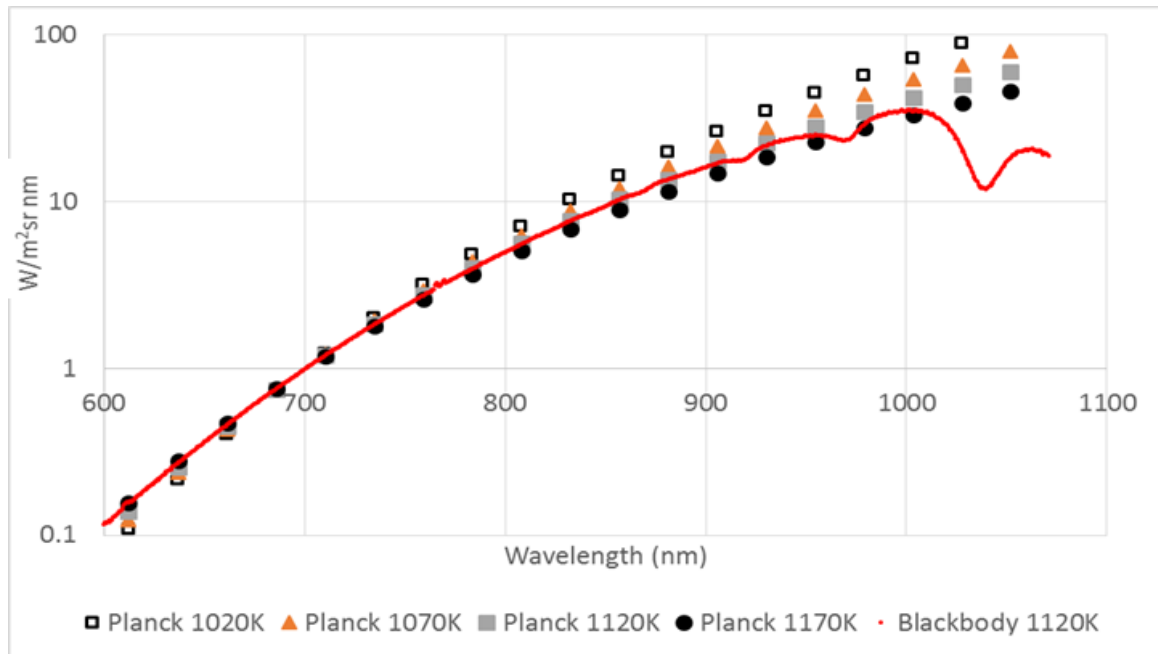


Figure 6-27 Normalized blackbody curve at 700 nm

In terms of absolute radiance as shown in Fig 6-26, the blackbody measurement seems to follow a Planck curve between 1020 K and 1070 K which is clearly lower than the pyrometer temperature which measured 847°C (1120 K). The reasons are not clear so far and an explanation requires more detailed investigation. However, all measurements (i.e. all different samples) are subject to the same calibration, so these effects should compensate when extracting the emissivity values. Therefore an emissivity analysis is

conducted in the following section, keeping in mind that the actual temperature seems to have unknown uncertainties and may be lower than reported by roughly 100 K.

6.4.2.2 Sample Analysis

The results in Figure 6-28 display the measured spectral emissivity for all four conditions of the stainless steel 304 obtained from building the ratio of the emitted intensity from the surface of interest to the blackbody cavity emission. The 0° samples show a higher emissivity than the 30° samples. This is opposite than what the trend obtained in the IR tests showed where the 30° samples had a higher emissivity than the 0° samples. However, for the 0° sample the rough surface has a higher emissivity than the polished surface, but for the 30° sample the polished surface has the higher emissivity value.

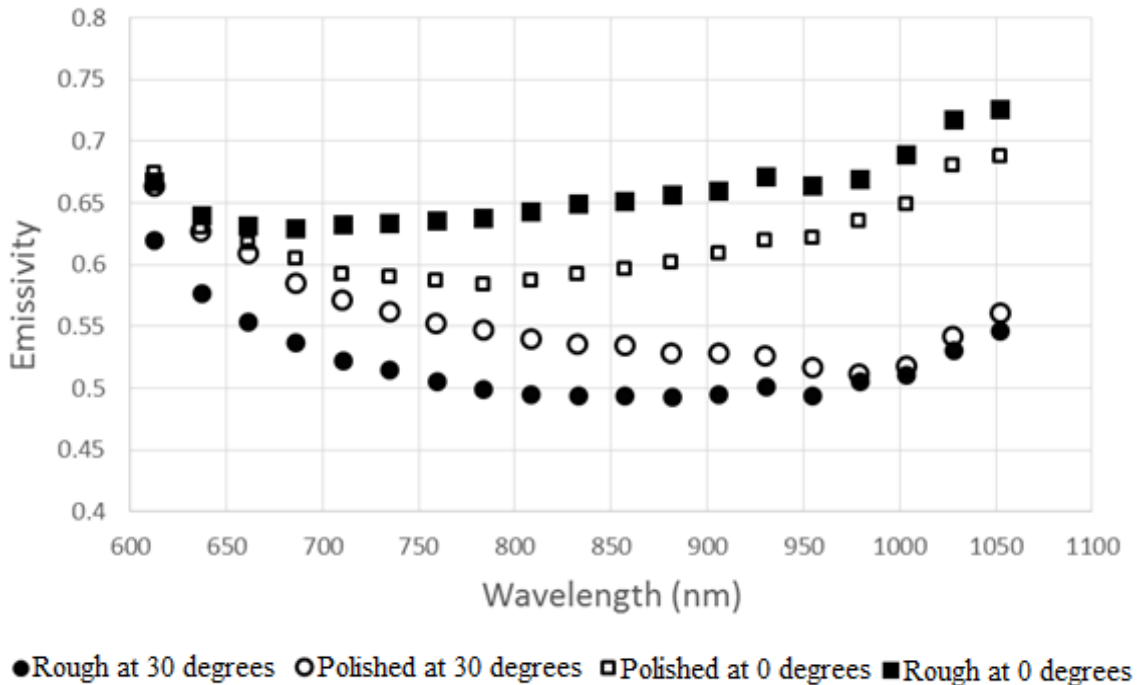


Figure 6-28 Measured emissivity values in visible wavelength for stainless steel 304

Above 900 nm for all four surfaces the measured emissivity decreases and then increases. This resembles the trend seen of the blackbody curve and intensity calibration curve. These results after 900 nm may not be as accurate compared to the results from 600-900 nm. Literature values of normal emittance for oxidized stainless steel 304 up to 525°C have been reported to be 0.62 to 0.73 (Modest). Emissivity varies by approximately 0.15 between all four surface conditions at 800 nm. The 0° samples tend to increase around 775 nm while the 30° samples decrease until about 900 nm. This is an interesting trend and may suggest that the 30° sample is receiving reflective radiation from the radiation shield.

Measurements of radiation reflected from the radiation shield have been performed for the IR camera tests and are presented in the next chapter but were not completed yet for the VIS/NIR measurements since the set-up will have to be moved to another lab for these experiments. For the time being, a more comprehensive series of furnace experiments is planned to be completed first, before moving the set-up and losing all alignment.

7 RADIATION REFLECTED BY SHIELD EXPERIMENT

An experiment was devised to account for error that may result from radiation emitted by the samples to the radiation shield and being reflected back to the samples. An experiment was devised by Joule heating similar sample shapes of stainless steel 304, and measuring the difference in intensity of the samples with the radiation shield covering the sample, and without the radiation shield covering the sample. The sample geometry was based on multiple ANSYS simulations to maximize the temperature reached by the samples under direct current while reducing the amount of cutting needed to be done on the sample. Three different mounting blades were designed to hold the sample at these positions to simulate the three tilting angles measured.

7.1 ANSYS Simulations

The finite element analysis (FEA) model was developed and executed with ANSYS Workbench 16.0. The model was built with the thermal electric modular. For this design, two simulations were executed for each material: stainless steel 304 and titanium 6Al-4V.

7.1.1 Geometry and Mesh Size

The geometry chosen for this simulation included the copper terminals, stainless steel blades, and the sample. The sample size was chosen to be similar to that used in the furnace experiment. Early experiments showed that it would be necessary to have a small cross sectional area for the current to pass through.

Similar to the low heat and vacuum chamber simulations, the mesh size that was implemented was coarse. However, the body size was used to control the element size of

the sample. This was done since the highest Joule heating would be taking place across a small cross sectional area. A finer mesh results in a more accurate temperature distribution across a small area. The body size feature was also applied so a coarse mesh could be applied across larger bodies (i.e. the copper clamps) that would not be undergoing as much heat generation.

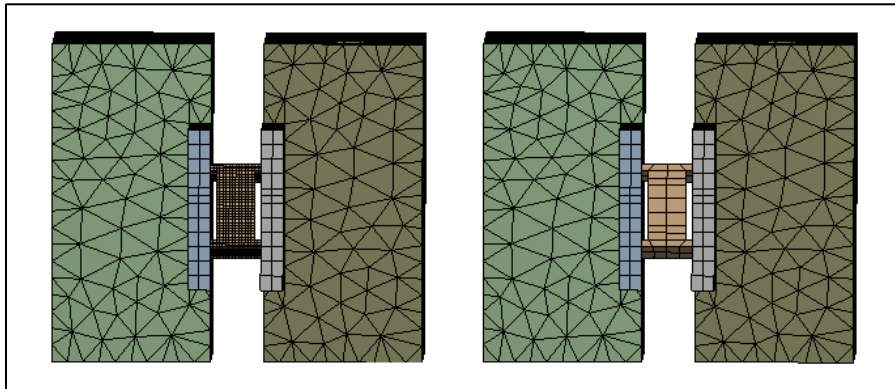


Figure 7-1 Comparison of sample mesh sizes for ANSYS Simulation

7.1.2 Boundary Conditions

Two electrical boundary conditions were applied to the model. 0 volts was applied on the back of one copper terminal and 250 amperes were applied to the back of the one. Since water cooling would be employed, a 10°C temperature boundary condition was applied on the surface of the water channels in the copper terminals. Convection was also applied to the model. A convection heat transfer coefficient of 15 W/m²*K was applied to the sample and steel blades. This large heat transfer coefficient was chosen to ensure enough heat generation will take place to reach the target temperature. A convection film coefficient value of 5 W/m²*K was applied to the outer surfaces of the copper terminal. Radiation emitted by the sample was taken into account by applying an emissivity of 0.6

to the surface of the sample and stainless steel blades. For the titanium sample, an emissivity of 0.35 was used based on reported values [Welsch].

7.1.3 Simulation Results

7.1.3.1 Stainless Steel 304

Figure 7-2 and 7-3 show that the stainless steel reaches a maximum temperature of 860°C and that the sample reached a maximum temperature of 1075.8 °C at 250 amperes. This is 125°C higher than the maximum temperature reached in the furnace for measuring spectral, directional emissivity. Figure 7-2 shows that with water cooling the temperature of the copper blocks will be at a safe operating temperature. Figure 7-3 also highlights that the sample will not be at a uniform temperature. However, the minimum temperature of the sample is not below 950 °C.

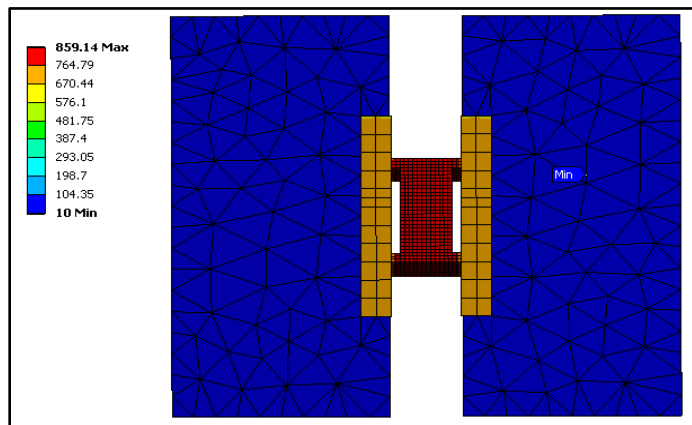


Figure 7-2 Simulated temperature profile at 200 amperes for steel

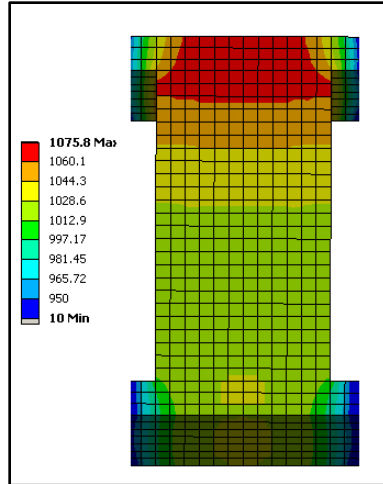


Figure 7-3 Simulated temperature profile at 250 amperes for steel

7.1.3.2 Titanium 6AL-4V

For titanium, a maximum temperature of 1031.4 °C was reached at 200 amperes which is 80°C higher than the maximum temperature reached in the furnace. At no point of the sample surface does the temperature decrease by more than 95 °C below this value. At 250 amperes, the temperature may reach up to 1300°C. This leaves more margin in the simulations for the titanium sample than for the stainless steel sample since achievable temperatures are clearly higher than needed to mimic the temperatures in the furnace experiments.

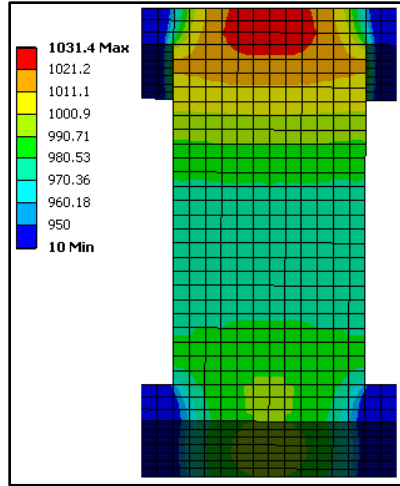


Figure 7-4 Simulated temperature profile at 200 amperes of titanium sample

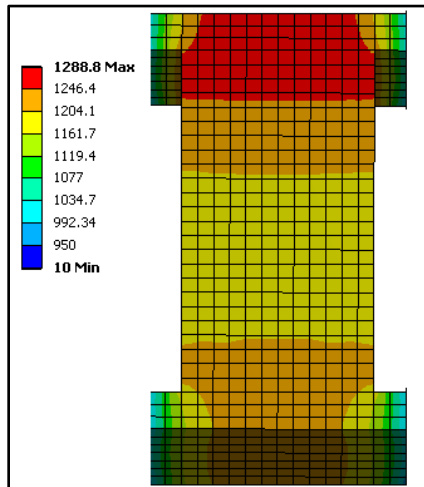


Figure 7-5 Simulated temperature profile at 250 amperes of titanium sample

7.1.4 Final Design

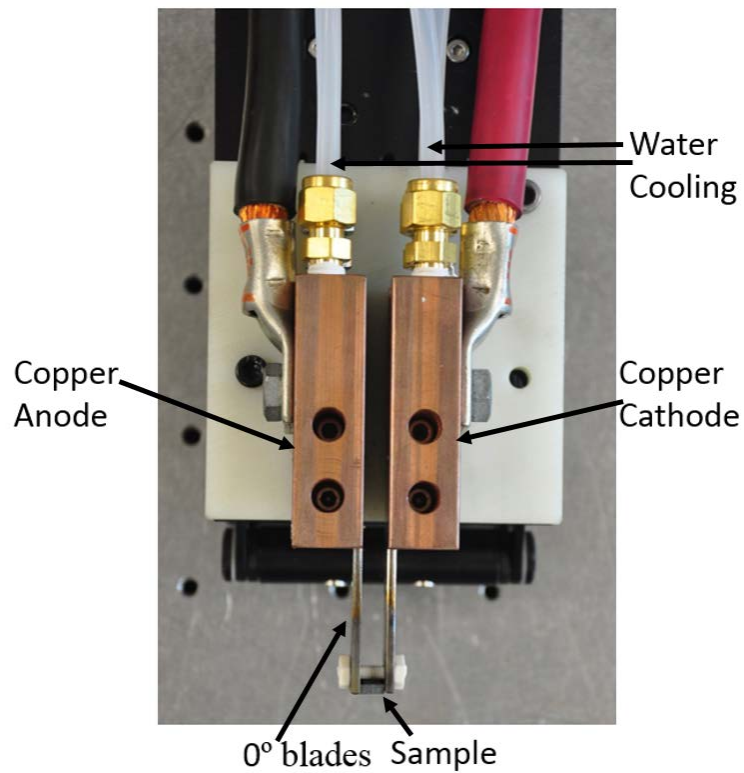


Figure 7-6 Top view of reflected irradiation setup

The final design included two water cooled copper terminals with slots machined on the inside for different sets of blades to be mounted. The setup was mounted to a nylon plate to electrically isolate it from the optical table. The blades were originally designed to be clamped by a ceramic screw. However, this solution made it very difficult to get sufficient contact between all four feet of the samples and the blades. Without complete contact, local hot spots develop at the feet leading to a portion of the sample being heated by conduction only instead of Joule heating. To eliminate these hot spots, a C-clamp was utilized to clamp the blades as shown in Figure 7-7. Between the C-clamp and the blades

a calcium silicate layer was used as an electrical isolator between the C-clamp and the blades.



Figure 7-7 Clamping Mechanism

7.2 View factor calculations

The view factors from the 0° sample to our radiation shield and from the radiation shield to the 0° sample were calculated. The assumptions used in this analysis is that every surface is gray and diffuse, and the surfaces are separated by a nonparticipating medium. This was done by defining the following surfaces: A_1 , A_2 , A_3 , and A_4 where A_1 is an imaginary cap on the radiation shield opposite to the side of our sample to form an enclosure for the application of a summation rule. A_2 is defined by the sides of the radiation shield. A_3 is the sample itself. A_4 is the surface of an imaginary cap minus A_3 .

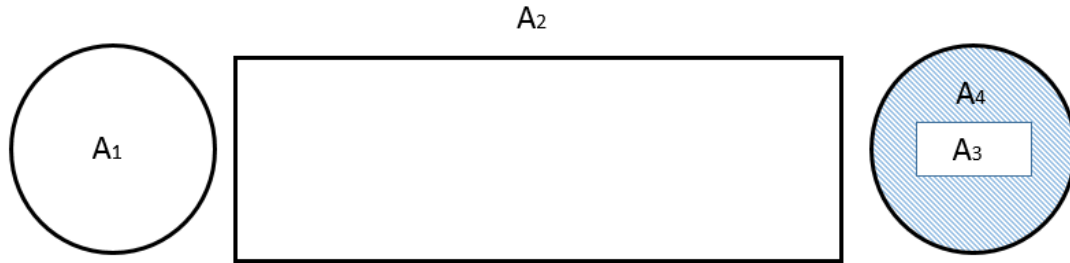


Figure 7-8 Area definitions for view factor calculations

To determine the amount of radiation that would be reflected back to our sample by the sides of the cylinder wall, the following equations and assumptions were used. First, it was assumed that $F_{3-3} = 0$ and $F_{4-4} = 0$ since they are co planar surfaces. Next, the summation relation of view factors, equation 7-1, was used (Abishek and Katte).

This yield:

$$F_{3-1} + F_{3-2} = 1 \quad \text{(Equation 7-1)}$$

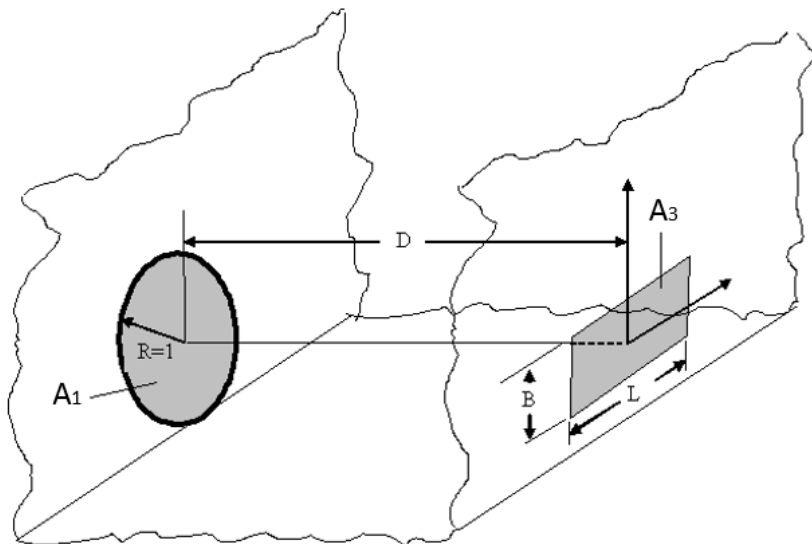


Figure 7-9 Variable definition for equation 7-2

$$F_{3-1} = \frac{1.0152(1 + L^{1.0251})(1 + B^{3.4915})}{(1 + L^{1.195})(1 + B^{3.656})[D^{1.9767} + (1 + D)^{0.3047} - 0.0175]} \quad (\text{Equation 7-2})$$

Equation 7-2 based on figure 6-4 was used to find F_{3-1} . Next, equation 7-1 was used to find F_{3-2} (Absheik and Katte). Finally, the law of reciprocity for view factors (equation 7-3) was used to find F_{2-3} .

$$F_{3-2}A_3 = F_{2-3}A_2 \quad (\text{Equation 7-3})$$

Table 7-1 View factor results with D=6.5"

F_{3-1}	F_{3-2}	F_{2-3}
1.20E-02	9.88E-01	2.85E-03

If the view factors are calculated assuming A_3 is 6.5" (length of radiation tube) from the sample, then the actual view factor from the shield to the sample is very small. The view factor from the radiation shield to the sample may change though, depending on the point of interest on the radiation shield. Figure 7-10 shows that the view factor is above .01 at the tip of the radiation shield located by the sample. This starts to decrease though as the point of interest of the radiation shield becomes further away from the sample.

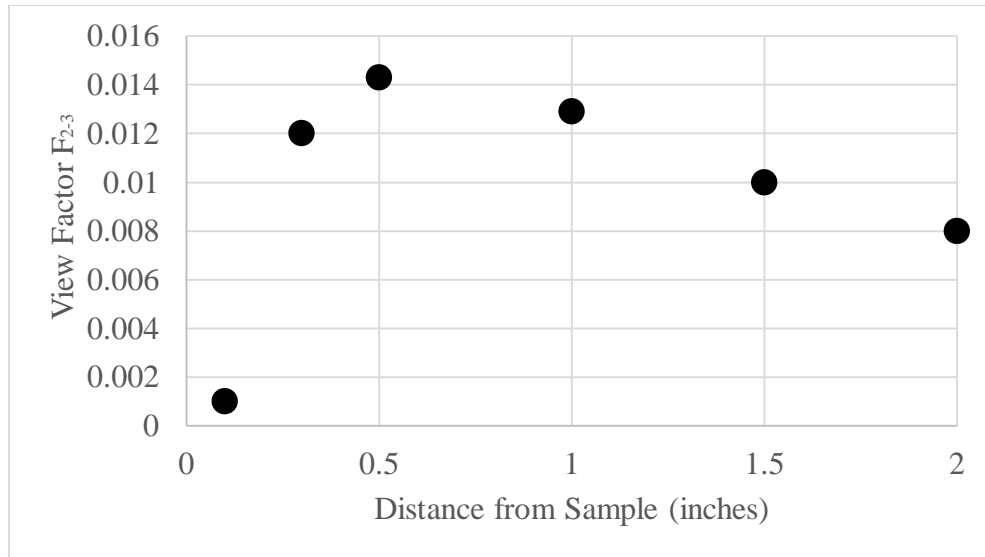


Figure 7-10 View factor from shield to sample

7.3 Reflectivity experimental setup

7.3.1 Experimental Setup

This experiment was performed in the Radiation Sciences Laboratory in Ralph G. Anderson 318 on the optical table in ambient air as shown in Fig. 6-6. Direct current was fed to the copper cathode by the Magna-Power XR16-250/208 power supply via 3/0 AWG cable. The temperature of the copper clips were kept constant at 12°C by chilled water that was circulated through both pieces.

7.3.2 Experimental Procedure

- 1) Mount the first sample and the 0° blades on the copper cathode and anode.
- 2) Turn the chill water on and attach the electrical cables to the copper cathode and anode.
- 3) Apply the current needed to heat the sample to at least 1050°C.
- 4) Take measurement with the IR camera.

- 5) Slide the radiation shield out of the adapter chamber and over the sample. Take second measurement with IR camera.
- 6) Slide the radiation shield back into the adapter.
- 7) Hold a black plate in front of the IR camera and take a background measurement.
- 8) Decrease the applied amperes by 10 amperes and repeat steps 3-6.
- 9) Turn the power supply off, disconnect the power supply and unmount the sample.
- 10) Repeat steps 1-7 for 30 °and 60° blades

7.4 Experimental Analysis

MATLAB r2014B was used to carry out calculations, and the code is available in Appendix 4. First, the average of the ten frames for each condition was calculated. Second, the average background radiation was subtracted from without the radiation shield covering the sample, WOS , and with the radiation shield covering the sample, (WS).

$$[WOS_{A-BG}] = [WOS_A] - [BG_A] \quad \text{(Equation 7-4)}$$

$$[WS_{A-BG}] = [WS_A] - [BG_A] \quad \text{(Equation 7-5)}$$

Third, the energy reflected from the shield, RE , was calculated with equation 6-9.

$$[RE] = [WS_{A-BG}] - [WOS_{A-BG}] \quad \text{(Equation 7-6)}$$

7.5 Experimental Results

7.5.1 Experiment one: no anti-reflective paint

The goal of the first set of experiments conducted was to determine how much radiation is reflected back to the sample from the radiation shield with no anti-reflective paint.

Figure 7-11 displays a surface plot calculated with Eq. 7-6.

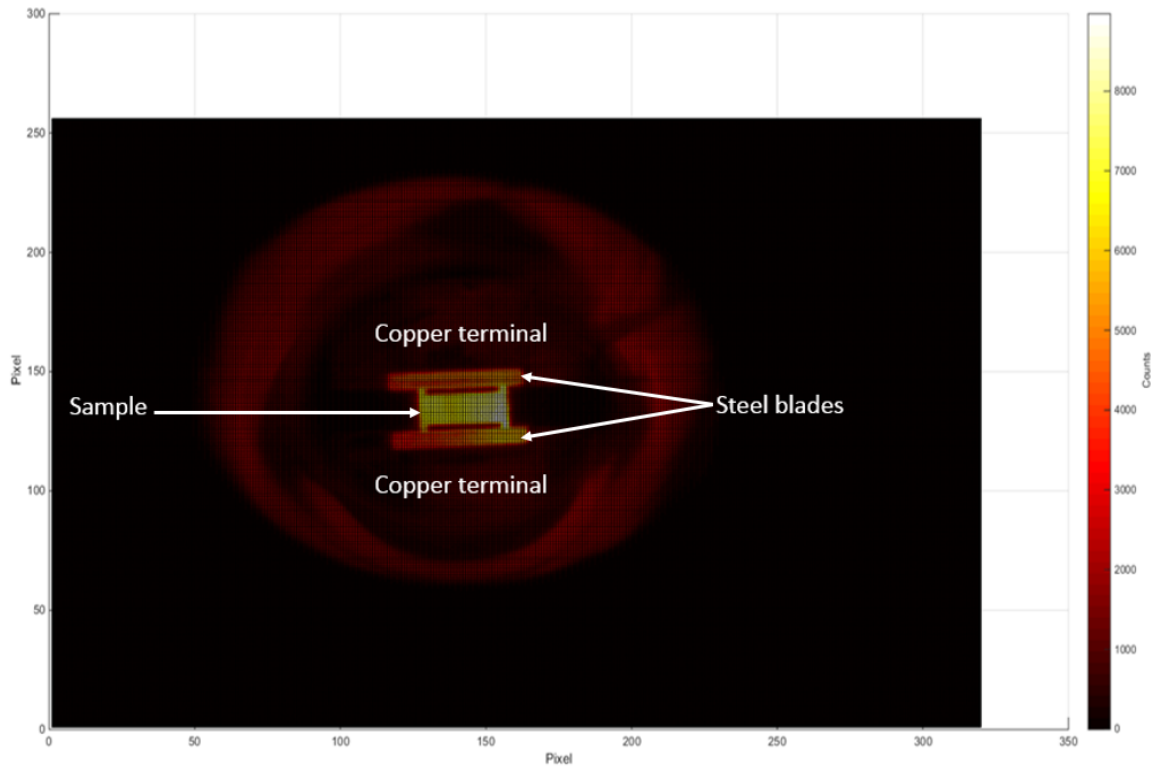


Figure 7-11 Experiment 1: Surface plot without shield covering sample at
 0°

Figure 7-12 through Figure 7-14 displays the zoomed surface plots of the sample and steel blades for 0° , 30° , and 60° . The 0° sample has less reflected irradiation than the ones under 30° and 60° . This is to be expected since the view factor from the 0° sample to the

radiation shield is lower than the view factors from the 30° and 60° sample to the radiation shield.

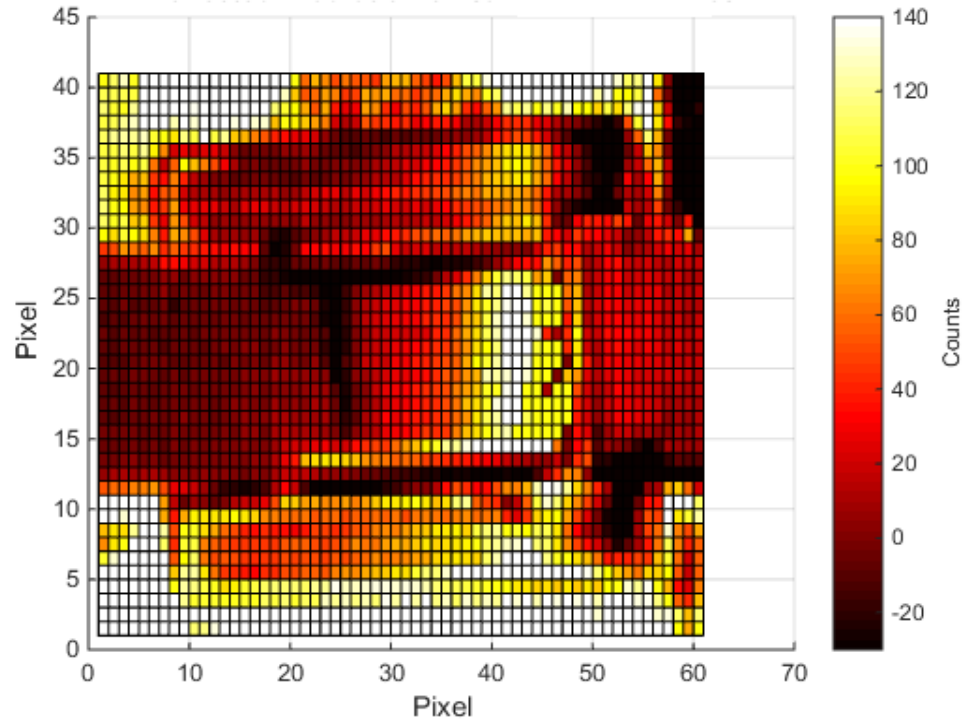


Figure 7-12 Experiment 1 reflected irradiation on sample at 0°

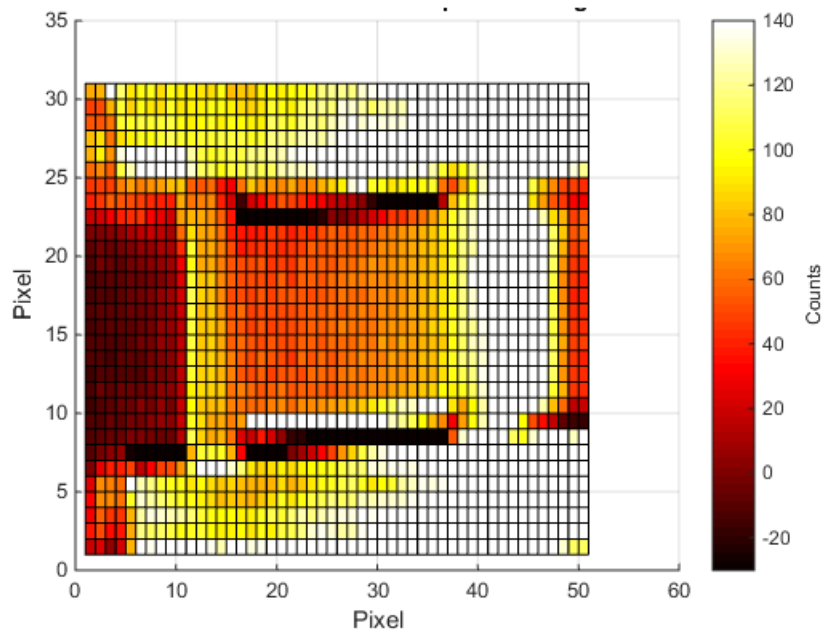


Figure 7-13 Experiment 1 reflected irradiation on sample at 30°

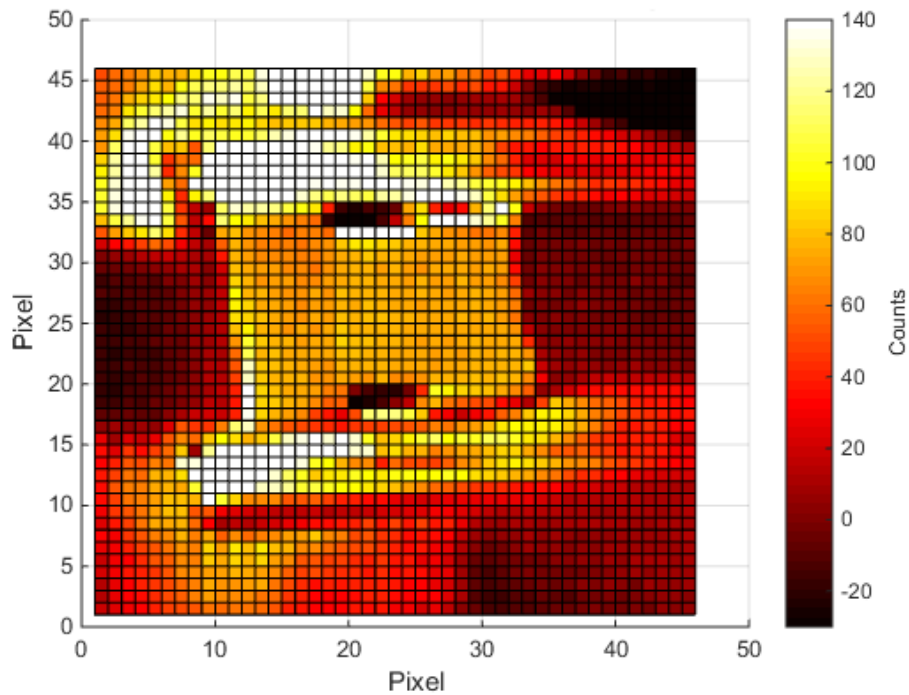


Figure 7-14 Experiment 1 reflected irradiation on sample at 60°

7.6 Analysis and Conclusions

Table 7-2 displays the average counts for each surface after negative values were removed and values higher than two standard deviations were removed. Table 7-3 displays the percent increase for the graphite sample, 0° sample, and 30° sample based upon the results in section 6.5 from the isothermal test.

Table 7-2 Average count difference across each sample

0°	30°	60°
52	69	75

Table 7-3 Percent difference for counts measured in isothermal test based on reflectivity measurements

0° Sample	Graphite	30° Sample
1.4	0.81	1.3

The results from this test show that there is no significant increase due to the reflection from the radiation shield. Likewise, the results from the view factor calculations in 6.2 support this as well with the view factor being less than 1.5%

8 CONCLUSIONS

This thesis has presented an experimental method for measuring spectral, directional emissivity at high temperatures. This involved designing a custom built radiation shield adapter for an existing furnace with optical access to block unwanted emission. This design proved to be successful as no testing has shown an issue with the radiation shield heating above 200°C. However, the overall setup went through several design iterations including redesigning the sample holder and sample size to eliminate unwanted reflected radiation. Experimental procedures and assumptions were also modified including the method in which temperature measurement was performed. Initially, sample temperatures were assumed to be equal to a thermocouple located in the proximity of the sample. However, it was later determined after comparing results to a pyrometer that the sample temperature and furnace temperature were biased by 100°C. Thus, temperature values to calculate the emissivity should be determined with the pyrometer that is measuring the temperature of graphite instead of the thermocouple located inside of the furnace. The spectral shape of Planck radiation of a blackbody cavity in the graphite sample measured in the visible to near infrared agrees well with the pyrometer temperature. Current discrepancies between intensity and the spectral shape of the radiation emitted by this cavity will still have to be resolved in future measurements. Ideally, a thermocouple should be positioned on the sample but due to the configuration of the furnace and radiation adapter this was not feasible.

Results in this thesis indicate that is possible to use the infrared camera and spectrometer setup to measure spectral emissivity. However, initial results show that the blackbody

does not agree well with spectral Planck radiation above 900 nm. It is highly possible this may be due to errors performed during the intensity calibration for the spectral measurements in the visible wavelength. In future measurements it is planned to apply an edge filter to block second order radiation and improve the accuracy of these measurements.

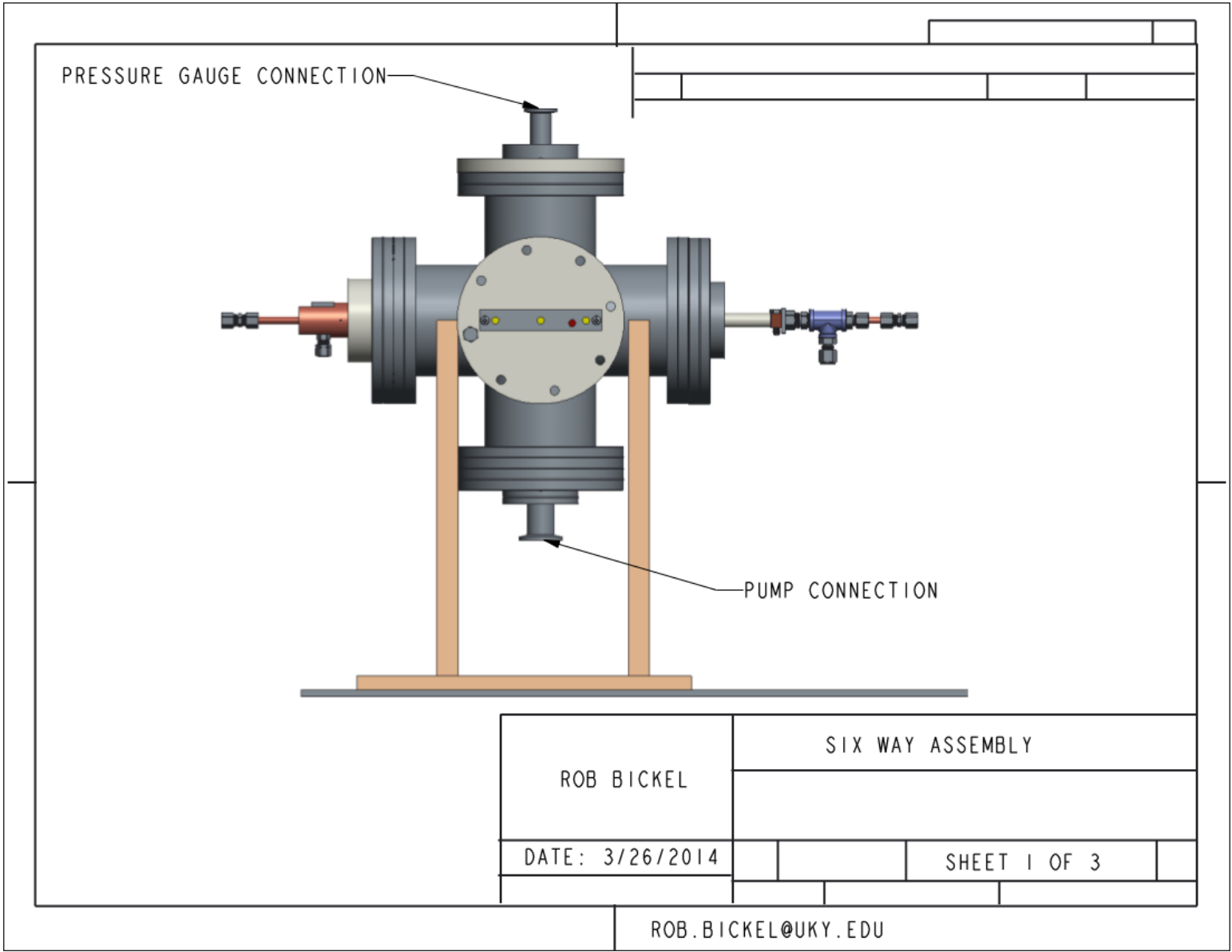
Nonetheless, emissivity values were extracted for stainless steel 304 for two surface conditions at 0° and 30° in the visible regime. These data serves as a starting point for determining the reliability of future emissivity measurements of NASA samples.

There is plenty of future work that may be undertaken in regards to measuring spectral, directional emissivity at the University of Kentucky. This work includes:

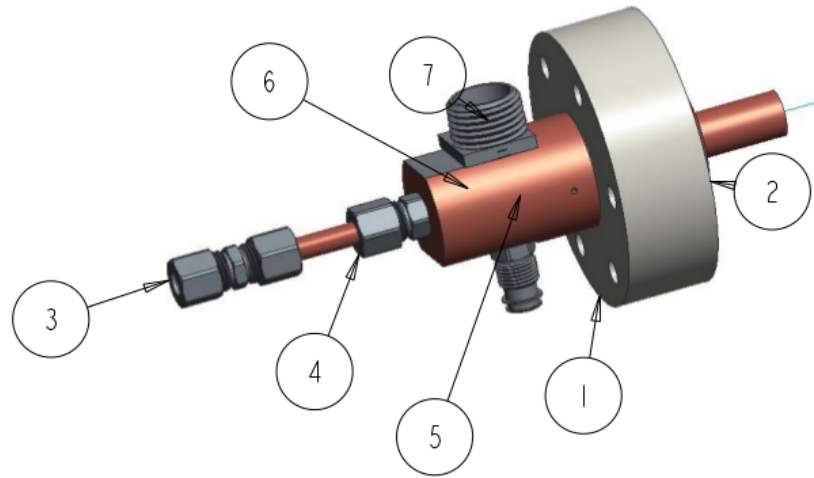
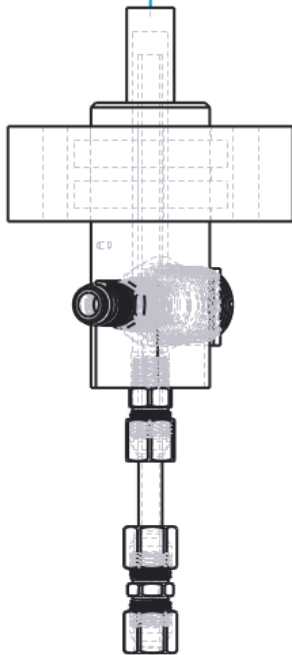
- 1) Completing emissivity measurements of further sample materials, roughnesses, and directions in the visible and infrared regime specified by a NASA test matrix.
- 2) Completing additional radiation shield reflectivity measurements with stainless steel and titanium at the minimum and maximum surface roughness to confirm the conclusions in chapter 6.
- 3) Designing a mirror to allow for sample measurements in the visible and infrared wavelengths to take place in the same test sequence.
- 4) Measuring the temperatures of the sample in the radiation reflected by the radiation shield experiment with a calibrated infrared camera and comparing these measurements to the results in the ANSYS simulations.

In addition, a method of measuring Joule heating and comparing results from experiments to ANSYS simulations has been developed and was applied to a set-up supporting the emissivity measurements. The first two Joule heating experiments presented demonstrated the importance of defining a system and the boundary conditions associated with them. The results from these two experiments also demonstrate that it is possible to obtain accurate results predicting Joule heating with ANSYS simulations. Without knowledge gained from the first two chapters, temperature distributions across Joule heated sample would not have been understood fully. This would have possibly resulted in an under designed system when measuring the radiation reflected by the radiation shield in chapter six. Furthermore, the knowledge gained in the ANSYS simulation has led other members in the Radiation Sciences Lab to utilize ANSYS in their Joule heating research.

APPENDIX 1 ASSEMBLY DRAWINGS



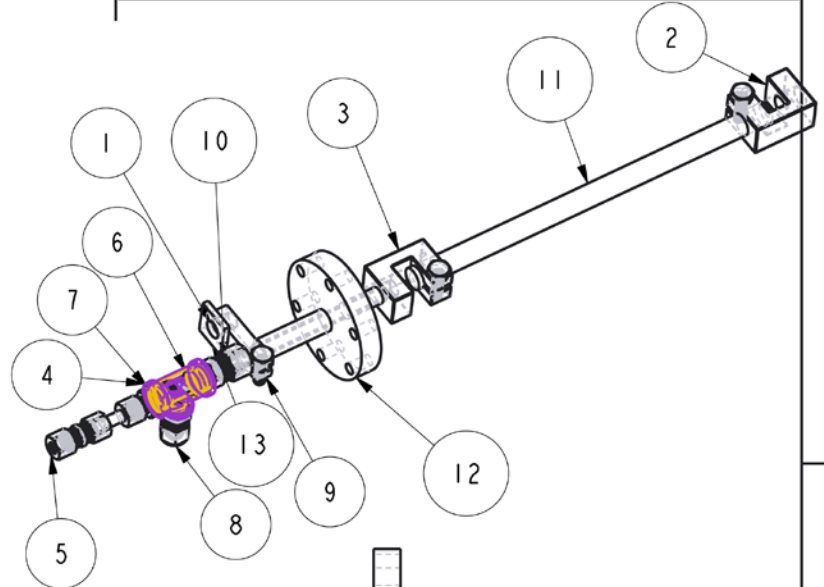
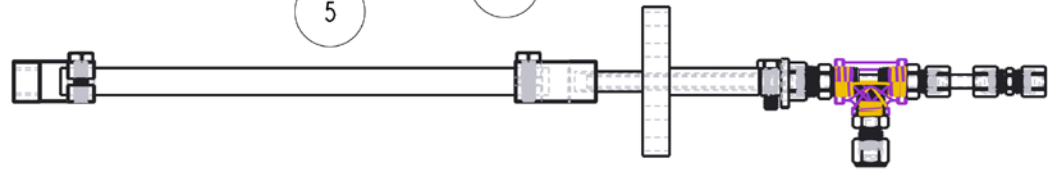
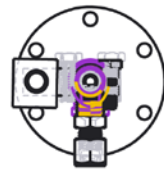
7	TERMINAL_RING_1	1
6	ANODE_INLET_TUBE	1
5	5220K640	1
4	50915K314	1
3	50915K133	1
2	05_COPPER_ROD	1
1	03_TEFLON	1
ITEM NO	PART NUMBER	QTY



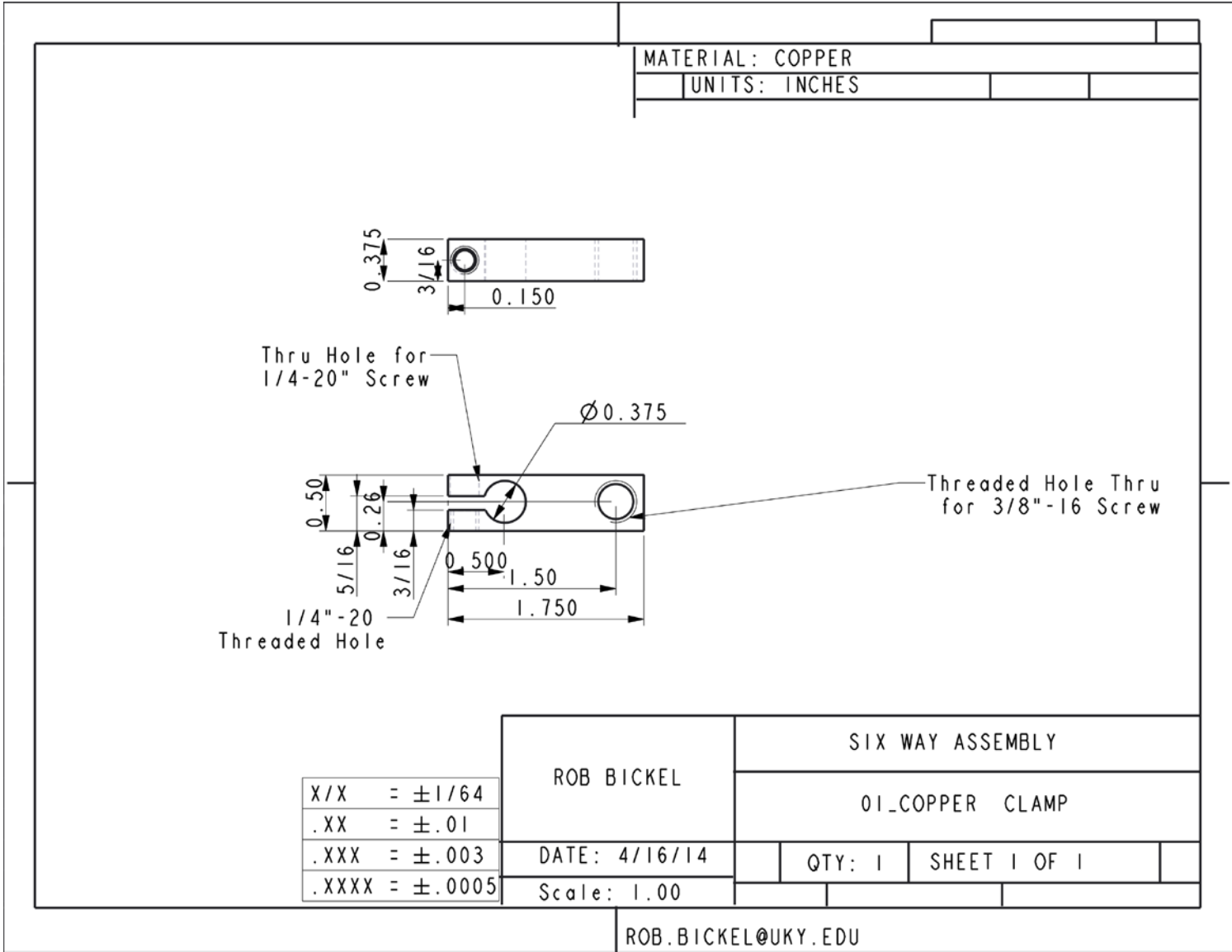
ROB BICKEL	SIX WAY ASSEMBLY		
DATE: 3/24/14		SHEET 2 OF 3	

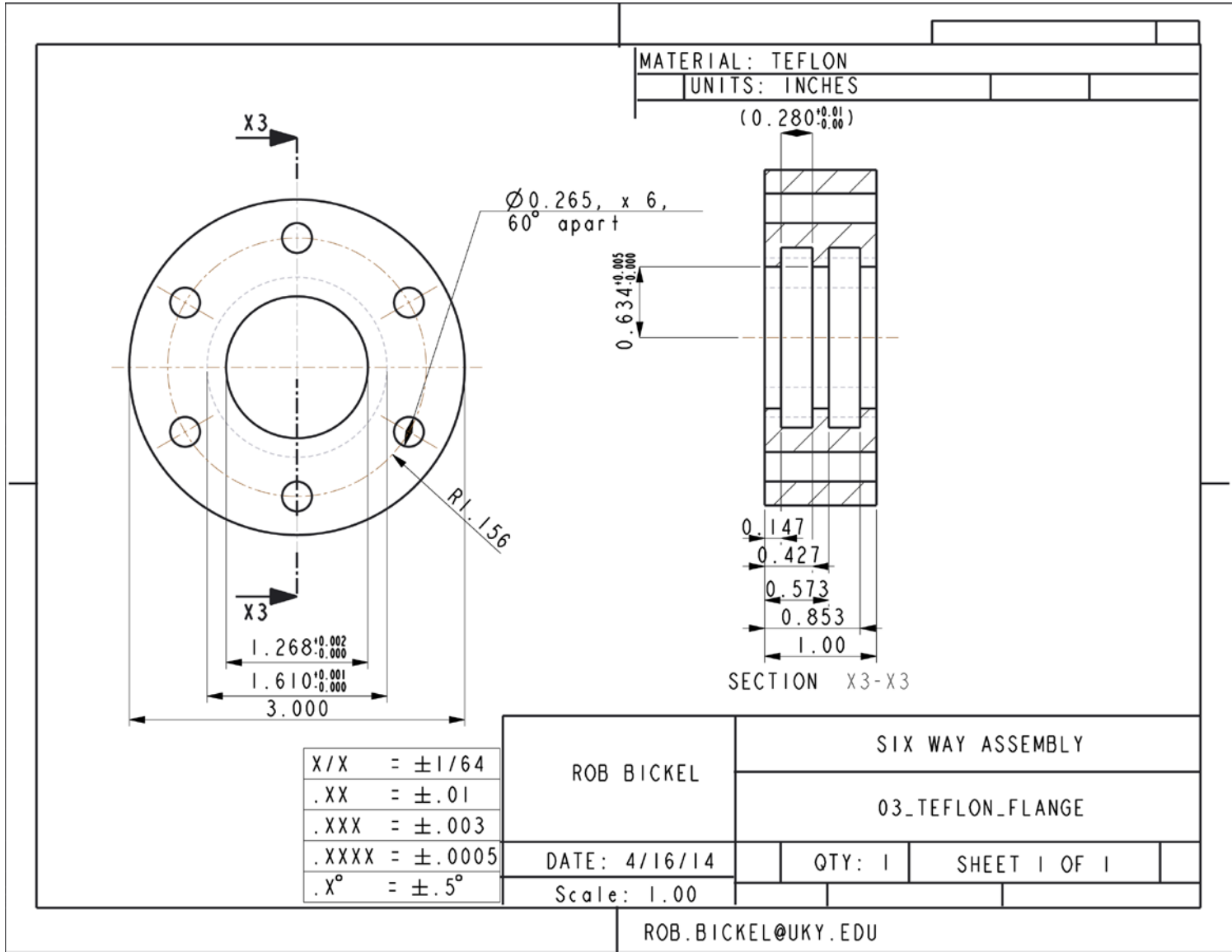
Rob.Bickel@uky.edu

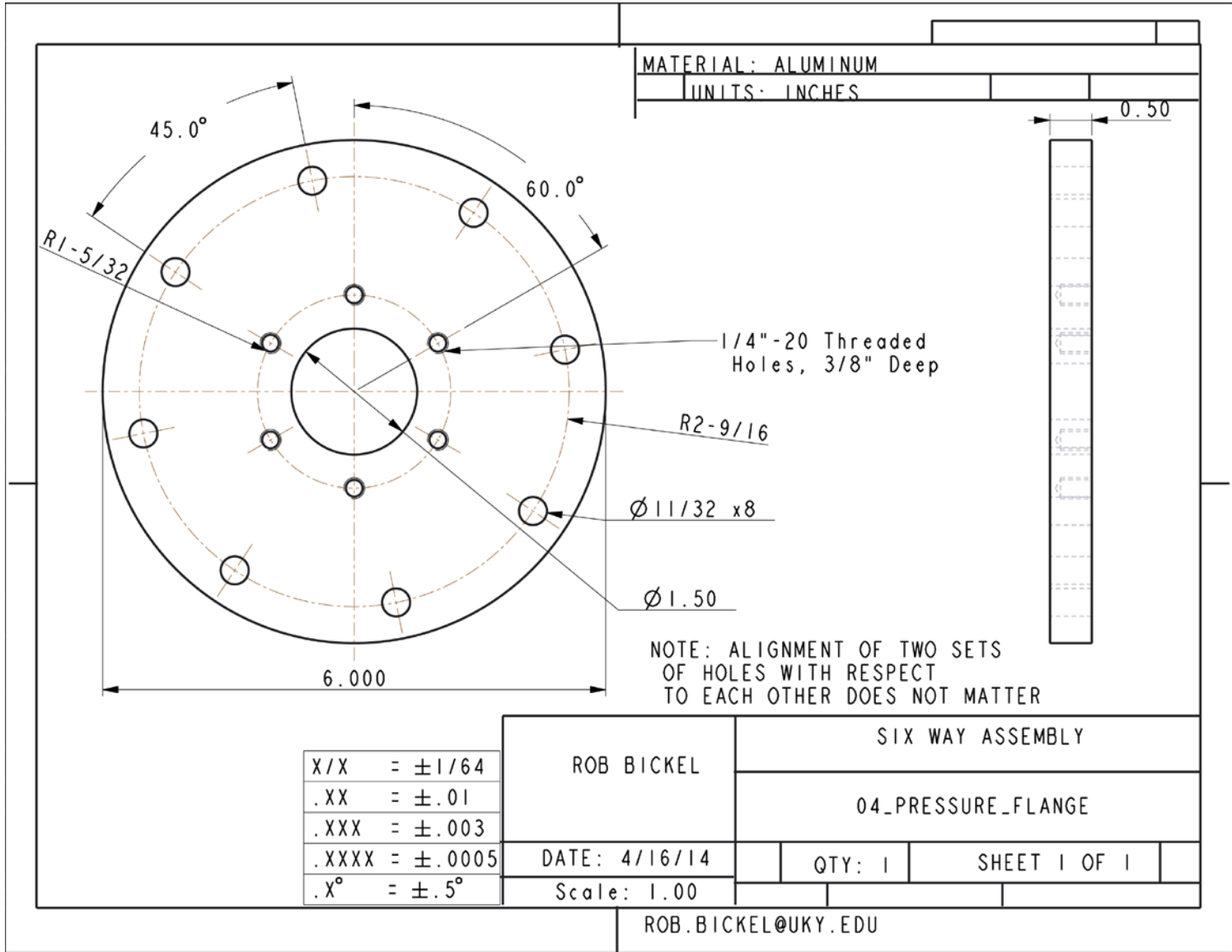
13	TERMINAL RING	1
12	POWER FEED-THRU FLANGE	1
11	GRAPHITE ROD	1
10	CATHODE_INLET_TUBE	1
9	1/4-20" CAP SCREW	1
8	COMPRESSION FITTING	1
7	COMPRESSION FITTING	1
6	COMPRESSION FITTING	1
5	COMPRESSION FITTING	1
4	T FITTING	1
3	07_CLAMP_INTERIOR_02	1
2	02_CLAMP_INTERIOR_01	1
1	01_COPPER_CLAMP	1
ITEM NO	PART NUMBER	QTY

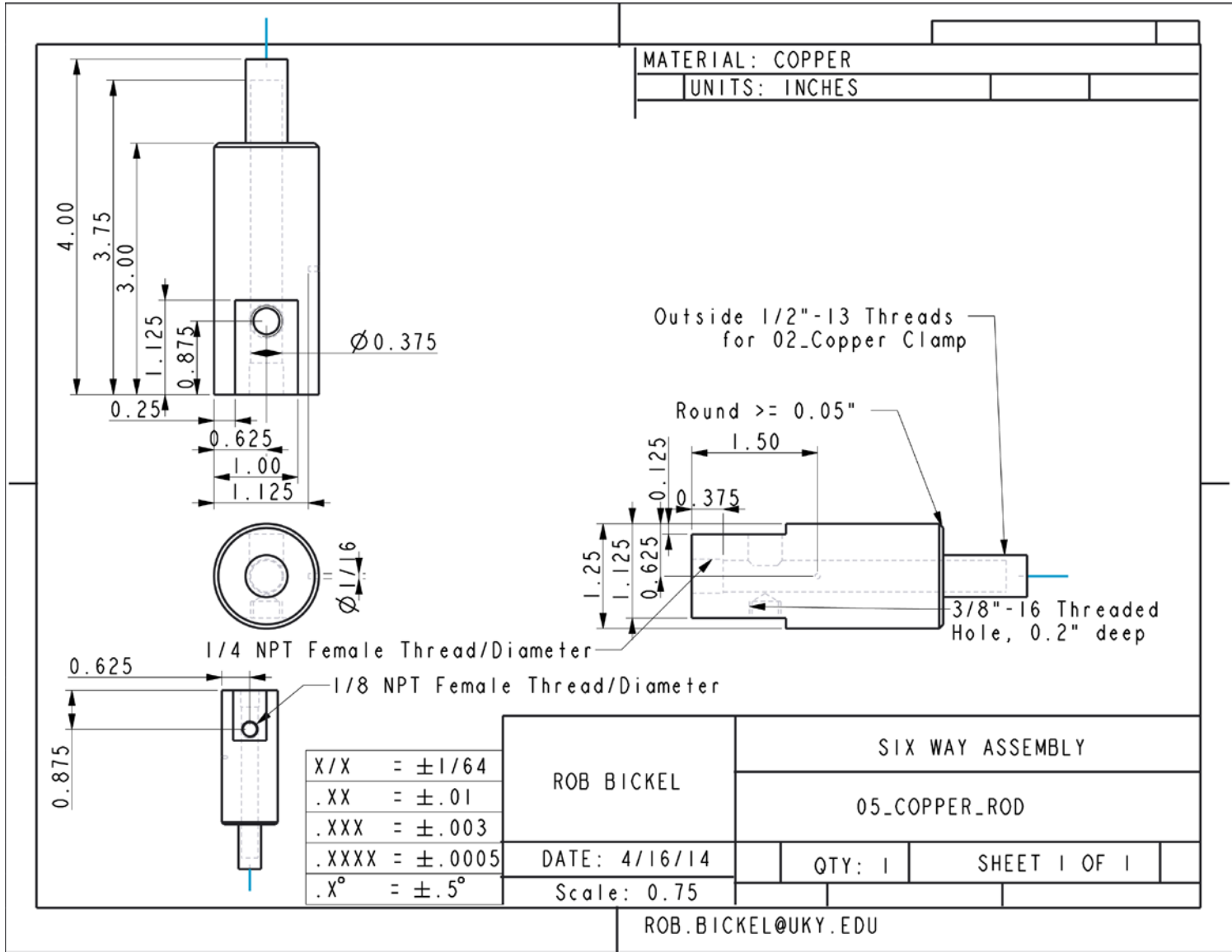


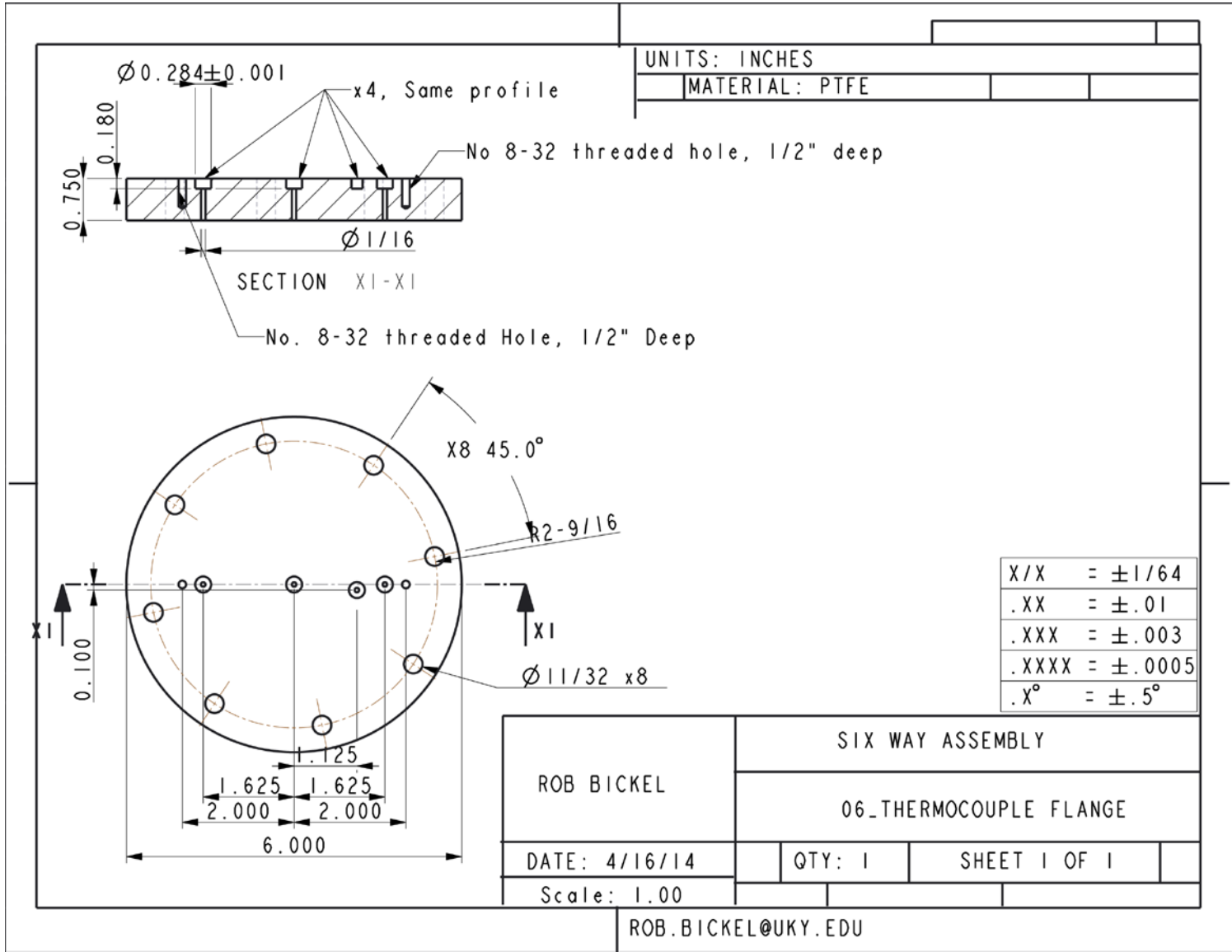
ROB BICKEL	SIX WAY ASSEMBLY		
DATE: 3/26/2014		SHEET 3 OF 3	

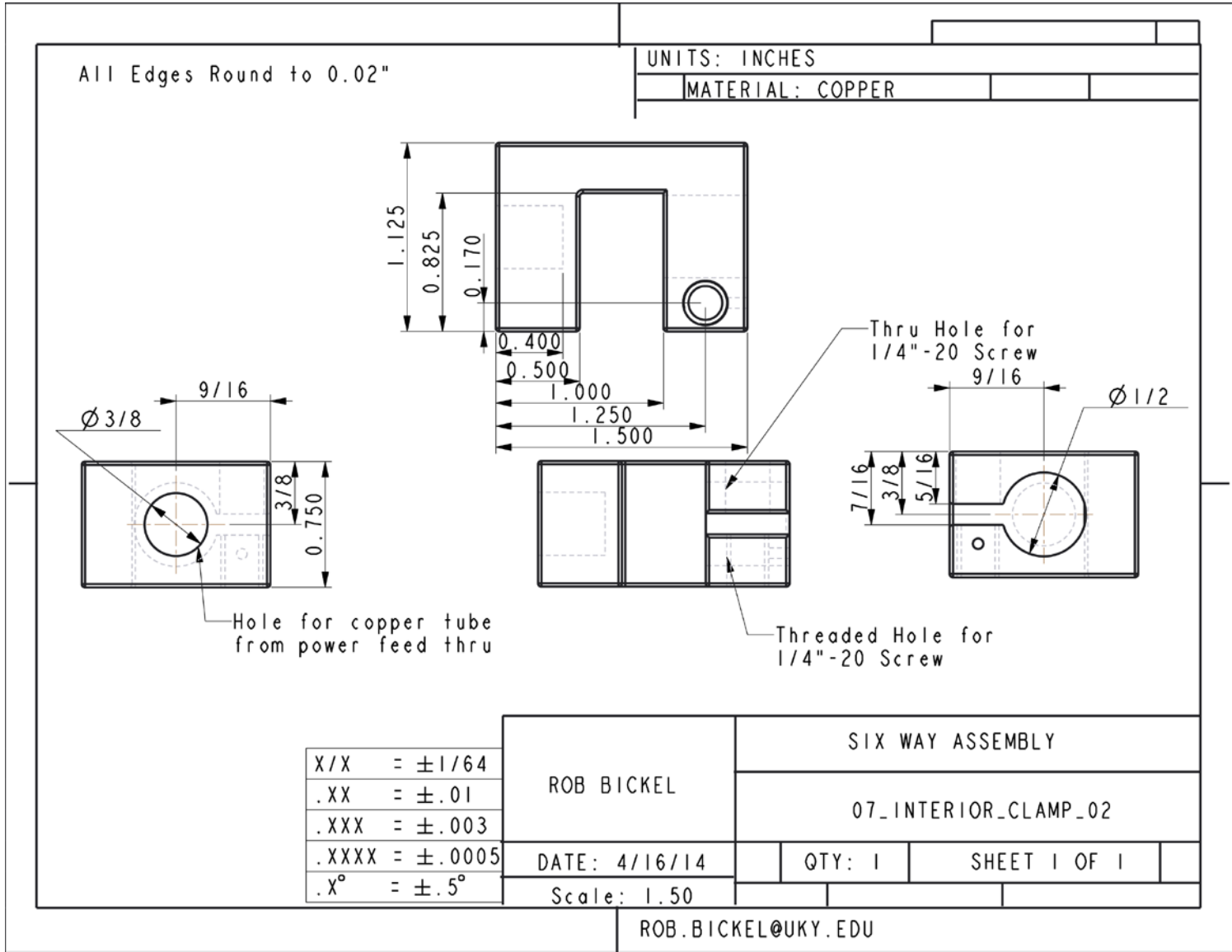


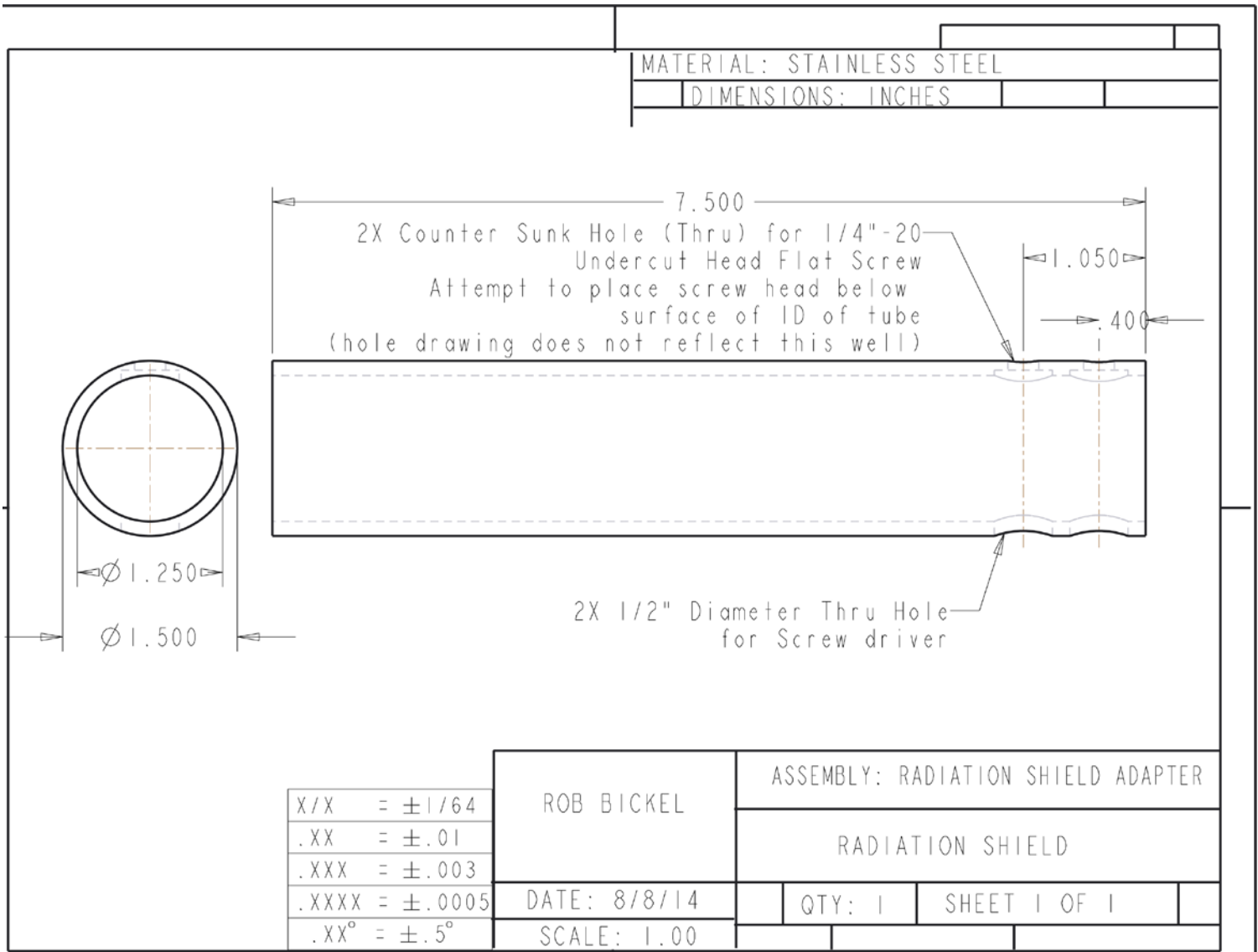


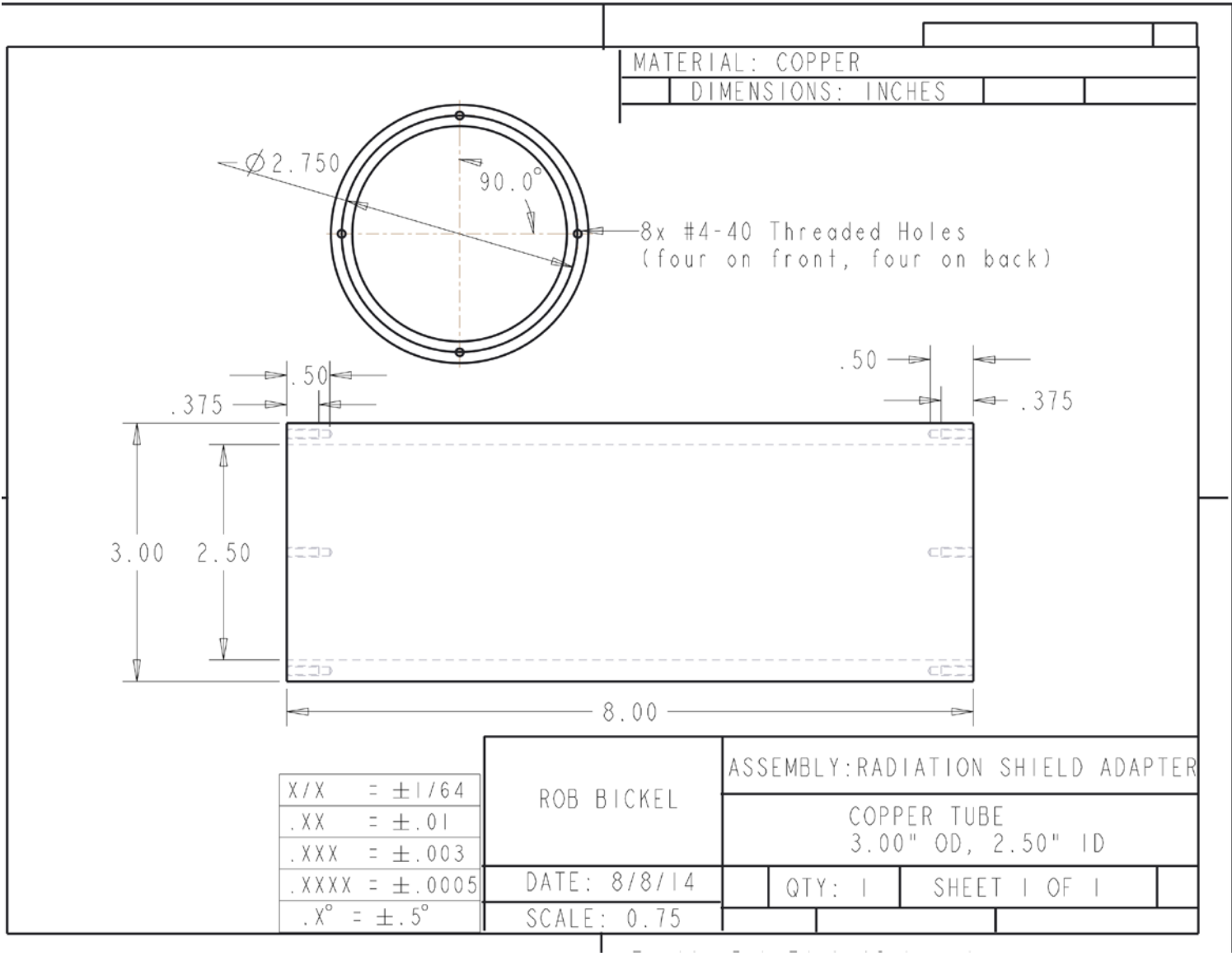


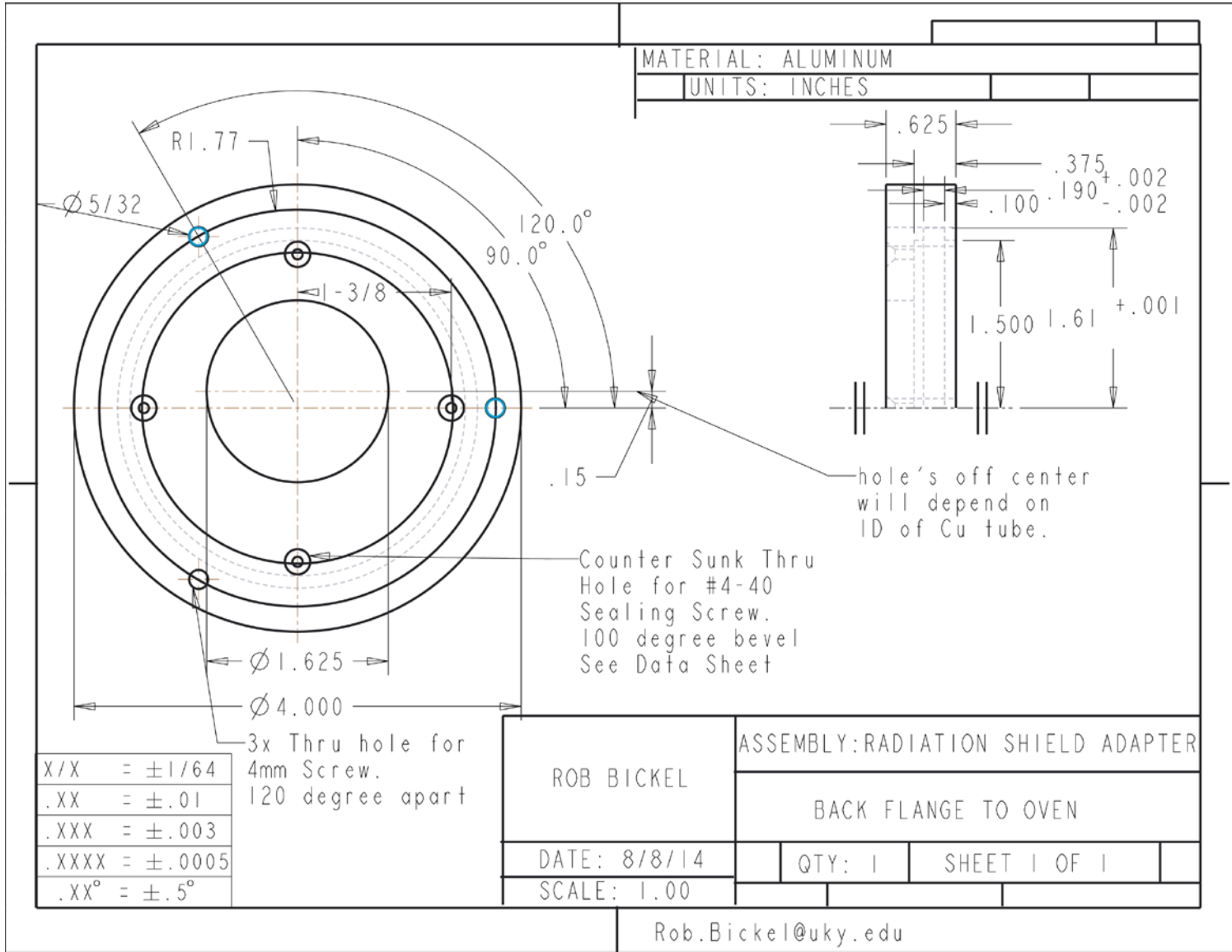


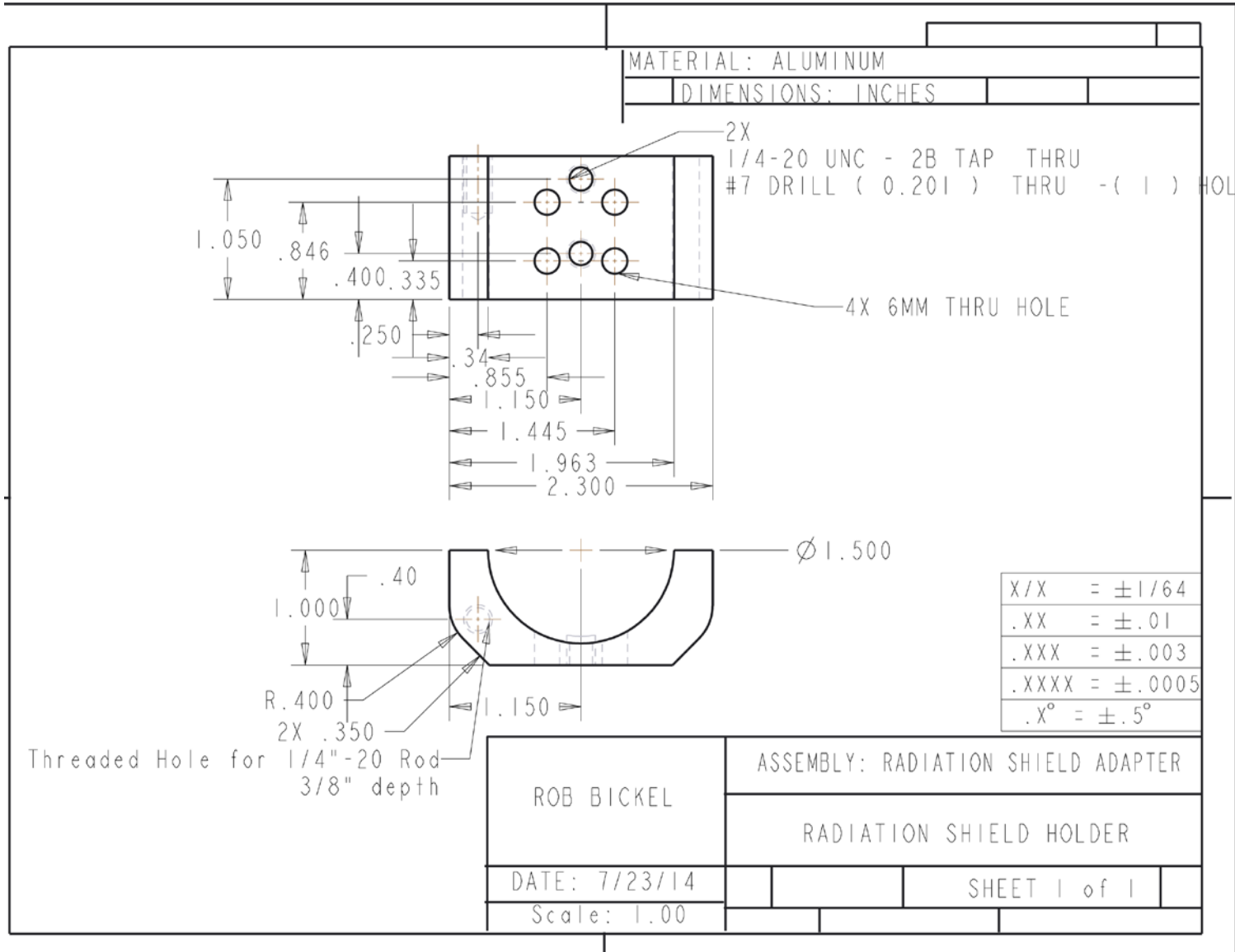


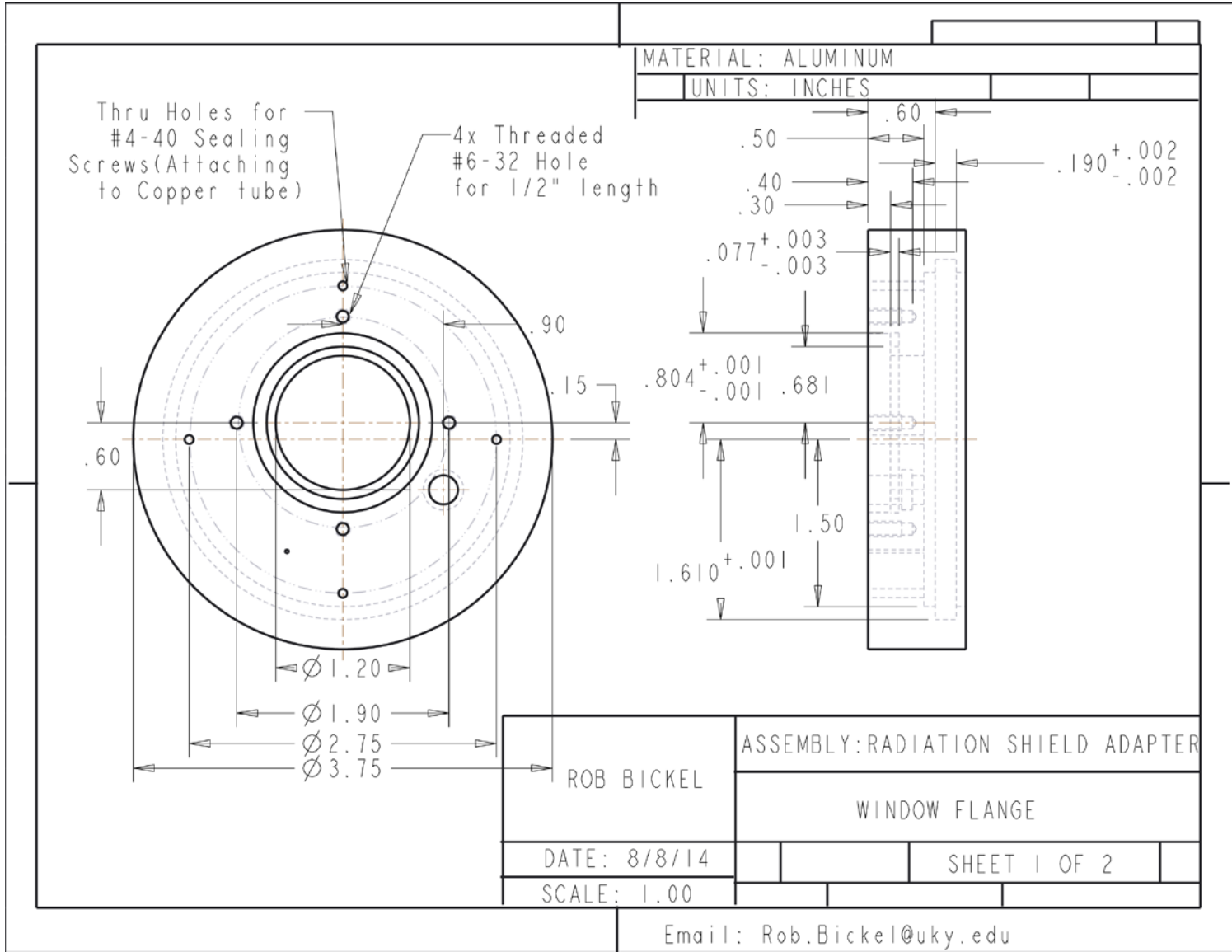


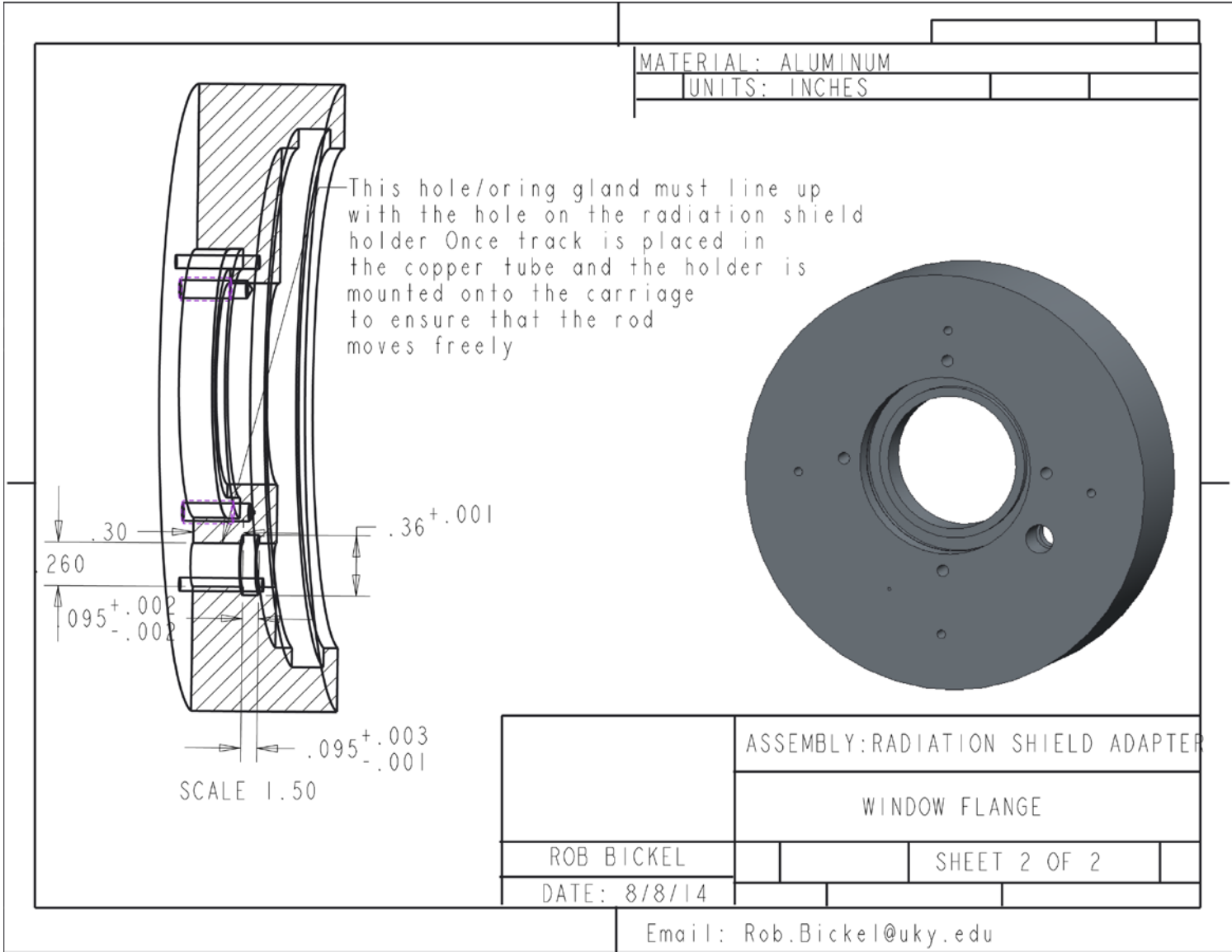




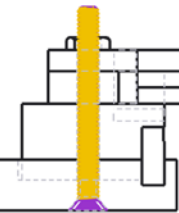
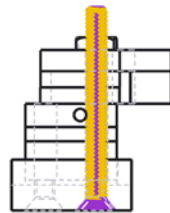
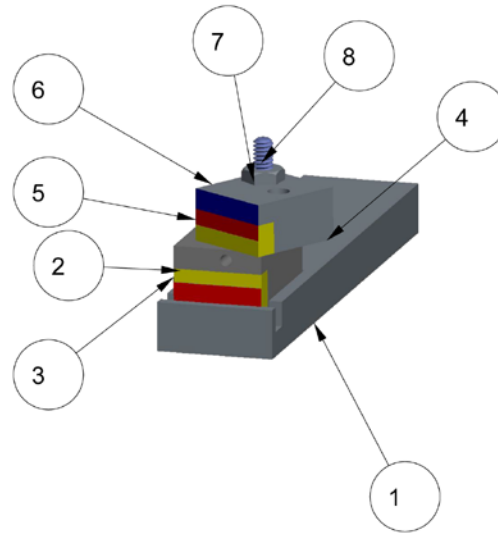






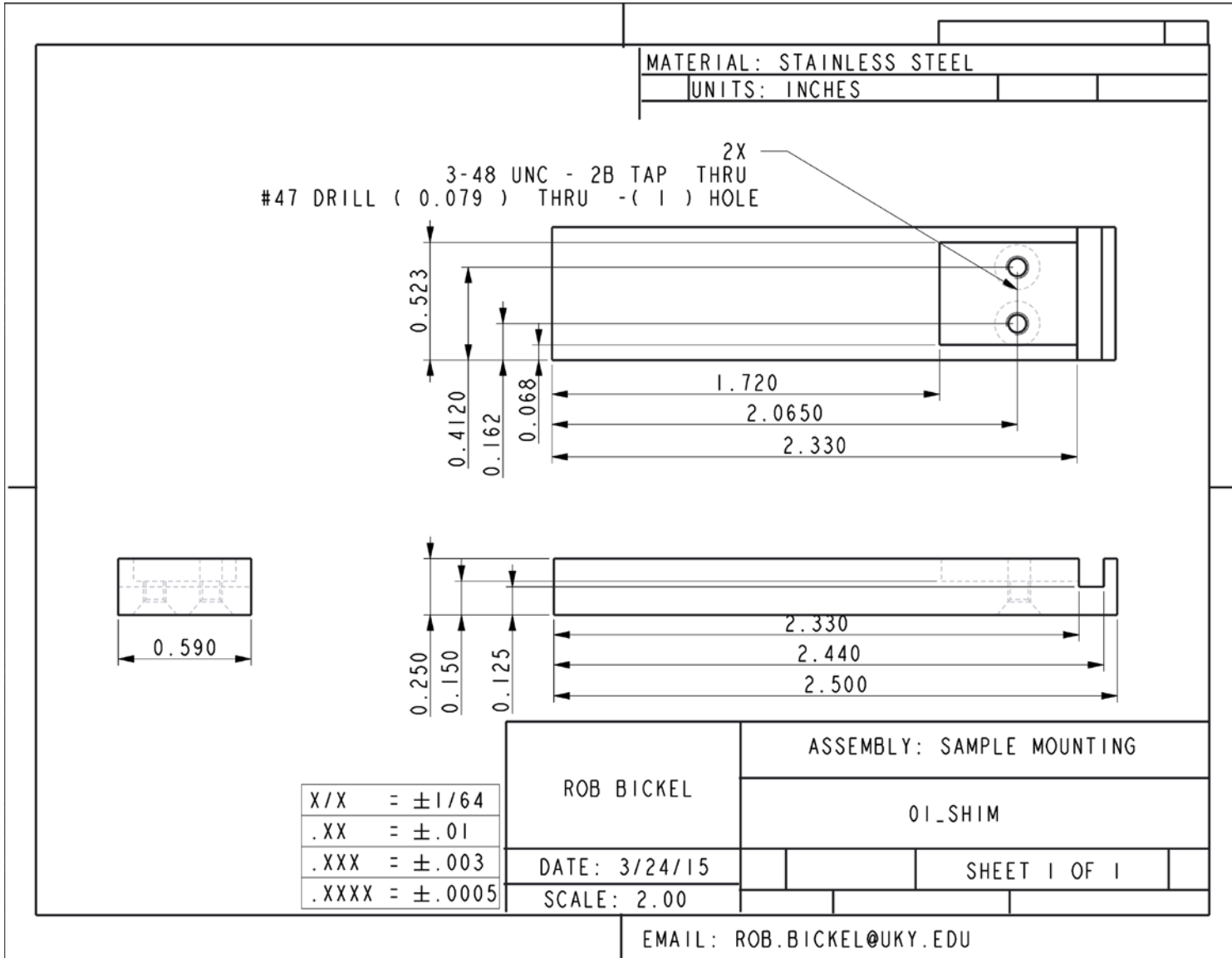


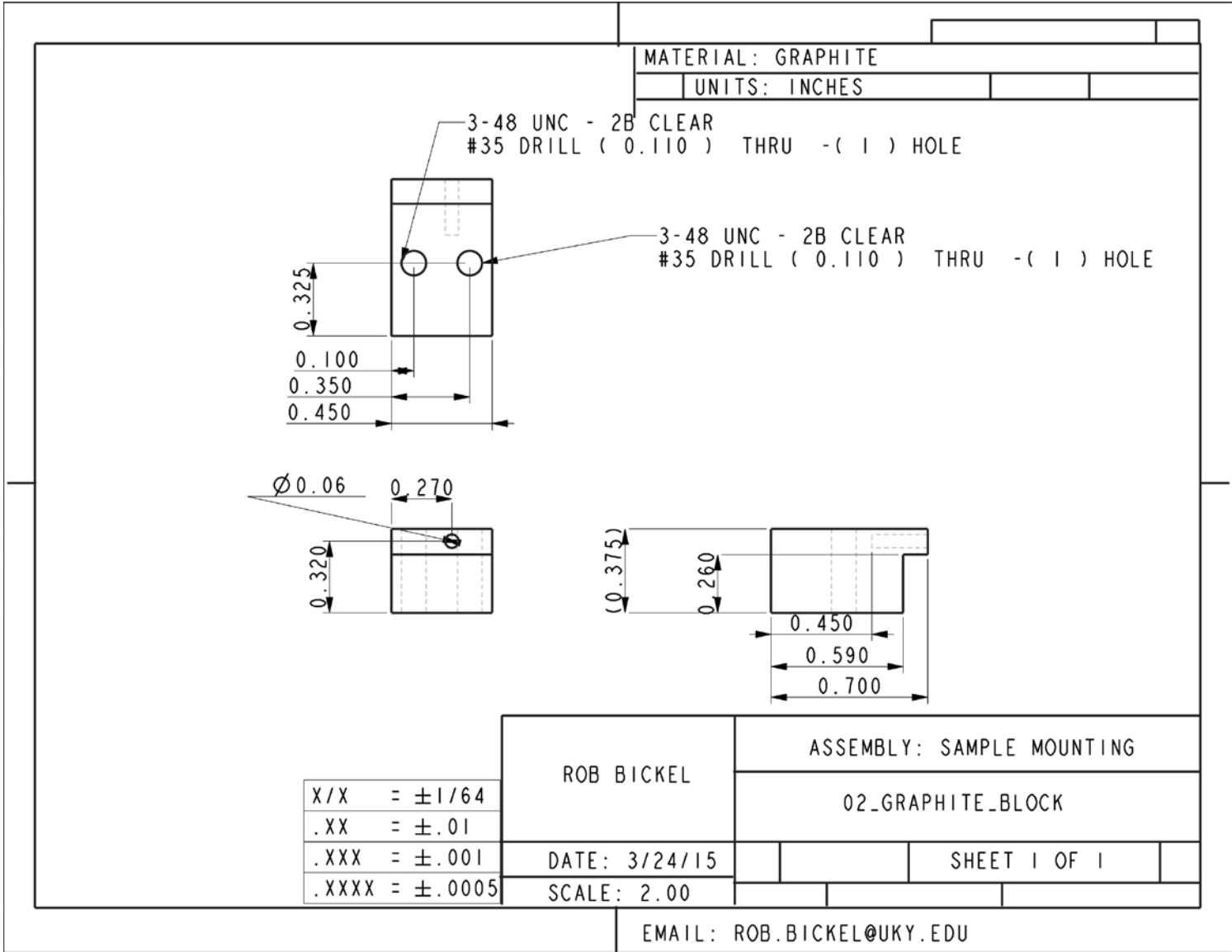
8	3-48 HEX
7	3-48 FLAT HEAD
6	06_SAMPLE
5	05_SAMPLE
4	04_TOP_BLOCK
3	03_SAMPLE_90
2	02_GRAPHITE_BLOCK
1	01_SHIM
ITEM NO	DRAWING NO.

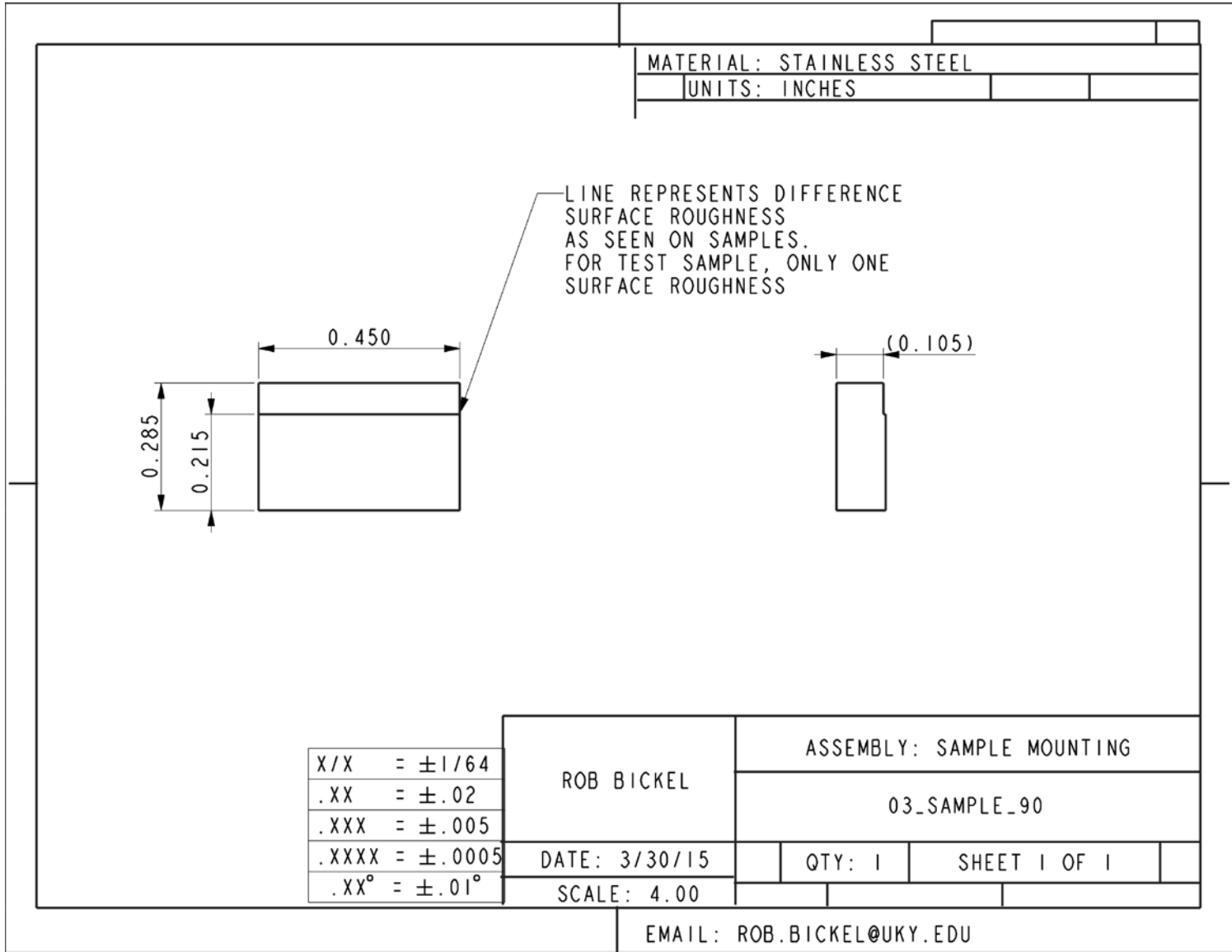


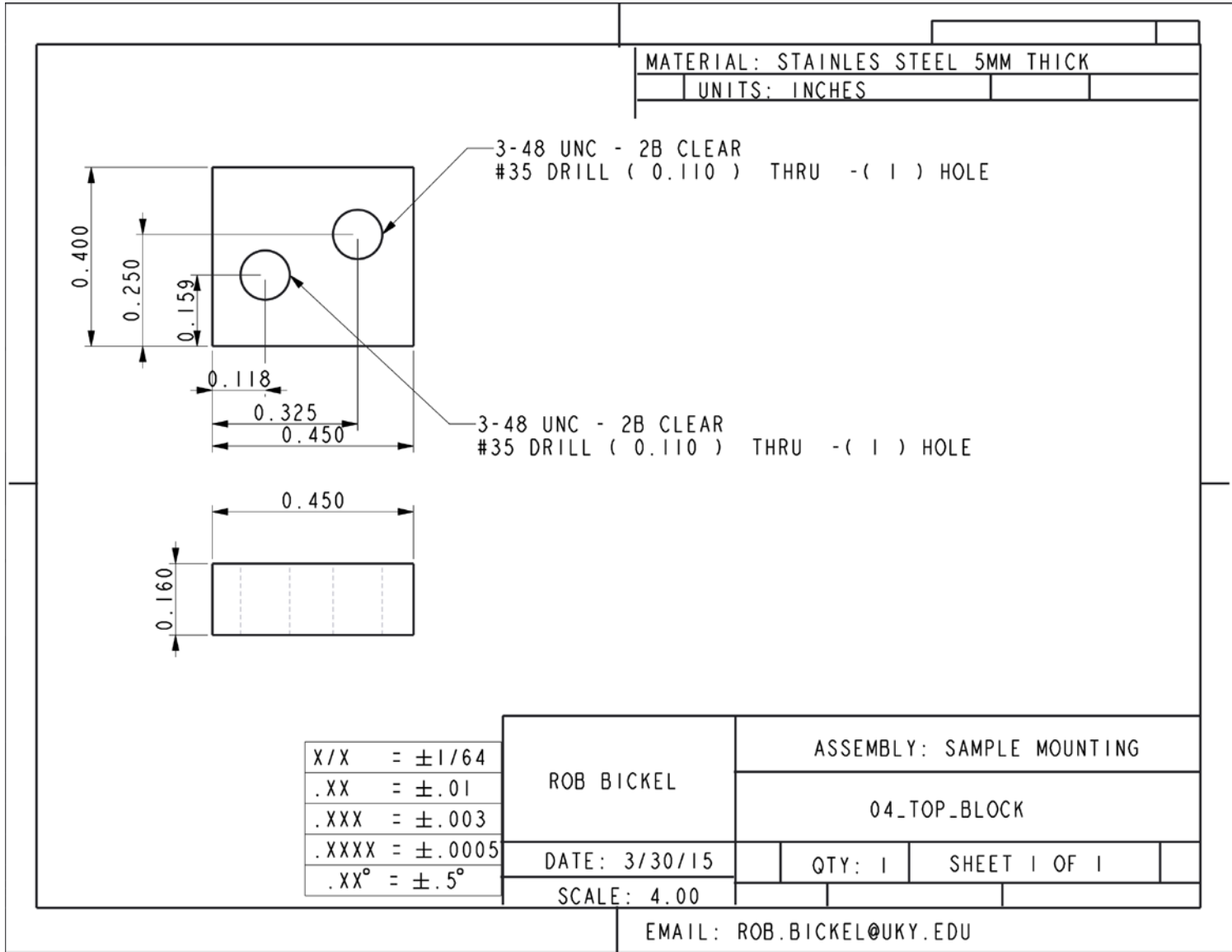
ROB BICKEL	SAMPLE MOUNTING ASSEMBLY		
DATE: 3/30/15	QTY: 1	SHEET 1 OF 1	
SCALE: 1.00			

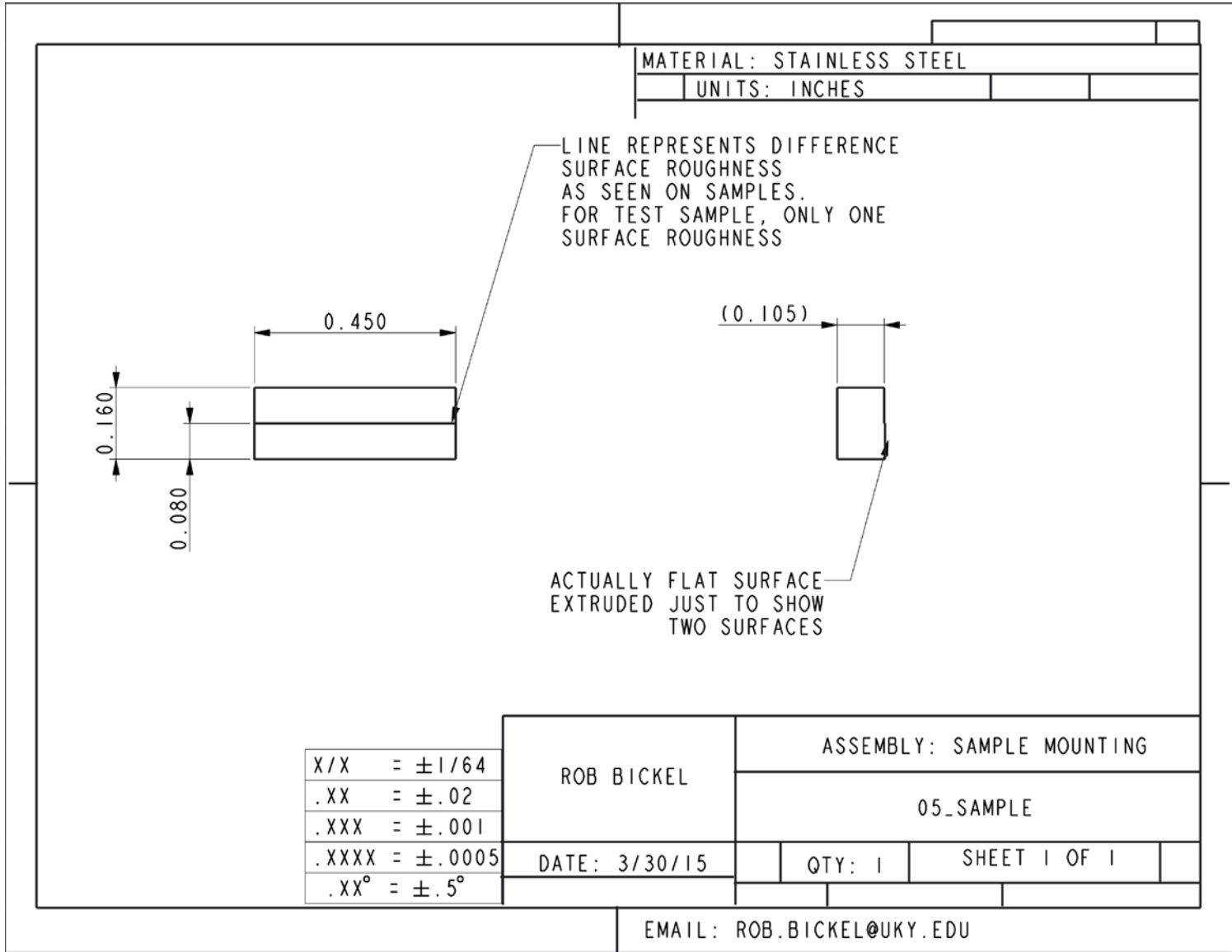
ROB.BICKEL@UKY.EDU

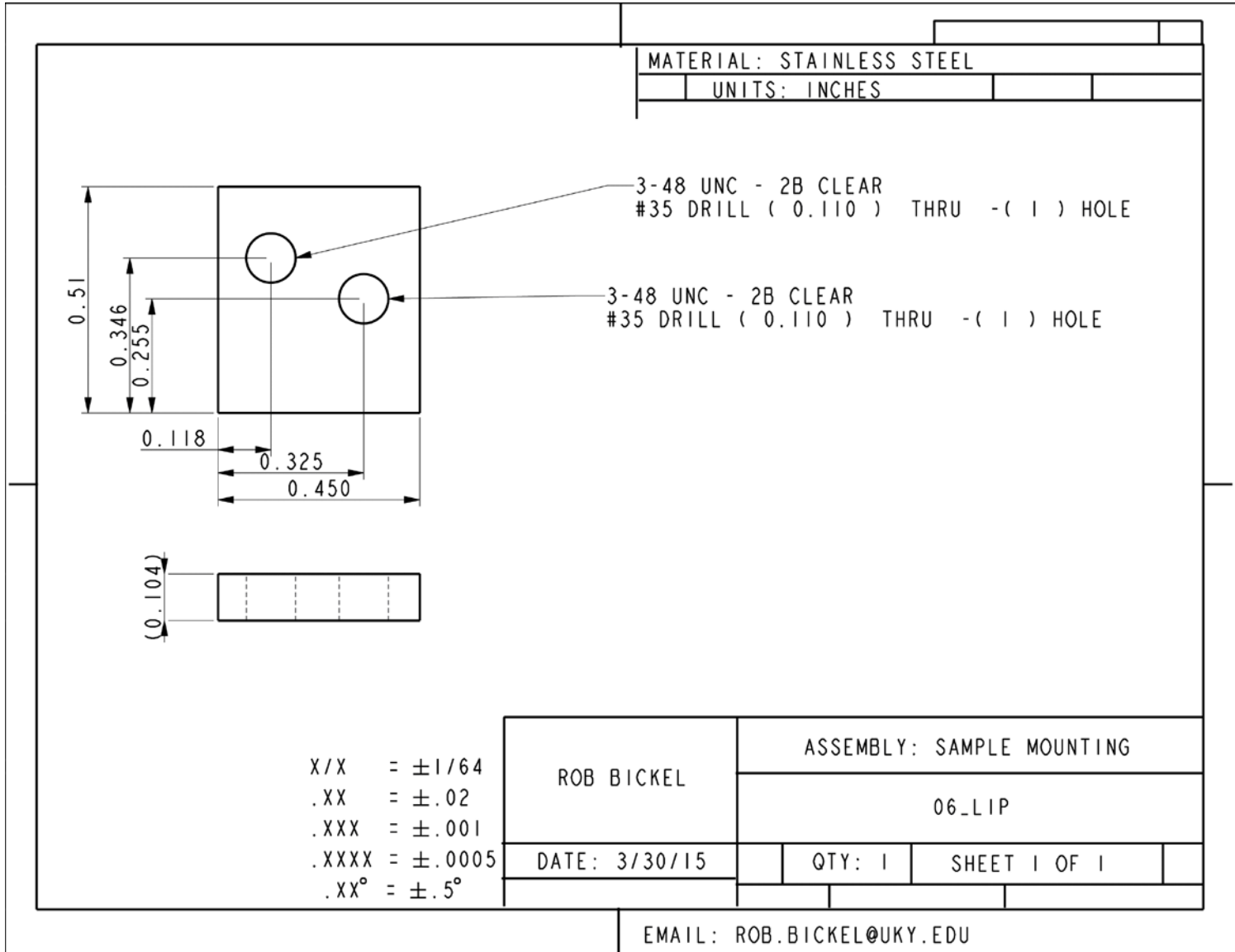


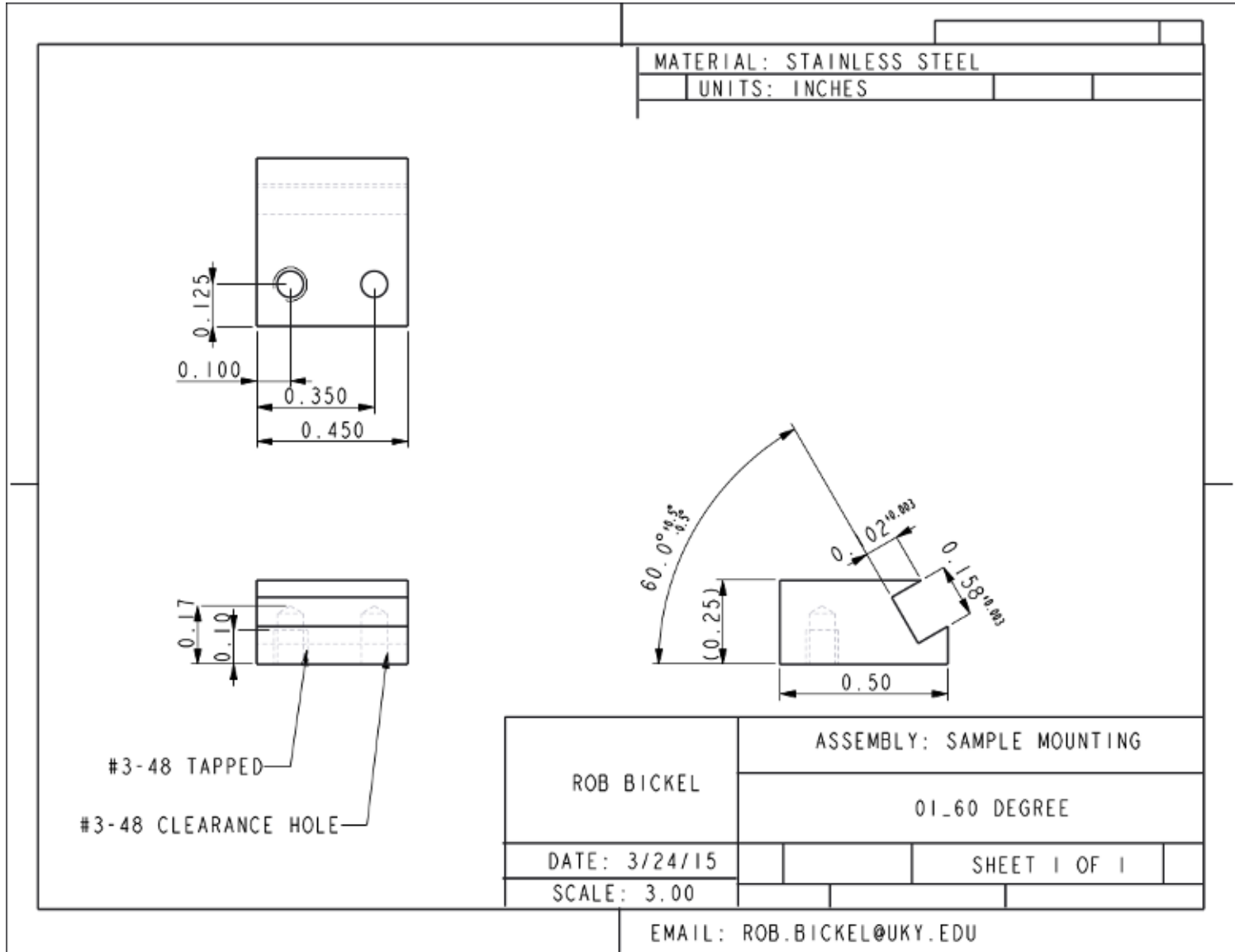






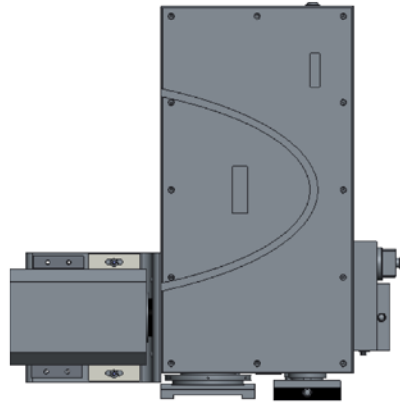
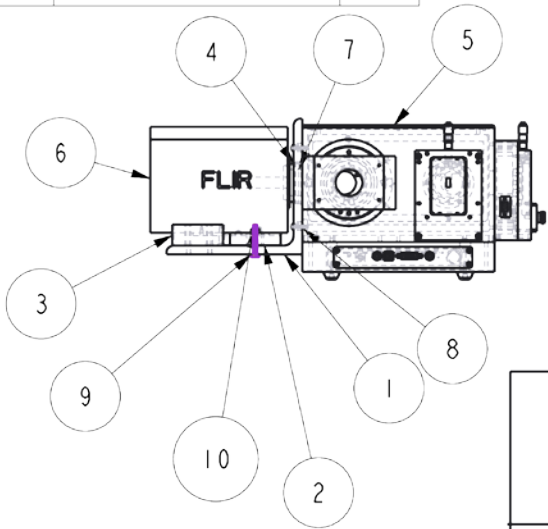




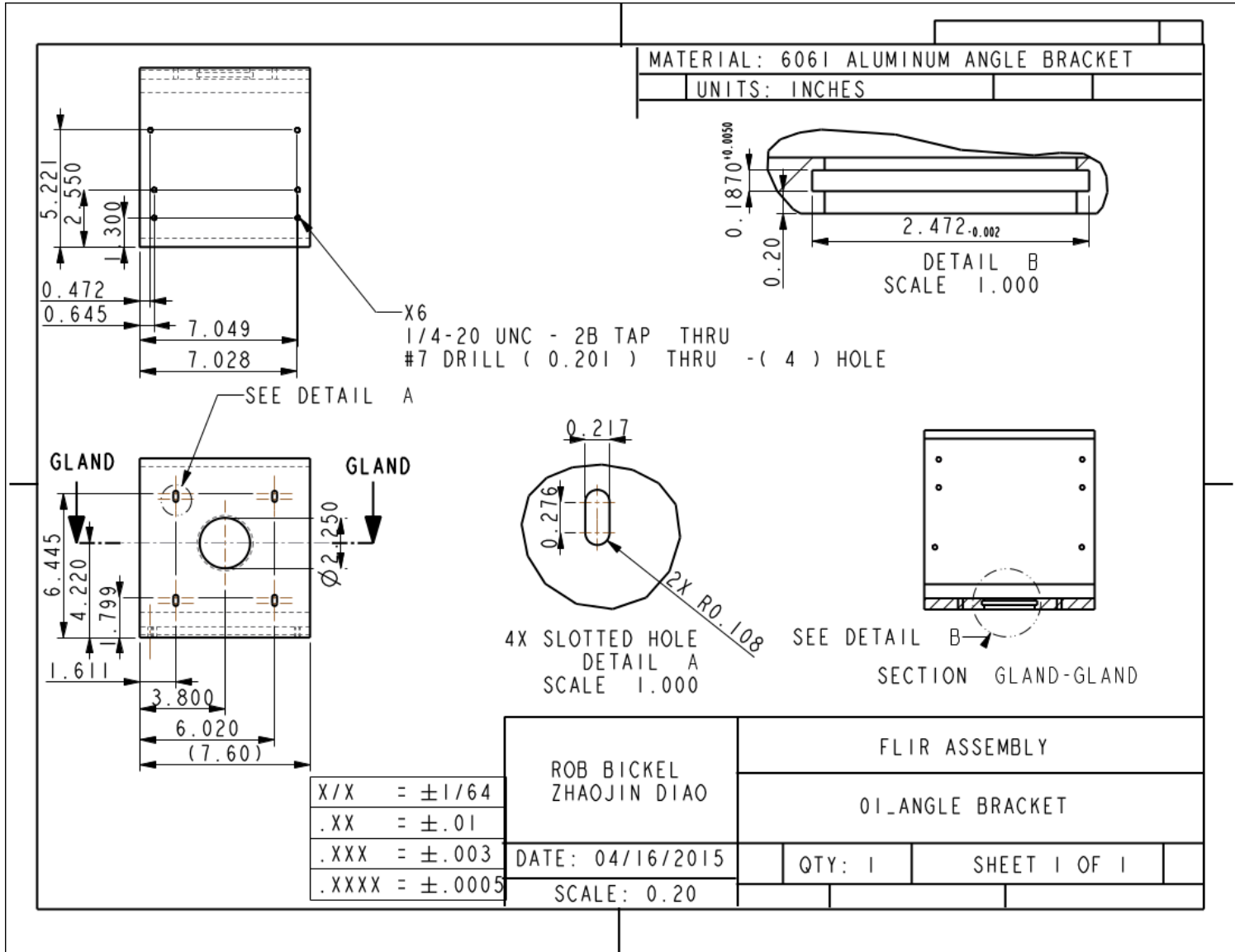


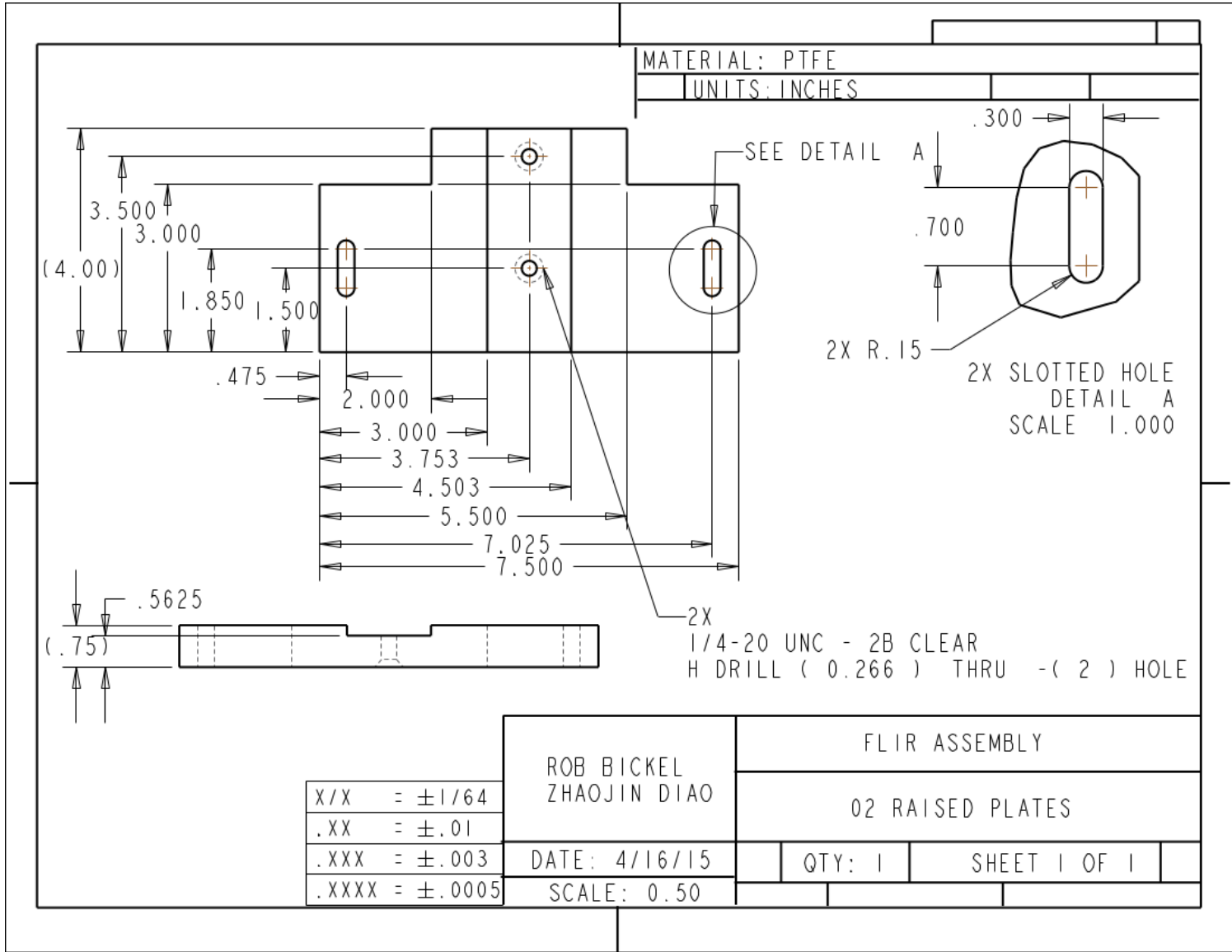
A 1.4 FLIR IR Camera Adapter

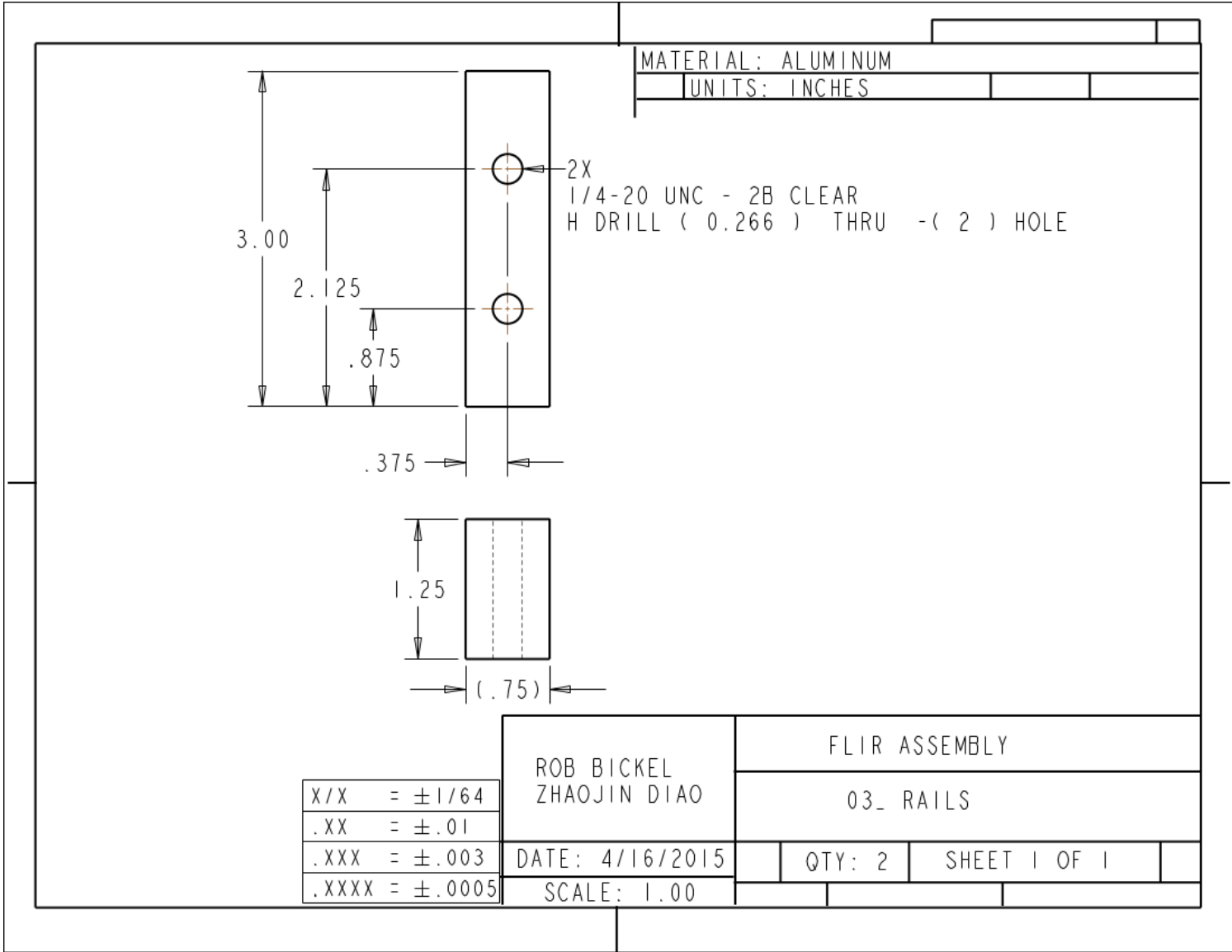
10	1/4-20 CAP SCREW	2
9	1/4-20 FLAT HEAD	2
8	M5 MOUNTING SCREW	4
7	#228 ORING	1
6	FLIR IR CAMERA	1
5	SPECTROMETER	1
4	04_TUBE	1
3	03_RAILS	2
2	02_RAISED_PLATE	1
1	01_ANGLE	1
ITEM NO	DRAWING NO / PART DESCRIPTION	QTY



ROB BICKEL ZHAOJIN DIAO		FLIR ASSEMBLY	
DATE: 04/16/2015	QTY: 1	SHEET 1 OF 1	
SCALE: 0.125			

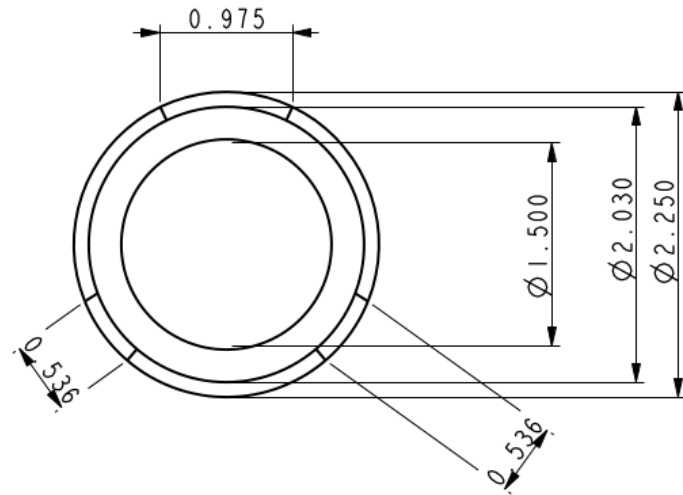
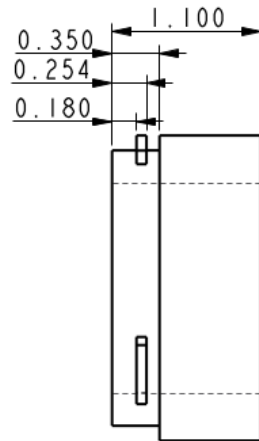






MATERIAL: ALUMINUM

UNITS: INCHES



THIS PART IS BASED ON CAMERA CAP. FOR THE FLANGES THAT STICK OUT, THEY ARE ~120 DEG FROM TOP OF CAP. WHEN MANUFACTURING, PLEASE REQUEST CAP TO CONFIRM FLANGE PLACEMENT

X/X	= ±1/64
.XX	= ±.01
.XXX	= ±.003
.XXXX	= ±.0005

ROB BICKEL
ZHAOJIN DIAO

FLIR ASSEMBLY

04_TUBE

DATE: 4/16/2015

QTY: 1

SHEET 1 OF 1

SCALE: 1.00

APPENDIX 2: CALCULATED ELECTRICAL RESISTIVITY¹

Table A2-1 Vacuum chamber, case 1, graphite sample 1, trial 2

Current (amperes)	Voltage (volts)	Resistance (Ω)	Resistivity (Ω *mm)
20	0.49	0.0245	0.012
40	1.03	0.02575	0.013
60	1.43	0.023833333	0.012
80	1.8	0.0225	0.011

Table A2-2 Vacuum chamber, case 1 graphite sample 2, trial 2

Current (amperes)	Voltage (volts)	Resistance (Ω)	Resistivity (Ω *mm)
20	0.6	0.030	0.013
40	1.55	0.039	0.016
60	1.87	0.031	0.013
80	2.25	0.028	0.012

Table A2-2 Vacuum chamber, case 1, no water cooling

Current (amperes)	Voltage (volts)	Resistance (Ω)	Resistivity (Ω *mm)
20	0.78	0.039	0.020
40	1.55	0.03875	0.020
60	1.87	0.031166667	0.016
80	2.25	0.028125	0.015

¹ Graphite length of 7.50" and a diameter of 0.5" unless noted otherwise.

Table A2-3 Vacuum chamber, case 2, graphite sample 2, trial 1

Current (amperes)	Voltage (volts)	Resistance (Ω)	Resistivity (Ω *mm)
20	0.78	0.039	0.024
40	1.55	0.039	0.024
60	2.14	0.036	0.022
80	2.5	0.031	0.019
100	2.73	0.027	0.017

Table A2-3 Vacuum chamber, case 2, preheated graphite, trial 2

Current (amperes)	Voltage (volts)	Resistance (Ω)	Resistivity (Ω *mm)
20	0.42	0.021	0.013
40	0.79	0.020	0.012
60	1.19	0.020	0.012
80	1.49	0.019	0.012
100	1.82	0.018	0.011

Table A2-4 Vacuum chamber case 3, preheated graphite, trial 2

Current (amperes)	Voltage (volts)	Resistance (Ω)	Resistivity (Ω *mm)
20	0.40	0.020	0.013
40	0.78	0.020	0.012
60	1.15	0.019	0.012
80	1.46	0.018	0.012
100	1.76	0.018	0.011
120	2.05	0.017	0.011
140	2.34	0.017	0.011
160	2.64	0.017	0.011
180	2.92	0.016	0.010
200	3.19	0.016	0.010
220	3.44	0.016	0.010
240	3.72	0.016	0.010
250	3.85	0.015	0.010

APPENDIX 3: CALCULATED HEAT TRANSFER COEFFICIENT VALUES

$$Gr = \frac{L^3 g \beta \rho^2 (T_s - T_\infty)}{\mu^2} \quad \text{(Equation A3-1)}$$

$$Ra = GrPr \quad \text{(Equation A3-2)}$$

$$h_{hc} = (1.32)^4 \sqrt{\frac{(T_s - T_\infty)}{d}} \quad \text{(Equation A3-3)}$$

$$h_{hp} = (1.32)^4 \sqrt{\frac{(T_s - T_\infty)}{d}} \quad \text{(Equation A3-4)}$$

$$h_{vp} = (1.37)^4 \sqrt{\frac{(T_s - T_\infty)}{d}} \quad \text{(Equation A3-5)}$$

Table A3-1 Calculating film coefficient for a horizontal cylinder

Diameter (m)										0.0127
T _{inf}	T _s	T _f	β	ρ	μ	k	Gr	Pr	Ra	h
K			1/K	kg/m ³	kg/(s*m)	W/(m*K)				W/(m ² *K)
295	311	303	0.0033	1.165	1.86E-05	0.026	4.163E+03	0.720	2.997E+03	7.864
295	451	373	0.00268	1.011	2.18E-05	0.032	1.808E+04	0.700	1.265E+04	13.896
295	651	473	0.00211	1.025	2.58E-05	0.039	2.387E+04	0.680	1.623E+04	17.080
295	851	573	0.00175	1.045	2.95E-05	0.045	2.447E+04	0.680	1.664E+04	19.094
295	1251	773	0.00129	1.093	3.58E-05	0.056	2.317E+04	0.700	1.622E+04	21.864

Table A3-2 Film coefficient variables and values for a horizontal plate

Length (m)										0.01905
T _{inf}	T _s	T _f	β	ρ	μ	k	Gr	Pr	Ra	h
K			1/K	kg/m ³	kg/(s*m)	W/(m*K)				W/(m ² *K)
295	311	303	0.0033	1.165	1.86E-05	0.026	1.405E+04	0.720	1.012E+04	7.106
295	451	373	0.0027	1.011	2.18E-05	0.032	6.100E+04	0.700	4.270E+04	12.557
295	651	473	0.0021	1.025	2.58E-05	0.039	8.057E+04	0.680	5.478E+04	15.433
295	851	573	0.0017	1.045	2.95E-05	0.045	8.258E+04	0.680	5.615E+04	17.253
295	1251	773	0.0013	1.093	3.58E-05	0.056	7.818E+04	0.700	5.473E+04	19.757

Table A3-3: Film coefficient variables and value for a vertical plate

Length (m)						0.012				
T_{inf}	T_s	T_f	β	ρ	μ	k	Gr	Pr	Ra	h
K			1/K	kg/m ³	kg/(s*m)	W/(m*K)				W/(m ² *K)
295	311	303	0.0033	1.165	1.86E-05	0.026	3.512E+03	0.720	2.528E+03	8.279
295	451	373	0.0027	1.011	2.18E-05	0.032	1.525E+04	0.700	1.067E+04	14.629
295	651	473	0.0021	1.025	2.58E-05	0.039	2.014E+04	0.680	1.369E+04	17.980
295	851	573	0.0017	1.045	2.95E-05	0.045	2.064E+04	0.680	1.404E+04	20.100
295	1251	773	0.0013	1.093	3.58E-05	0.056	1.954E+04	0.700	1.368E+04	23.017

APPENDIX 4: MATLAB CODE FOR EMISSIVITY ANALYSIS

%%CALCULATES THE EMISSIVITY OF DATA FOR IR DATA IN FURNACE EXPERIMENT
FOR

%%AUTHOR: ROBERT BICKEL

%%DATE: JULY 2015

%%test name

testname=sprintf('test');

GraphiteFileName='Graphite_Dummy.xlsx';

Degree0FileName='Degree0_Dummy.xlsx';

Degree30FileName='Degree30_Dummy.xlsx';

Degree30_leftFileName='Degree30_left_Dummy.xlsx';

Degree30_rightFileName='Degree30_right_Dummy.xlsx';

%%Set Rows and columns

%%Graphite

Graphite_r1=111;

Graphite_r2=117;

Graphite_c1=115;

Graphite_c2=143;

%%Blackbody

Blackbody_r1=111;

Blackbody_r2=118;

Blackbody_c1=115;

Blackbody_c2=144;

%%0 Degree Sample

Sample_0_r1=120;

Sample_0_r2=129;

Sample_0_c1=115;

Sample_0_c2=144;

%%30 Degree Sample

Sample_30_r1=99;

Sample_30_r2=109;

Sample_30_c1=120;

Sample_30_c2=146;

%%30 Degree Sample (Right)

Sample_30r_r1=99;

Sample_30r_r2=109;

Sample_30r_c1=120;

Sample_30r_c2=133;

%%30 Degree Sample (left)

Sample_30L_r1=99;

Sample_30L_r2=109;

Sample_30L_c1=134;

Sample_30L_c2=146;

```

%Physical Constants
c=2.9979*10.^(8); %Speed of Light
pc=6.626*10.^(-34); %Planck Constant
k2=1.3807*10^(-23); %boltszman
n=3800; %wavelength

%Extracting Shield Counts from All Temperatures
ii=450;
for j=1:7
fileName=sprintf('Shield_%d_F*.csv', ii);
csvFiles = dir(fileName) ;
numfiles = length(csvFiles);
mydata = cell(1, numfiles);

for k = 1:numfiles
    SHIELD{k} = importdata(csvFiles(k).name);
end
SumWShield=SHIELD{1,1}+SHIELD{1,2};
%+SHIELD{1,3}+SHIELD{1,4}+SHIELD{1,5}+SHIELD{1,6}+SHIELD{1,7}+SHIELD{1,
8}+SHIELD{1,9}+SHIELD{1,10};
AvgWShield=SumWShield/2;

All_Avg_Shield{1,j}=AvgWShield;
ii=ii+100;
end

%Extracting Background Counts from All Temperatures
iii=450;
for jj=1:7
fileName=sprintf('BG_%d_F*.csv', iii);
csvFiles = dir(fileName) ;
numfiles = length(csvFiles);
mydata = cell(1, numfiles);

for k = 1:numfiles
    BGCOUNTS{k} = importdata(csvFiles(k).name);
end
SumBGCOUNTS=BGCOUNTS{1,1}+BGCOUNTS{1,2};
%+BGCOUNTS{1,3}+BGCOUNTS{1,4}+BGCOUNTS{1,5}+BGCOUNTS{1,6}+BGCOUNTS{1,7}
+BGCOUNTS{1,8}+BGCOUNTS{1,9}+BGCOUNTS{1,10};
AvgBGCOUNTS=SumBGCOUNTS/2;

All_Avg_BGCOUNTS{1,jj}=AvgBGCOUNTS;
iii=iii+100;
end

%Subtracting Background from Shield
Count_Difference=
cellfun(@minus,All_Avg_Shield,All_Avg_BGCOUNTS, 'UniformOutput', false);
%Count_Difference=AvgWShield{1,1}-Avg_BGCOUNTS{1,1};

%Extracting all temperature data
Difference_450=Count_Difference{1,1};
Difference_550=Count_Difference{1,2};

```

```

Difference_650=Count_Difference{1,3};
Difference_750=Count_Difference{1,4};
Difference_850=Count_Difference{1,5};
Difference_950=Count_Difference{1,6};
Difference_1050=Count_Difference{1,7};

```

```

%Creates Blank matrix elements

```

```

blackbody_avg=[];
blackbody_std=[];
blackbody_lowavg=[];
blackbody_highavg=[];
Error_Blackbody=[];
blackbody_temp=[];
blackbody_temp_low=[];
blackbody_temp_high=[];
%Tguess_f=[];
Tlow_blackbody=[];
Thigh_blackbody=[];
TDistpercent_blackbody=[];

```

```

graphiteleft_avg=[];
graphiteleft_std=[];
graphiteleft_lowavg=[];
graphiteleft_highavg=[];
emissgraphite_avg=[];
emissgraphite_low=[];
emissgraphite_high=[];
Std_Error_graphite=[];
Error_graphite_T=[];
Tlow_graphite=[];
Thigh_graphite=[];
TDistpercent_graphite=[];

```

```

Degree0_avg=[];
Degree0_std=[];
Degree0_lowavg=[];
Degree0_highavg=[];
emiss0_avg=[];
emiss0_high=[];
emiss0_low=[];
Std_Error_Degree0=[];
Error_Degree0_T=[];
Tlow_Degree0=[];
Thigh_Degree0=[];
TDistpercent_degree0=[];

```

```

Degree30_avg=[];
Degree30_std=[];
Degree30_lowavg=[];
Degree30_highavg=[];
emiss30_avg=[];
emiss30_low=[];
emiss30_high=[];
Std_Error_Degree30=[];

```

```

Error_Degree30_T=[];
Tlow_Degree30=[];
Thigh_Degree30=[];
TDistpercent_Degree30=[];

Degree30_left_avg=[];
Degree30_left_std=[];
Degree30_left_lowavg=[];
Degree30_left_highavg=[];
emiss30_left_avg=[];
emiss30_left_low=[];
emiss30_left_high=[];
Std_Error_Degree30_left=[];
Error_Degree30_left_T=[];
Tlow_Degree30_left=[];
Thigh_Degree30_left=[];
TDistpercent_Degree30_left=[];

Degree30_right_avg=[];
Degree30_right_std=[];
Degree30_right_lowavg=[];
Degree30_right_highavg=[];
emiss30_right_avg=[];
emiss30_right_low=[];
emiss30_right_high=[];
Std_Error_Degree30_right=[];
Error_Degree30_right_T=[];
Tlow_Degree30_right=[];
Thigh_Degree30_right=[];
TDistpercent_Degree30_right=[];

T2=450+273;
% STATISTICAL SURFACE CALCULATIONS
iv=1;
for iv=1:7
%blackbody calculation
blackbody0=Count_Difference{1,iv}([Blackbody_r1:Blackbody_r2],[Blackbod
y_c1:Blackbody_c2]);
blackbodyshape= reshape(blackbody0.',1,[]);
blackbodyshapesort=sort(blackbodyshape,'descend');
blackbody1=blackbodyshapesort(1,1); %Saves maximum values in graphite
matrix
blackbody2=blackbodyshapesort(1,2);
blackbody3=blackbodyshapesort(1,3);
blackbody4=blackbodyshapesort(1,4);
blackbody5=blackbodyshapesort(1,5);
blackbody6=blackbodyshapesort(1,6);
blackbody7=blackbodyshapesort(1,7);
blackbody8=blackbodyshapesort(1,8);
blackbody9=blackbodyshapesort(1,9);
blackbody10=blackbodyshapesort(1,10);
blackbody11=blackbodyshapesort(1,11);
blackbody12=blackbodyshapesort(1,12);
blackbody13=blackbodyshapesort(1,13);
blackbody14=blackbodyshapesort(1,14);
blackbody15=blackbodyshapesort(1,15);

```

```

blackbody16=blackbodyshapesort(1,16);
blackbody_std_matrix=[blackbody1 blackbody2 blackbody3 blackbody4];
blackbody_v=blackbody1+blackbody2+blackbody3+blackbody4;
blackbody_avg(end+1)=blackbody_v/4;
blackbody_std(end+1)=std(blackbody_std_matrix);
Error_Blackbody(end+1)=1.96*(blackbody_std(1,iv)/sqrt(4));

% graphite calculations
graphiteleft=Count_Difference{1,iv}([Graphite_r1:Graphite_r2],[Graphite
_c1:Graphite_c2]);
%Deletes 15 highest count values
indices1=find(graphiteleft==blackbody1);
graphiteleft(indices1)= NaN;
indices2=find(graphiteleft==blackbody2);
graphiteleft(indices2)= NaN;
indices3=find(graphiteleft==blackbody3);
graphiteleft(indices3)= NaN;
indices4=find(graphiteleft==blackbody4);
graphiteleft(indices4)= NaN;
indices5=find(graphiteleft==blackbody5);
graphiteleft(indices5)= NaN;
indices6=find(graphiteleft==blackbody6);
graphiteleft(indices6)= NaN;
indices7=find(graphiteleft==blackbody7);
graphiteleft(indices7)= NaN;
indices8=find(graphiteleft==blackbody8);
graphiteleft(indices8)= NaN;
indices9=find(graphiteleft==blackbody9);
graphiteleft(indices9)= NaN;
indices10=find(graphiteleft==blackbody10);
indices11=find(graphiteleft==blackbody11);
graphiteleft(indices11)= NaN;
indices12=find(graphiteleft==blackbody12);
graphiteleft(indices12)= NaN;
indices13=find(graphiteleft==blackbody13);
graphiteleft(indices13)= NaN;
indices14=find(graphiteleft==blackbody14);
graphiteleft(indices14)= NaN;
indices15=find(graphiteleft==blackbody15);
graphiteleft(indices15)= NaN;
indices16=find(graphiteleft==blackbody16);
graphiteleft(indices16)= NaN;
graphiteleft_v=graphiteleft(:);
graphiteleft_avg(end+1)=nanmean(graphiteleft_v);
graphiteleft_std(end+1)=nanstd(graphiteleft_v);
Std_Error_graphite(end+1)=1.96*(graphiteleft_std(1,iv)/sqrt(abs(((Graph
ite_r2-Graphite_r1)*(Graphite_c1-Graphite_c2)-15))));
left=Error_Blackbody(1,iv)*((graphiteleft_avg(1,iv))/(blackbody_avg(1,i
v)).^2);
right=(Std_Error_graphite(1,iv))/(blackbody_avg(1,iv));
Error_graphite_T(end+1)=sqrt(left.^2+right.^2);
emissgraphite_avg(end+1)=graphiteleft_avg(1,iv)/blackbody_avg(1,iv);
emissgraphite_low(end+1)=graphiteleft_avg(1,iv)/blackbody_avg(1,iv)-
Error_graphite_T(1,iv);
emissgraphite_high(end+1)=graphiteleft_avg(1,iv)/blackbody_avg(1,iv)+Er
ror_graphite_T(1,iv);

```

```

%Temperature Distribution Error Across Graphite
s=1;
count=0
Tguess=T2-100;
while s==1
    n1=(n/(1*10.^9));
percent_diff=(graphiteleft_avg(1,iv)-
2*graphiteleft_std(1,iv))/graphiteleft_avg(1,iv);
EB1=((2*pc*c.^2)/(n1).^5); %Part one of EB
EB3=(n1*k2*T2);
EB2=(exp((pc*c)/EB3)); %Part two of EB
EB4=(EB2-1);
EBT=(EB1*(1/EB4));

EB3_g=(n1*k2*Tguess);
EB2_g=(exp((pc*c)/EB3_g)); %Part two of EB
EB4_g=(EB2_g-1);
EBT_g=(EB1*(1/EB4_g));

EBT_r=EBT_g/EBT;
test=abs(percent_diff-EBT_r);
if test>.001;
    Tguess=Tguess+.0001;
    count=count+1;
else
    s=0;
end

end

Tlow_graphite(end+1)=Tguess;
Thigh_graphite(end+1)=T2+Tguess;
TDistpercent_graphite(end+1)=100*abs((Tguess-T2)/T2);

% o degree sample calculation
Degree0=Count_Difference{1,iv}([Sample_0_r1:Sample_0_r2],[Sample_0_c1:Sample_0_c2]);
Degree0_v=Degree0(:);
Degree0_avg(end+1)=mean(Degree0_v);
Degree0_std(end+1)=std(Degree0_v);
Std_Error_Degree0(end+1)=1.96*(Degree0_std(1,iv)/sqrt(abs((Sample_0_r2-Sample_0_r1)*(Sample_0_c1-Sample_0_c2))));
left=Error_Blackbody(1,iv)*((Degree0_avg(1,iv))/(blackbody_avg(1,iv)).^2);
right=(Std_Error_Degree0(1,iv))/(blackbody_avg(1,iv));
Error_Degree0_T(end+1)=sqrt(left.^2+right.^2);
emiss0_avg(end+1)=Degree0_avg(1,iv)/blackbody_avg(1,iv);
emiss0_low(end+1)=Degree0_avg(1,iv)/blackbody_avg(1,iv)-Error_Degree0_T(1,iv);
emiss0_high(end+1)=Degree0_avg(1,iv)/blackbody_avg(1,iv)+Error_Degree0_T(1,iv);

% Temperature Distribution Error Across Degree0
s=1;
count=0
Tguess=T2-40;

```

```

while s==1
    n1=(n/(1*10.^9));
    percent_diff=(Degree0_avg(1,iv)-2*Degree0_std(1,iv))/Degree0_avg(1,iv);
    EB1=((2*pc*c.^2)/(n1).^5); %Part one of EB
    EB3=(n1*k2*T2);
    EB2=(exp((pc*c)/EB3)); %Part two of EB
    EB4=(EB2-1);
    EBT=(EB1*(1/EB4));

    EB3_g=(n1*k2*Tguess);
    EB2_g=(exp((pc*c)/EB3_g)); %Part two of EB
    EB4_g=(EB2_g-1);
    EBT_g=(EB1*(1/EB4_g));

    EBT_r=EBT_g/EBT;
    test=abs(percent_diff-EBT_r);

    if test>.01;
        Tguess=Tguess+.01;
        count=count+1;
    else
        s=0;
    end
    % if Tguess >T2+5
    %     s=0
    % end

end
Tlow_Degree0(end+1)=Tguess;
Thigh_Degree0(end+1)=(T2-Tguess)+T2;
TDistpercent_degree0(end+1)=100*abs((Tguess-T2)/T2);

%30 degree sample calculation
Degree30=Count_Difference{1,iv}([Sample_30_r1:Sample_30_r2],[Sample_30_
c1:Sample_30_c2]);
Degree30_v=Degree30(:);
Degree30_avg(end+1)=mean(Degree30_v);
Degree30_std(end+1)=std(Degree30_v);
Std_Error_Degree30(end+1)=1.96*(Degree30_std(1,iv)/sqrt(abs((Sample_30_
r2-Sample_30_r1)*(Sample_30_c1-Sample_30_c2))));
left=Error_Blackbody(1,iv)*((Degree30_avg(1,iv))/(blackbody_avg(1,iv)).
^2);
right=(Std_Error_Degree30(1,iv))/(blackbody_avg(1,iv));
Error_Degree30_T(end+1)=sqrt(left.^2+right.^2);
emiss30_avg(end+1)=Degree30_avg(1,iv)/blackbody_avg(1,iv);
emiss30_low(end+1)=Degree30_avg(1,iv)/blackbody_avg(1,iv)-
Error_Degree30_T(1,iv);
emiss30_high(end+1)=Degree30_avg(1,iv)/blackbody_avg(1,iv)+Error_Degree
30_T(1,iv);

% Temperature Distribution Error Across Degree30
s=1;
count=0
Tguess=T2-70;
while s==1
    n1=(n/(1*10.^9));

```



```

percent_diff=(Degree30_avg(1,iv)-
2*Degree30_std(1,iv))/Degree30_avg(1,iv);
EB1=((2*pc*c.^2)/(n1).^5); %Part one of EB
EB3=(n1*k2*T2);
EB2=(exp((pc*c)/EB3)); %Part two of EB
EB4=(EB2-1);
EBT=(EB1*(1/EB4));

EB3_g=(n1*k2*Tguess);
EB2_g=(exp((pc*c)/EB3_g)); %Part two of EB
EB4_g=(EB2_g-1);
EBT_g=(EB1*(1/EB4_g));

EBT_r=EBT_g/EBT;
test=abs(percent_diff-EBT_r);

if test>.01;
    Tguess=Tguess+.001;
    count=count+1;
else
    s=0;
end
% if Tguess >T2+5
%     s=0
% end

end
Tlow_Degree30(end+1)=Tguess;
Thigh_Degree30(end+1)=(T2-Tguess)+T2;
TDistpercent_Degree30(end+1)=100*abs((Tguess-T2)/T2);

%30 degree sample left half
Degree30_left=Count_Difference{1,iv}([Sample_30L_r1:Sample_30L_r2],[Sam
ple_30L_c1:Sample_30L_c2]);
Degree30_left_v=Degree30_left(:);
Degree30_left_avg(end+1)=mean(Degree30_left_v);
Degree30_left_std(end+1)=std(Degree30_left_v);
Std_Error_Degree30_left(end+1)=1.96*(Degree30_left_std(1,iv)/sqrt(abs((
Sample_30_r2-Sample_30_r1)*(Sample_30_c1-Sample_30_c2))));
left=Error_Blackbody(1,iv)*((Degree30_left_avg(1,iv))/(blackbody_avg(1,
iv)).^2);
right=(Std_Error_Degree30_left(1,iv))/(blackbody_avg(1,iv));
Error_Degree30_left_T(end+1)=sqrt(left.^2+right.^2);
emiss30_left_avg(end+1)=Degree30_left_avg(1,iv)/blackbody_avg(1,iv);
emiss30_left_low(end+1)=Degree30_left_avg(1,iv)/blackbody_avg(1,iv)-
Error_Degree30_left_T(1,iv);
emiss30_left_high(end+1)=Degree30_left_avg(1,iv)/blackbody_avg(1,iv)+Er
ror_Degree30_left_T(1,iv);

%Temperature Distribution Error Across Degree30_left
s=1;
count=0
Tguess=T2-90;
while s==1
    n1=(n/(1*10.^9));

```

```

percent_diff=(Degree30_left_avg(1,iv)-
2*Degree30_left_std(1,iv))/Degree30_left_avg(1,iv);
EB1=((2*pc*c.^2)/(n1).^5); %Part one of EB
EB3=(n1*k2*T2);
EB2=(exp((pc*c)/EB3)); %Part two of EB
EB4=(EB2-1);
EBT=(EB1*(1/EB4));

EB3_g=(n1*k2*Tguess);
EB2_g=(exp((pc*c)/EB3_g)); %Part two of EB
EB4_g=(EB2_g-1);
EBT_g=(EB1*(1/EB4_g));

EBT_r=EBT_g/EBT;
test=abs(percent_diff-EBT_r);

if test>.01;
    Tguess=Tguess+.0001;
    count=count+1;
else
    s=0;
end
% if Tguess >T2+5
%     s=0
% end
end
Tlow_Degree30_left(end+1)=Tguess;
Thigh_Degree30_left(end+1)=(T2-Tguess)+T2;
TDistpercent_Degree30_left(end+1)=100*abs((Tguess-T2)/T2);

%30 degree sample right half
Degree30_right=Count_Difference{1,iv}([Sample_30r_r1:Sample_30r_r2],[Sample_30r_c1:Sample_30r_c2]);
Degree30_right_v=Degree30_right(:);
Degree30_right_avg(end+1)=mean(Degree30_right_v);
Degree30_right_std(end+1)=std(Degree30_right_v);
Std_Error_Degree30_right(end+1)=1.96*(Degree30_right_std(1,iv)/sqrt(abs((Sample_30_r2-Sample_30_r1)*(Sample_30_c1-Sample_30_c2))));
left=Error_Blackbody(1,iv)*((Degree30_right_avg(1,iv))/(blackbody_avg(1,iv)).^2);
right=(Std_Error_Degree30_right(1,iv))/(blackbody_avg(1,iv));
Error_Degree30_right_T(end+1)=sqrt(right.^2+left.^2);
emiss30_right_avg(end+1)=Degree30_right_avg(1,iv)/blackbody_avg(1,iv);
emiss30_right_low(end+1)=Degree30_right_avg(1,iv)/blackbody_avg(1,iv)-
Error_Degree30_right_T(1,iv);
emiss30_right_high(end+1)=Degree30_right_avg(1,iv)/blackbody_avg(1,iv)+
Error_Degree30_right_T(1,iv);

% %Temperature Distribution Error Across Degree30_right
s=1;
count=0
Tguess=T2-70;
while s==1
    n1=(n/(1*10.^9));

```

```

percent_diff=(Degree30_right_avg(1,iv)-
2*Degree30_right_std(1,iv))/Degree30_right_avg(1,iv);
EB1=((2*pc*c.^2)/(n1).^5); %Part one of EB
EB3=(n1*k2*T2);
EB2=(exp((pc*c)/EB3)); %Part two of EB
EB4=(EB2-1);
EBT=(EB1*(1/EB4));

EB3_g=(n1*k2*Tguess);
EB2_g=(exp((pc*c)/EB3_g)); %Part two of EB
EB4_g=(EB2_g-1);
EBT_g=(EB1*(1/EB4_g));

EBT_r=EBT_g/EBT;
test=abs(percent_diff-EBT_r);

if test>.01;
    Tguess=Tguess+.01;
    count=count+1;
else
    s=0;
end
% if Tguess >T2+5
%     s=0
% end

end
Tlow_Degree30_right(end+1)=Tguess;
Thigh_Degree30_right(end+1)=(T2-Tguess)+T2;
TDistpercent_Degree30_right(end+1)=100*abs((Tguess-T2)/T2);
%
T2=T2+100;
iv=iv+1; %#ok<*FXSET>
end

%Graphite data transpose
graphiteleft_avg= graphiteleft_avg';
graphiteleft_std= graphiteleft_std';
graphiteleft_lowavg= graphiteleft_lowavg';
graphiteleft_highavg= graphiteleft_highavg';
emissgraphite_avg= emissgraphite_avg';
emissgraphite_low= emissgraphite_low';
emissgraphite_high= emissgraphite_high';
TDistpercent_graphite=TDistpercent_graphite';

%0 Degree data transpose
Degree0_avg= Degree0_avg';
Degree0_std= Degree0_std';
Degree0_lowavg= Degree0_lowavg';
Degree0_highavg= Degree0_highavg';
emiss0_avg= emiss0_avg';
emiss0_low= emiss0_low';
emiss0_high= emiss0_high';
TDistpercent_degree0=TDistpercent_degree0';

```

```

%30 Degree data transpose
Degree30_avg= Degree30_avg';
Degree30_std= Degree30_std';
Degree30_lowavg= Degree30_lowavg';
Degree30_highavg= Degree30_highavg';
emiss30_avg= emiss30_avg';
emiss30_low= emiss30_low';
emiss30_high= emiss30_high';
TDistpercent_Degree30=TDistpercent_Degree30';

%30 Degree left data transpose
Degree30_left_avg= Degree30_left_avg';
Degree30_left_std= Degree30_left_std';
Degree30_left_lowavg= Degree30_left_lowavg';
Degree30_left_highavg= Degree30_left_highavg';
emiss30_left_avg= emiss30_left_avg';
emiss30_left_low= emiss30_left_low';
emiss30_left_high= emiss30_left_high';
TDistpercent_Degree30_left=TDistpercent_Degree30_left';

%30 Degree right data transpose
Degree30_right_avg= Degree30_right_avg';
Degree30_right_std= Degree30_right_std';
Degree30_right_lowavg= Degree30_right_lowavg';
Degree30_right_highavg= Degree30_right_highavg';
emiss30_right_avg= emiss30_right_avg';
emiss30_right_low= emiss30_right_low';
emiss30_right_high= emiss30_right_high';
TDistpercent_Degree30_right=TDistpercent_Degree30_right';

%Excel export variables
temperature=[450 550 650 750 850 950 1050];
temperature=temperature';
header = {'temperature (C)', 'Average Count', 'Standard Deviation
Count', 'Average emissivity', 'Lower Bound Emissivity', 'Upper Bound
Emissivity', 'Temperature Distribution (Percent)'};

%graphite excel export
Graphite_data_set=[temperature graphiteleft_avg graphiteleft_std
emissgraphite_avg emissgraphite_low emissgraphite_high
TDistpercent_graphite];
graphite_table=dataset({Graphite_data_set,header{:}});
export(graphite_table, 'XLSFile', GraphiteFileName);

%0 degree excel export
Degree_0_data_set=[temperature Degree0_avg Degree0_std emiss0_avg
emiss0_low emiss0_high TDistpercent_degree0];
degree0table=dataset({Degree_0_data_set,header{:}});
export(degree0table, 'XLSFile', Degree0FileName);

%30 degree excel export;
Degree_30_data_set=[temperature Degree30_avg Degree30_std emiss30_avg
emiss30_low emiss30_high TDistpercent_Degree30];
degree30table=dataset({Degree_30_data_set,header{:}});
export(degree30table, 'XLSFile', Degree30FileName);

```

```

%30 degree left excel export;
Degree_30_left_data_set=[temperature Degree30_left_avg
Degree30_left_std emiss30_left_avg emiss30_left_low emiss30_left_high
TDistpercent_Degree30_left];
degree30_lefttable=dataset({Degree_30_left_data_set,header{:}});
export(degree30_lefttable, 'XLSFile', Degree30_leftFileName);

%30 degree right excel export;
Degree_30_right_data_set=[temperature Degree30_right_avg
Degree30_right_std emiss30_right_avg emiss30_right_low
emiss30_right_high TDistpercent_Degree30_right];
degree30_righttable=dataset({Degree_30_right_data_set,header{:}});
export(degree30_righttable, 'XLSFile', Degree30_rightFileName);

%%Surface Plots
%Full Scale
YAxis=size(Difference_1050,1);
XAxis=size(Difference_1050,2);
figure()
surf(Difference_1050)
view(0,270)
colormap hot
title(['Full Scale IR Image ', testname])
xlabel('Pixel')
ylabel('Pixel')
xlim([1 XAxis])
ylim([1 YAxis])
set(gca, 'fontsize', 40)
h = colorbar;
ylabel(h, 'Counts')

%graphite sample
graphite_surf=Difference_1050([Graphite_r1:Graphite_r2],[Graphite_c1:Gr
aphite_c2]);
YAxis=size(graphite_surf,1);
XAxis=size(graphite_surf,2);
figure()
surf(graphite_surf)
view(0,270)
colorbar
%caxis([5500 7000])
title(['Zoomed Grapephite ', testname])
colormap hot
xlabel('Pixel')
ylabel('Pixel')
xlim([1 XAxis])
ylim([1 YAxis])
set(gca, 'fontsize', 40)
h = colorbar;
ylabel(h, 'Counts')

%0 Sample
Degree0_surf=Difference_1050([Sample_0_r1:Sample_0_r2],[Sample_0_c1:Sam
ple_0_c2]);
YAxis=size(Degree0_surf,1);

```

```

XAxis=size(Degree0_surf,2);
figure()
surf(Degree0_surf)
view(0,270)
colorbar
%caxis([2500 5000])
title(['0 degree sample ', testname])
colormap hot
xlabel('Pixel')
ylabel('Pixel')
xlim([1 XAxis])
ylim([1 YAxis])
set(gca, 'fontsize', 40)
h = colorbar;
ylabel(h, 'Counts')

%30 sample
Degree30_surf=Difference_1050([Sample_30_r1:Sample_30_r2],[Sample_30_c1
:Sample_30_c2]);
YAxis=size(Degree30_surf,1);
XAxis=size(Degree30_surf,2);
figure()
surf(Degree30_surf)
view(0,270)
colorbar
%caxis([2500 5000])
title(['Zoomed 30 degree sample ', testname])
colormap hot
xlabel('Pixel')
ylabel('Pixel')
xlim([1 XAxis])
ylim([1 YAxis])
set(gca, 'fontsize', 40)
h = colorbar;
ylabel(h, 'Counts')

%temperature plot
figure()
hold on
temperaturescatter=[450 550 650 750 850 950 1050];
s = sprintf('Furnace Temperature %cC', char(176));
s1=scatter(temperaturescatter,TDistpercent_graphite,400);
set(s1, 'Marker', 'square', 'LineWidth', 3)
xlabel(s);
ylabel('Temperature Distribution (Percent)')
set(gca, 'fontsize', 25)
s2=scatter(temperaturescatter,TDistpercent_degree0,400);
set(s2, 'Marker', 'square', 'LineWidth', 3)
s3=scatter(temperaturescatter,TDistpercent_Degree30,400);
set(s3, 'Marker', 'diamond', 'LineWidth', 3)
s4=scatter(temperaturescatter,TDistpercent_Degree30_left,400);
set(s4, 'Marker', '^', 'LineWidth', 3)
s5=scatter(temperaturescatter,TDistpercent_Degree30_right,400);
set(s5, 'Marker', 'p', 'LineWidth', 3)
grid on
ax=gca;

```

```
set(ax,'XTick',[350 450 550 650 750 850 950 1050 1150])  
legend('Graphite', '0 Degree Sample', '30 Degree Sample', '30 Degree  
Sample Left', '30 Degree Sample Right')
```

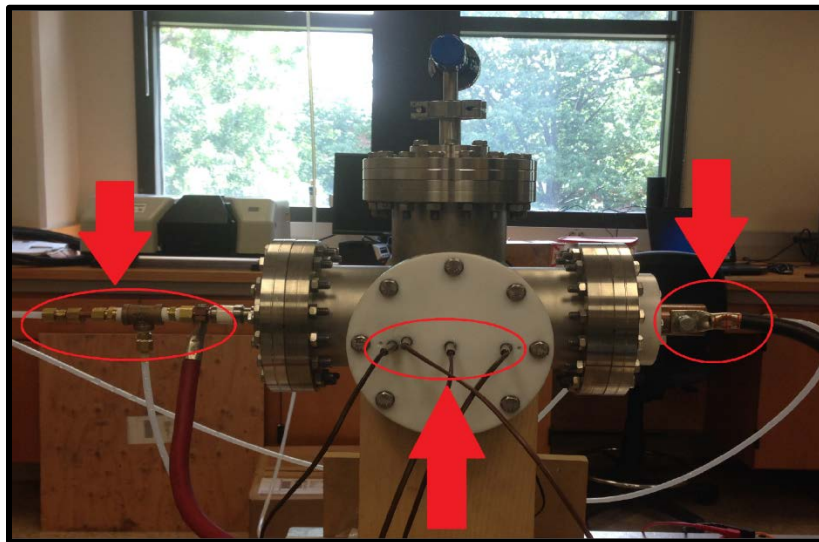
APPENDIX 5: OPERATION MANUAL FOR SIX WAY

Overview:

The vacuum chamber located on the optical table in Rgan 318 is lethal while in operation. Current outputted by the DC generator may reach up to 200 Amperes. It is inherit that the following checklist be performed before operation begins. Furthermore, it is the responsibility of the investigator to inform all personnel in the lab of the dangers that exist while using the vacuum chamber in conjunction with the DC generator.

Hot Sections:

Pictured below is the back view of the vacuum chamber. The areas circled in red are conducting current while experiments are being performed. Thus, they must never come in contact with anything. These areas include the brass water cooling fittings, the copper anode and copper cathode, and the thermocouples sticking out of the flange.



Vacuum Chamber Checklist:

- 1) Ensure that the DC power supply is powered off and disconnected from the power strip.
- 2) Inspect the vacuum chamber to ensure that the electrical connections are secure.
- 3) Inspect the electrical cables and water cooling tubes to ensure that they are secure and are not in the way of foot traffic.
- 4) Check the water cooling system by turning on the water supply first, and then by turning on the water return line.
- 5) Let the water run for two minutes at full pressure to make sure that there are no leaks in the water cooling system.
- 6) Turn the return line off, followed by the supply line.
- 7) Repair any leaks if needed and recheck the water cooling lines.
- 8) Open the window and visually inspect the graphite rod to ensure that there are no cracks.

- 9) Using the multimeter set on the resistance function and the mode set to sound, check the circuit in figure 1.1. The multimeter should beep indicating that there is a circuit between the anode and cathode. If it does not, check the graphite rod and connections.

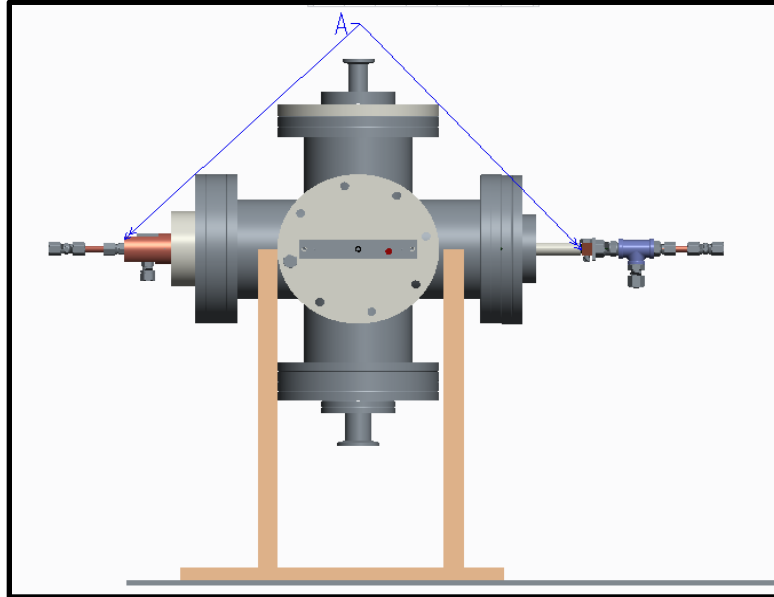


Figure A-1: Circuit Test I

- 10) Check the following points (A-F) in figure A-2 with the multimeter. The multimeter should NOT beep and should NOT display a resistance. If it does, determine how electricity is flowing to these points.

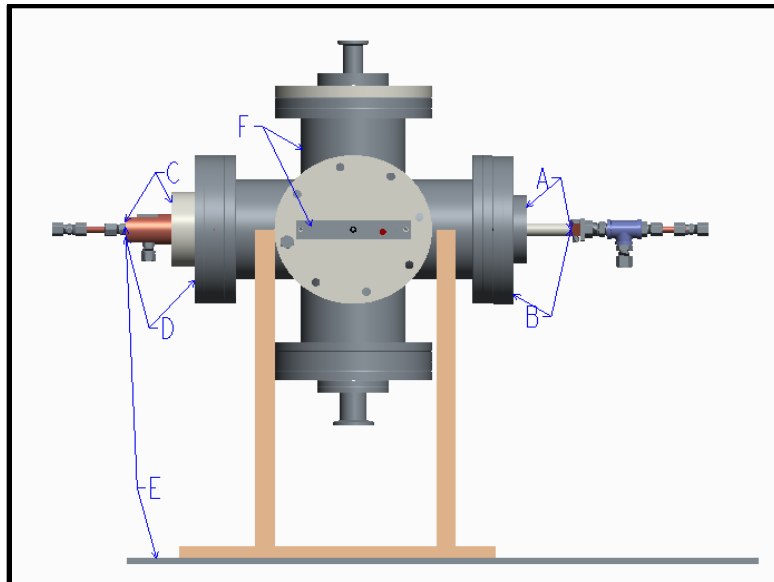


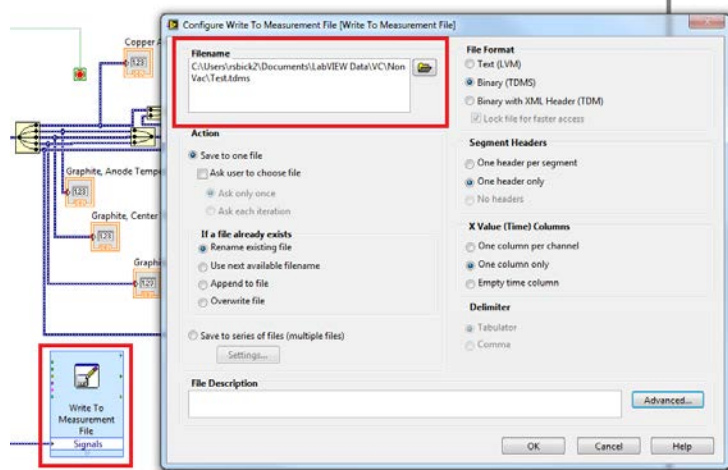
Figure A-2: Circuit test II

- 11) Make sure the vacuum chamber is grounded.

- 12) Make sure the optical table is grounded.
- 13) Ensure the thermocouples inside of the chamber are not in contact with the walls.
- 14) Check the thermocouple cables are secure in the DAQ unit and that the DAQ unit is grounded.
- 15) Check to ensure the hoses are connected from the pump to the chamber.
- 16) Free the table from any tools or clutter.
- 17) Erect barriers to prevent foot traffic by the pump and vacuum chamber.
- 18) Place warning sign by the vacuum chamber.
- 19) Inform all personnel in the lab that the experiments will start.

LabView Checklist

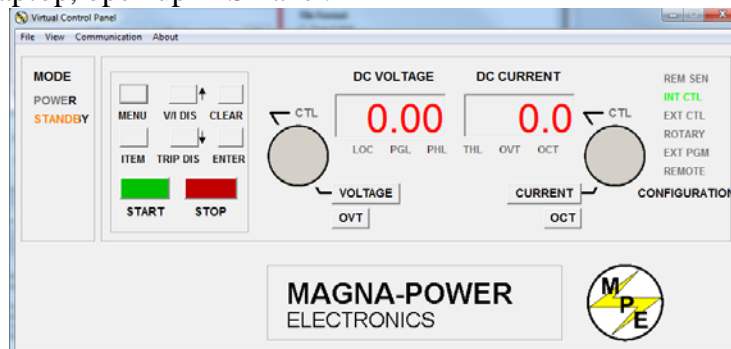
- 1) Open C:\Users\rsbick2\Documents\LabVIEW Data\VC\Thermocoules.vi
- 2) Double click one of the charts to open the block diagram
- 3) Check the write to mesa block to ensure you will be writing to the correct file.



- 4) Run a test to ensure all thermocouples are reporting values
- 5) Stop the test

DC Power Supply Checklist

- 1) Review the DC Power Supply Manual located in the file cabinet.
- 2) Ensure the DC power supply is plugged into the laptop.
- 3) Plug the DC power supply into the cable tray.
- 4) Turn the DC power supply on.
- 5) On the lab laptop, open up RIS Panel.



- 6) For instructions on how to operate the power supply, see the DC power supply manual.

Operation of Vacuum Chamber:

- 1) Turn the pump on and rotate the knob to I.
- 2) Wait for the pressure gauge to show a steady reading.
- 3) If you expect temperatures of the copper anode and cathode to reach 300°C or above, apply water cooling by turning the supply line on, and then the return line.
- 4) Begin recording temperature data with LabView
- 5) Set and apply the current on the Virtual Control panel.
- 6) Wait for the temperatures of graphite to stabilize.
- 7) During this time, check the graphite through the window.
- 8) When the temperature remains constant ($\pm 1^\circ\text{C}$ for two minutes), stop recording data.
- 9) Go into the "Write to Mesa" block and change the filename.
- 10) Repeat steps 4-8 until experiments are complete.
- 11) When completed, turn the power supply off.
- 12) Verify with the multimeter that no current is running through the graphite rod.
- 13) Turn the vacuum pump off.
- 14) Turn the water supply lines off.

Post Experiment checklist

- 1) Disconnect the power supply from the power strip
- 2) Check the graphite rod to ensure no cracking has occurred.
- 3) Inform all personnel that experiments are completed.
- 4) Remove barriers and signs

REFERENCES

- Abishek, S. S., and S. S. Katte. "View Factors between Disk/Rectangle and Rectangle in Parallel and Perpendicular Planes." *Journal of Thermophysics* 21.1 (n.d.): 236-39. Print.
- Alfano, G., and A. Sarno. "Normal and Hemispherical Thermal Emittances of Cylindrical Cavities." *ASME Journal of Heat Transfer* 97.3 (1975): 387-90. Print.
- Atkinson, W. H., and R. R. Strange. *Development of Sensors for Ceramic Components in Advanced Propulsion System*. Rep. no. 195324. East Hartford: Pratt & Whitney, 1994. NASA. Web.
- Bejan, Adrian. *Convection Heat Transfer*. Chichester: Wiley, 2013. Print.
- "Blackbody Calibrator, 970 Pegasus R." *Isotech: The Source for Calibration Professionals*. N.p., n.d. Web. 2 Feb. 2014.
<http://www.isotechna.com/High_Temperature_Blackbody_Source_p/970%20pegasus%20r.htm>.
- Campo, Leire Del, Raúl B. Pérez-Sáez, Xabier Esquisabel, Ignacio Fernández, and Manuel J. Tello. "New Experimental Device for Infrared Spectral Directional Emissivity Measurements in a Controlled Environment." *Review of Scientific Instruments* 77.11 (2006): 113111. Web.
- Edmund Optics. Transmission Curve for Sapphire Windows. N.d. Raw data. Barrington, NJ.
- "Elevated Temperature Physical Properties of Stainless Steels." *British Stainless Steel Association* (n.d.): n. pag. Web. 23 Jan. 2015.

- Funai, A. I. "A Multichamber Calorimeter For High-Temperature Emittance Studies." *Measurement of Thermal Radiation Properties of Solids* (1963): 317-27. Print.
- Furukawa, T., and T. Iuchi. "Experimental Apparatus for Radiometric Emissivity Measurements of Metals." *Review of Scientific Instruments* 71.7 (2000): 2843. Web.
- Hagqvist, Petter, Fredrik Sikstrom, and Anna-Karin Christiansson. "Emissivity Estimation for High Temperature Radiation Pyrometry on Ti-6Al-4V." *Measurement* 46 (2013): 871-80. Elsevier. Web.
- "High Temperature Comparison Blackbody Furnaces." *CHINO*. N.p., n.d. Web. 2 Feb. 2014. <<https://www.chino.co.jp/english/products/traceability/ir-r24.html>>.
- Ho, C. Y., and T. K. Chu. *Electrical Resistivity and Thermal Conductivity of Nine Selected AISI Stainless Steels*. Rep. Vol. 45. N.p.: American Iron and Steel Institute, 1977. Print.
- Incropera, Frank P. *Introduction to Heat Transfer*. Estados Unidos: John Wiley & Sons, 2007. Print.
- Ku, Harry. "Notes on the Use of Propagation of Error Formulas." *J Research of National Bureau of Standards-C. Engineering and Instrumentation* 70.4 (1966): 263-73. Web.
- Limperis, T., D. M. Szeles, and W. L. Wolfe. *Measurement of Thermal Radiation Properties of Solids*. Rep. no. NASA-SP31. Richmond: NASA, 1963. Print.
- Limperis, T., D. M. Szeles, and W. L. Wolfe. "The Measurement of Total, Normal Emittance of Three Nuclear Reactor Materials." *Measurement of Thermal Radiation Properties of Solids* (1963): 357-64. Print.

- Markham, J. R., P. R. Solomon, and P. E. Best. "An FTIR Based Instrument for Measuring Spectral Emittance of Material at High Temperature." *Review of Scientific Instruments* 61.12 (1990): 3700-708. Web.
- Matula, R. A. "Electrical Resistivity of Copper, Gold, Palladium and Silver." *Journal of Physical and Chemical Reference Data* 8.4 (1979): 150-60. Print.
- Modest, M. F. *Radiative Heat Transfer*. Amsterdam: Academic, 2003. Print.
- Noyes, B., Jr. "The Variation in the Resistance of Carbon and Graphite with Temperature." *American Physical Society* 24 (1924): n. pag. Web.
- Persky, Merle J., and Martin Szczesniak. "Infrared, Spectral, Directional-hemispherical Reflectance of Fused Silica, Teflon Polytetrafluoroethylene Polymer, Chrome Oxide Ceramic Particle Surface, Pyromark 2500 Paint, Krylon 1602 Paint, and Duraflect Coating." *Applied Optics Appl. Opt.* 47.10 (2008): 1389-396. Web.
- Postlethwait, M. A., K. K. Sikka, M. F. Modest, and J. R. Hellmann. "High-Temperature, Normal Spectral Emittance of Silicon Carbide Based Materials." *Journal of Thermophysics and Heat Transfer* 8.3 (1994): 412-18. Web.
- Reda, Daniel C., Michael C. Wilder, and Dinesh K. Prabhu. "Transition Experiments on Slightly Blunted Cones with Distributed Roughness in Hypersonic Flight." *AIAA Journal* 50.10 (2012): 2248-254. Web.
- Salmon, David. "Thermal Conductivity of Insulations Using Guarded Hot Plates, including Recent Developments and Sources of Reference Materials." *Meas. Sci. Technol. Measurement Science and Technology* 12.12 (2001): n. pag. Web.

- Stamm, Alfred J. "The Electrical Resistance of Wood as A Measure of Its Moisture Content." *Ind. Eng. Chem. Industrial & Engineering Chemistry* 19.9 (1927): 1021-025. Web.
- Touloukian, Y. S., and David P. DeWitt. *Thermal Radiative Properties: Metallic Elements and Alloys*. New York: IFI/Plenum, 1970. Print.
- Touloukian, Y. S., and David P. DeWitt. *Thermal Radiative Properties: Nonmetallic Solids*. New York: IFI/Plenum, 1972. Print.
- Touloukian, Y. S. *Thermophysical Properties of Matter; the TPRC Data Series; a Comprehensive Compilation of Data*. New York: IFI/Plenum, 1970. Print.
- Welsch, Gerhard, Rodney Boyer, and E. W. Collings. *Materials Properties Handbook: Titanium Alloys*. Materials Park, OH: ASM International, 1994. Print.
- Wilder, Michael C., Daniel C. Reda, and Dinesh K. Prabhu. *Heat-Transfer Measurements on Hemisphere in Hypersonic Flight through Air and CO₂*. Proc. of 42nd AIAA Thermophysics Conference, Honolulu, Hawaii. N.p.: n.p., n.d. Print.
- Zaworski, J. R., J. R. Welty, and M. K. Drost. "Measurement and Use of Bi-directional Reflectance." *International Journal of Heat and Mass Transfer* 39.6 (1996): 1149-156. Web.

VITA

Robert S. Bickel

Place of Birth: Louisville, Kentucky

Education

Bachelor of Science in Mechanical Engineering, 2008-2012 University of Kentucky, Lexington, Kentucky.

Professional Positions

Graduate Researcher, University of Kentucky. Jan 2015-Aug 2015, Jan 2014-Aug 2014

Mechanical Engineering Intern, Walt Disney Parks and Resorts. Aug 2014-Dec 2014

Teaching Assistant, University of Kentucky. Jan 2013-Dec 2013

Piping Field Engineer Intern, Bechtel Corporation. Jun 2012-Dec 2012. Jun 2013-Aug 2013

Professional Publications

Bickel, R. and Winter, M., 2015 “Experimental Methods for Measuring Spectral,

Directional Emissivity at High Temperatures,” *Presentations 40th Dayton-Cincinnati Aerospace Symposium*.

Bickel, R. and Winter, M., 2015 “Experimental Methods for Measuring Spectral,

Directional Emissivity at High Temperatures,” *KY EPSCoR Annual Conference*